MULTI-BODY DYNAMIC ANALYSIS OF HELICOPTER ROTORS

By

Nicolaas J. Theron

A Thesis Submitted to the Graduate

Faculty of Rensselaer Polytechnic Institute

in Partial Fulfillment of the

Requirements for the Degree of

DOCTOR OF PHILOSOPHY

Major Subject: Mechanical Engineering

Approved by the
Examining Committee:

Prof. O. A. Bauchau, Thesis Adviser

Prof. P. Hajela, Member

Prof. A. Z. Lemnios, Member

Prof. M. S. Shephard, Member

Prof. S. S. Sternstein, Member

Rensselaer Polytechnic Institute
Troy, New York

September 1994
(For Graduation December 1994)

CONTENTS

LIST OF TABLES vi

LIST OF FIGURES viii

ACKNOWLEDGEMENT xv

ABSTRACT xvi

1. INTRODUCTION AND HISTORICAL REVIEW 1

   1.1 The role of beam modeling in multi-body dynamic analysis of helicopter rotors 5

   1.2 The role of the time integration methods in multi-body dynamic analysis 7

   1.3 Objective and Layout of this thesis 13

2. EQUATIONS OF MOTION AND EQUATIONS OF CONSTRAINT . . . 16

   2.1 Introduction 16

   2.2 Equations of motion of a non-linear beam. 17

   2.3 Constraint equations for a revolute joint 21

3. THREE DIMENSIONAL SAINT-VENANT BEAM THEORY 23

   3.1 Introduction 23

      3.1.1 Compatibility of the three dimensional Saint-Venant beam theory with multi-body dynamic analysis 23

      3.1.2 The three dimensional Saint-Venant beam theory 25

   3.2 The Helicoidal Beam 27

      3.2.1 One dimensional equilibrium equations 28

      3.2.2 Three dimensional strain-displacement relationship 29

   3.3 Central Solution 33

      3.3.1 Principle of Virtual Work 34

      3.3.2 Rigid body motion of the beam 36

      3.3.3 Sectional displacement 37

      3.3.4 Calculation of cross sectional properties 40

   3.4 Stress and strain recovery 46

   3.5 Strain energy expression 47

3.6 Conclusion 49

4. ADVANCED BEAM THEORY 50

4.1 Introduction 50

4.2 Analysis of beams subjected to differential warping 50

4.2.1 Strain Energy 51

4.2.2 Kinetic Energy 52

4.3 Analysis of beams subjected to the non-linear strain effect 56

4.4 Conclusion 60

5. NUMERICAL EXAMPLES: CROSS SECTIONAL ANALYSIS 61

5.1 Introduction 61

5.2 Validation of central and extremity solution calculation 62

5.2.1 Solid rectangular section 64

5.2.2 Hollow rectangular section 64

5.2.3 Sections of beams with high curvature 71

5.2.4 The ONERA section: an experimental helicopter rotor blade . 71

5.3 Advanced beam theory 79

5.3.1 Comparison between the advanced beam element and the regular beam element, in the absence of differential warping and non-linear strain effects 80

5.3.2 Clamped-free beam with hollow rectangular section 84

5.3.3 The MBB prototype tail rotor flexbeam 88

5.4 Conclusion 95

6. ENERGY PRESERVING SCHEME FOR THE TIME INTEGRATION OF BEAM EQUATIONS OF MOTION 120

6.1 Introduction 120

6.2 Discretization of the finite rotations. 121

6.3 Basic discretization of the equations of motion of a beam. 122

6.4 An energy preserving scheme for beams. 124

6.5 Conclusion 125

7. ENERGY DECAYING SCHEME FOR THE TIME INTEGRATION OF BEAM EQUATIONS OF MOTION 126

7.1 Introduction 126

7.2 Time discontinuous Galerkin scheme for a single degree of freedom system. 127
7.3 Stability proof based on an energy argument. 130
7.4 An energy decaying scheme for beams. 134
7.5 Conclusion 136
8. ENFORCEMENT OF KINEMATIC CONSTRAINTS 137
8.1 Introduction 137
8.2 The pendulum: treating a single degree of freedom system as a two degree of freedom system with a single constraint. 138
8.3 Energy Preserving Scheme 139
8.3.1 Discretization of pendulum equations 139
8.3.2 Basic discretization of the forces of constraint in a revolute joint. 140
8.3.3 Vanishing of work done by forces of constraint of a revolute joint 141
8.4 Energy Decaying Scheme 142
8.4.1 Pendulum equations: constant in time Lagrange multiplier. . . 143
8.4.2 Pendulum equations: linear in time Lagrange multiplier. . . . 145
8.4.3 Vanishing of work done by forces of constraint of a revolute joint 146
8.5 Conclusion 148
9. NUMERICAL EXAMPLES: ENERGY PRESERVING AND ENERGY DECAYING SCHEMES FOR THE TIME INTEGRATION OF MULTI-BODY SYSTEMS 149
9.1 Introduction 149
9.2 Solution of multi-body dynamic problems with the Energy Preserving Scheme 153
9.2.1 Convergence study: a hinged beam subjected to ramp loading 153
9.2.2 Flexible elbow mechanism 155
9.2.3 Swing with flexible beam and concentrated mass 158
9.3 Solution of beam structural dynamic problems using the Energy Decaying Scheme 162
9.3.1 Convergence study: a hinged beam rotating at a constant angular velocity 162

9.3.2 A hinged beam subjected to a single triangular pulse transverse tip load . . . 163
9.3.3 Hinged, L-shaped beam structure . . . 167
9.4 Solution of multi-body dynamic problems with the Energy Decaying Scheme . . . 172
9.4.1 Flexible Elbow Mechanism . . . 172
9.4.2 Swing with flexible beam and concentrated mass . . . 176
9.5 Conclusion . . . 178
9.5.1 Energy preserving scheme . . . 178
9.5.2 Energy decaying scheme applied to non-linear beams . . . 179
9.5.3 Energy decaying scheme for multi-body analysis . . . 180
10. DISCUSSION AND CONCLUSIONS . . . 246
10.1 Cross sectional analysis . . . 246
10.2 Time integration schemes with guaranteed unconditional stability in non-linear multi-body analysis . . . 247
10.3 Recommendations for future work . . . 250
10.3.1 Cross sectional analysis: the advanced beam theory . . . 250
10.3.2 Energy decaying scheme for time integration . . . 251
LITERATURE CITED . . . 253
APPENDICES . . . 256
A. THE CONFORMAL ROTATION VECTOR. . . . 256
B. DEFINITION OF THE NON-LINEAR STRAIN EFFECT MATRICES. . 257

LIST OF TABLES

Table 5.1 Symbols used in sectional stiffness and compliance tensor listings 63

Table 5.2 Hollow rectangular section 1: Ply material properties 65

Table 5.3 Hollow rectangular section 1: Lay-up of cases analyzed 66

Table 5.4 Hollow rectangular section 1: Two diagonal components of the sectional compliance tensor, for different material lay-ups . 66

Table 5.5 Hollow rectangular section 1: Two off-diagonal components of the sectional compliance tensor, for different material lay-ups . 67

Table 5.6 Hollow rectangular section 1: Sectional stiffness tensor C^*, multiplied by 10^{-4}, of the lay-up specimen A, as calculated with a thin walled approximation to the classical Saint-Venant beam theory. 68

Table 5.7 Hollow rectangular section 1: Sectional stiffness tensor C^*, multiplied by 10^{-4}, of the lay-up specimen A, as calculated with the three dimensional Saint-Venant beam theory 69

Table 5.8 Hollow rectangular section 1: Comparison of the diagonal components of the sectional stiffness tensor C^*, as calculated with a thin walled approximation to the classical Saint-Venant beam theory, and the three dimensional Saint-Venant beam theory 70

Table 5.9 ONERA section: Material properties 73

Table 5.10 ONERA section: Cross sectional compliance tensor S^*, multiplied by 10^{10}, for the case with no pre-twist 74

Table 5.11 ONERA section: Cross sectional compliance tensor S^*, multiplied by 10^{10}, for the case with the correct pre-twist 74

Table 5.12 ONERA section: Cross sectional stiffness tensor C^*, multiplied by 10^{-6}, for the case with no pre-twist 75

Table 5.13 ONERA section: Cross sectional stiffness tensor C^*, multiplied by 10^{-6}, for the case with the correct pre-twist 75

Table 5.14 Comparison of the natural frequencies of vibration of a cantilevered beam with free warping and no load, as calculated with regular and advanced beam elements 81

Table 5.15 Comparison of the natural frequencies of vibration of a cantilevered beam with free warping, and applied tip bending and torsional moments of 50 *lb.in.* each, as calculated with regular and advanced beam elements 82

Table 5.16 Comparison of the components of the static tip displacement and conformal rotation vectors, of a cantilevered beam with free warping, under applied tip bending and torsional moments, as calculated with regular and advanced beam elements 83

Table 5.17 Hollow rectangular section 2: Ply material properties 85

Table 5.18 Hollow rectangular section 2: Comparison of the tip rotation angle under an applied tip torque, as calculated using the analytical solution, and two finite element models employing either regular or advanced beam elements 87

Table 5.19 MBB cruciform flexbeam: material properties 90

Table 5.20 MBB cruciform flexbeam: Cross sectional stiffness characteristics 91

Table 5.21 MBB cruciform flexbeam: Comparison of blade torsional stiffness values 94

Table 9.1 Hinged beam convergence study: Beam properties 154

LIST OF FIGURES

Figure 2.1 Beam reference line in undeformed and deformed position . . . 18

Figure 2.2 Kinematics of a revolute joint 21

Figure 3.1 The beam reference line, cross section and generic point P, in the plane of the cross section, in the undeformed configuration 30

Figure 3.2 Components of the sectional displacement and rotation vectors 36

Figure 4.1 Position of generic point P, initially in the plane of the cross section, after deformation 53

Figure 5.1 Hollow rectangular section 1: Finite element mesh of section . 96

Figure 5.2 ONERA section: Finite element mesh of section 97

Figure 5.3 ONERA section: Detail of leading edge finite element mesh . . 98

Figure 5.4 ONERA section: Detail of trailing edge finite element mesh . 99

Figure 5.5 ONERA section: Refined detail of trailing edge finite element mesh, showing the connection between the aluminum tab and the four layered composite skin 100

Figure 5.6 ONERA section: Characteristic warping associated with an axial force 101

Figure 5.7 ONERA section: Characteristic warping associated with a transverse shear force in the $\vec{e}_2$ (or Y) direction 102

Figure 5.8 ONERA section: Characteristic warping associated with a transverse shear force in the $\vec{e}_3$ (or Z) direction 103

Figure 5.9 ONERA section: Characteristic warping associated with a torsional moment 104

Figure 5.10 ONERA section: Characteristic warping associated with a bending moment about the $\vec{e}_2$ (or Y) axis 105

Figure 5.11 ONERA section: Characteristic warping associated with a bending moment about the $\vec{e}_3$ (or Z) axis 106

Figure 5.12 MBB cruciform flexbeam: Finite element mesh of section . . . 107

Figure 5.13 MBB cruciform flexbeam: Characteristic warping associated with an axial force 108

Figure 5.14 MBB cruciform flexbeam: Characteristic warping associated with a transverse shear force in the $\vec{e}_2$ direction 109

Figure 5.15 MBB cruciform flexbeam: Characteristic warping associated with a transverse shear force in the $\vec{e}_3$ direction 110

Figure 5.16 MBB cruciform flexbeam: Characteristic warping associated with a torsional moment 111

Figure 5.17 MBB cruciform flexbeam: Characteristic warping associated with a bending moment about the $\vec{e}_2$ axis 112

Figure 5.18 MBB cruciform flexbeam: Characteristic warping associated with a bending moment about the $\vec{e}_3$ axis 113

Figure 5.19 MBB tail rotor blade with cruciform flexbeam: finite element mesh of blade 114

Figure 5.20 MBB tail rotor blade with cruciform flexbeam: fan plot of natural angular frequency as a function of rotor speed, for the case where the flexbeam portion is modeled with regular beam elements 115

Figure 5.21 MBB tail rotor blade with cruciform flexbeam: natural angular frequency of the 1st flapping mode as a function of rotor speed 116

Figure 5.22 MBB tail rotor blade with cruciform flexbeam: natural angular frequency of the 2nd flapping mode as a function of rotor speed 117

Figure 5.23 MBB tail rotor blade with cruciform flexbeam: natural angular frequency of the 1st lead-lag mode as a function of rotor speed 118

Figure 5.24 MBB tail rotor blade with cruciform flexbeam: natural angular frequency of the 1st torsional mode as a function of rotor speed 119

Figure 7.1 Typical time step with function discontinuities at boundaries . . 128

Figure 7.2 Comparison of spectral radii of various time integration schemes 130

Figure 7.3 Comparison of period elongation of various time integration schemes 131

Figure 7.4 Comparison of algorithmic damping of various time integration schemes 132

Figure 9.1 Hinged beam convergence study: Error in tip displacement and velocity, and root internal moment vectors 181

Figure 9.2 Flexible elbow mechanism, in the initial configuration 182

Figure 9.3 Flexible elbow mechanism: Motion and deformation of beams 183

Figure 9.4 Flexible elbow mechanism: Time history of conformal rotation vector component a_1 at mass 1 measured in the triad associated with the root of beam 1 184

Figure 9.5 Flexible elbow mechanism: Spectrum of conformal rotation vector component a_1 at mass 1 measured in the triad associated with the root of beam 1 185

Figure 9.6 Flexible elbow mechanism: Time history of conformal rotation vector component a_2 at mass 1 measured in the triad associated with the root of beam 1 186

Figure 9.7 Flexible elbow mechanism: Spectrum of conformal rotation vector component a_2 at mass 1 measured in the triad associated with the root of beam 1 187

Figure 9.8 Flexible elbow mechanism: Time history of transverse shear force in $\vec{e}_3$ direction at root of beam 1 188

Figure 9.9 Flexible elbow mechanism: Spectrum of transverse shear force in $\vec{e}_3$ direction at root of beam 1 189

Figure 9.10 Flexible elbow mechanism: Time history of transverse displacement of mass 2 in the $\vec{e}_2$ direction relative to, and measured in the triad associated with the root of beam 2 190

Figure 9.11 Flexible elbow mechanism: Spectrum of transverse displacement of mass 2 in the $\vec{e}_2$ direction relative to, and measured in the triad associated with the root of beam 2 191

Figure 9.12 Swing: Time history of (a) e_2 and (b) the energy-like norm e_1 192

Figure 9.13 Swing: Time history of e_2 for (a) $\Delta t = 5.0 \times 10^{-4}$, (b) $\Delta t = 5.0 \times 10^{-5}$, (c) $\Delta t = 5.0 \times 10^{-6}$ seconds 193

Figure 9.14 Rotating hinged beam: Error in tip conformal rotation vector component a_2 in the $\mathcal{S}$ system, and root axial force f_1 in the $\mathcal{S}^*$ system 194

Figure 9.15 Hinged beam subjected to pulse load: Time histories of root transverse shear force f_2, measured in $\mathcal{S}^*$ and calculated with 250 equal time steps 195

Figure 9.16 Hinged beam subjected to pulse load: Spectra of root transverse shear force f_2, measured in $\mathcal{S}^*$ 196

Figure 9.17 Hinged beam subjected to pulse load: Time histories of root torsional moment m_1, measured in $\mathcal{S}^*$ and calculated with 250 equal time steps 197

Figure 9.18 Hinged beam subjected to pulse load: Spectra of root torsional moment m_1, measured in $\mathcal{S}^*$ 198

Figure 9.19 Hinged beam subjected to pulse load: Time histories of tip angular velocity component ω_1, measured in $\mathcal{S}$ and calculated with 250 equal time steps 199

Figure 9.20 Hinged beam subjected to pulse load: Spectra of tip angular velocity about the component ω_1, measured in $\mathcal{S}$ 200

Figure 9.21 Hinged beam subjected to ramp loading: Error in tip displacement and root internal moment vectors as a function of the number of steps 201

Figure 9.22 Hinged beam subjected to ramp loading: Error in tip displacement and root internal moment vectors as a function of the CPU time 202

Figure 9.23 Hinged beam subjected to pulse load: Error in tip displacement vector as a function of the number of steps 203

Figure 9.24 Hinged beam subjected to pulse load: Error in tip velocity and root internal moment vectors as a function of the number of steps 204

Figure 9.25 Hinged beam subjected to pulse load: Error in tip displacement vector as a function of the CPU time 205

Figure 9.26 Hinged beam subjected to pulse load: Error in tip velocity and root internal moment vectors as a function of the CPU time 206

Figure 9.27 Hinged, L-shaped beam structure: Motion and deformation of beams 207

Figure 9.28 Hinged, L-shaped beam structure: Time histories of the $\vec{i}_1$ and $\vec{i}_2$ direction tip displacement components of both beams . 208

Figure 9.29 Hinged, L-shaped beam structure: Time histories of the $\vec{i}_3$ direction tip displacement components of both beams 209

Figure 9.30 Hinged, L-shaped beam structure: Time history of the $\vec{e}_2$ direction tip displacement component of beam 1, relative to, and measured in the triad associated with the root of beam 1 210

Figure 9.31 Hinged, L-shaped beam structure: Time history of the $\vec{e}_3$ direction root shear force in beam 1 211

Figure 9.32 Hinged, L-shaped beam structure: Spectrum of the $\vec{e}_3$ direction root shear force in beam 1 212

Figure 9.33 Hinged, L-shaped beam structure: Time history of the bending moment about the $\vec{e}_2$ axis in the root of beam 2 213

Figure 9.34 Hinged, L-shaped beam structure: Spectrum of the bending moment about the $\vec{e}_2$ axis in the root of beam 2 214

Figure 9.35 Hinged, L-shaped beam structure: Time history of normalized relative energy, $(E(t) - E_r)/E_r$ 215

Figure 9.36 Hinged, L-shaped beam structure: Time history energy increment ΔE 216

Figure 9.37 Hinged, L-shaped beam structure: Error in tip displacement vector of beam 1 (solid line) and beam 2 (dashed line) as a function of the number of steps 217

Figure 9.38 Hinged, L-shaped beam structure: Error in tip conformal rotation vector of beam 1 (solid line) and beam 2 (dashed line) as a function of the number of steps 218

Figure 9.39 Hinged, L-shaped beam structure: Error in internal force vector at the Gauss point closest to the root of beam 1 (solid line) and beam 2 (dashed line) as a function of the number of steps 219

Figure 9.40 Hinged, L-shaped beam structure: Error in internal moment vector at the Gauss point closest to the root of beam 1 (solid line) and beam 2 (dashed line) as a function of the number of steps 220

Figure 9.41 Hinged, L-shaped beam structure: Error in tip displacement vector of beam 1 (solid line) and beam 2 (dashed line) as a function of the CPU time 221

Figure 9.42 Hinged, L-shaped beam structure: Error in tip conformal rotation vector of beam 1 (solid line) and beam 2 (dashed line) as a function of the CPU time 222

Figure 9.43 Hinged, L-shaped beam structure: Error in internal force vector at the Gauss point closest to the root of beam 1 (solid line) and beam 2 (dashed line) as a function of the CPU time 223

Figure 9.44 Hinged, L-shaped beam structure: Error in internal moment vector at the Gauss point closest to the root of beam 1 (solid line) and beam 2 (dashed line) as a function of the CPU time 224

Figure 9.45 Flexible elbow mechanism: Motion and deformation of beams 225

Figure 9.46 Flexible elbow: Time histories of the $\vec{i}_1$ and $\vec{i}_2$ direction tip displacement components of both beams 226

Figure 9.47 Flexible elbow: Time histories of the $\vec{i}_3$ direction tip displacement components of both beams 227

Figure 9.48 Flexible elbow: Time history of the $\vec{e}_2$ direction tip displacement component of beam 1, relative to, and measured in the triad associated with the root of beam 1 228

Figure 9.49 Flexible elbow: Time history of the $\vec{i}_3$ direction tip displacement component of beam 1 229

Figure 9.50 Flexible elbow: Spectrum of the $\vec{i}_3$ direction tip displacement component of beam 1 230

Figure 9.51 Flexible elbow: Time history of axial force at root of beam 1 . 231

Figure 9.52 Flexible elbow: Time history of axial force at root of beam 2 . 232

Figure 9.53 Flexible elbow: Spectrum of axial force at root of beam 2 . . . 233

Figure 9.54 Flexible elbow: Time history of transverse shear force in $\vec{e}_2$ direction at root of beam 2 234

Figure 9.55 Flexible elbow: Spectrum of transverse shear force in $\vec{e}_2$ direction at root of beam 2 235

Figure 9.56 Flexible elbow: Time history of transverse shear force in $\vec{e}_3$ direction at root of beam 2 236

Figure 9.57 Flexible elbow: Spectrum of transverse shear force in $\vec{e}_3$ direction at root of beam 2 237

Figure 9.58 Swing comprising two rigid links and a beam with midspan mass 238

Figure 9.59 Swing: Motion and deformation of beam and motion of links, at 0.1 second intervals, with solid lines indicating positions at $t = 0$ and 1 seconds, and the locus of point A 239

Figure 9.60 Swing: Loci of five nodes on the beam 240

Figure 9.61 Swing: Time history of displacement components of point B in the (a) $\vec{i}_1$ and (b) $\vec{i}_3$ directions 241

Figure 9.62 Swing: Time history of axial force in the beam, at the Gauss point immediately to the left of the midspan mass 242

Figure 9.63 Swing: Time history of transverse shear force in the beam in the $\vec{e}_3$ direction, at the Gauss point immediately to the left of the midspan mass 243

Figure 9.64 Swing: Time history of normalized relative energy, $(E(t) - E_r)/E_r$ 244

Figure 9.65 Swing: Time history energy increment ΔE 245

ACKNOWLEDGEMENT

I would like to acknowledge with sincere gratitude the guidance, advice and encouragement received, over several years, from my thesis advisor, Prof. O. A. Bauchau. His help is deeply appreciated. I would also like to express my thanks to the members of the doctoral thesis examining committee for their time, effort and valuable suggestions: Prof. P. Hajela, Prof. A. Z. Lemnios, Prof. M. S. Shephard and Prof. S. S. Sternstein.

This research was sponsored by the US Army Research Office, under Grant Number DAAH04-93-G-0003; Dr. Robert E. Singleton is the contract monitor. This aid is acknowledged with gratitude.

I also received assistance from several colleagues and friends, for which I am very grateful: Dr. Nam Kook Kang, Dr. Guido Damilano, Dr. Carlo Bottasso, Minsup Lee, Taesok Joo, Ray Collar and Rao Garimella.

Throughout this study, I was encouraged and supported by my family, in particular wife, Ulinda. For this I am deeply grateful. Above all, I would like to give thanks to our Heavenly Father, who made all of this possible.

ABSTRACT

A helicopter rotor is a prime example of a non-linear multi-body dynamic system, in which various elastic bodies are interconnected with joints imposing kinematic constraints. The finite element method is chosen to model the rotor in non-linear multi-body dynamic analyses.

The most important elastic element in this case is the beam element, to model the blade. The three dimensional Saint-Venant beam theory is implemented to calculate the sectional properties of naturally curved and twisted composite beam sections of complex shape. This theory is expanded to allow the analysis of differential warping and a non-linear strain effect common to rotor blades. Various examples illustrate the use of both methods, and show their powerful capabilities.

The kinematic constraints are implemented through a Lagrange multiplier technique. This results in stiff, non-linear differential-algebraic equations, the numerical solution of which is plagued by spurious high frequency oscillations, unless a method with high frequency numerical dissipation is used. Conventional time integration schemes with high frequency numerical dissipation that were developed for linear systems, are regularly applied also to non-linear systems, however without any proof of unconditional stability. The energy preserving and energy decaying integration schemes are introduced. With these schemes, the equations of motion of the elastic bodies are discretized in such a way that the total energy of each body is preserved exactly, in the energy preserving scheme, or decays, in the energy decaying scheme. The forces of constraint associated with the kinematic constraints are discretized in such a way that they perform no work. The combination of these two features establishes the preservation or decay of the total energy of the system, thus implying unconditional stability in non-linear analysis.

The energy preserving scheme does not present any numerical dissipation. It

is shown that this often leads to high frequency oscillations that bury the useful information, cause convergence problems and render strict energy preservation impossible. The energy decaying scheme, even though more expensive, is shown to present numerical dissipation with asymptotic annihilation. This scheme is shown to be ideally suited for the integration of constrained multi-body dynamic systems.

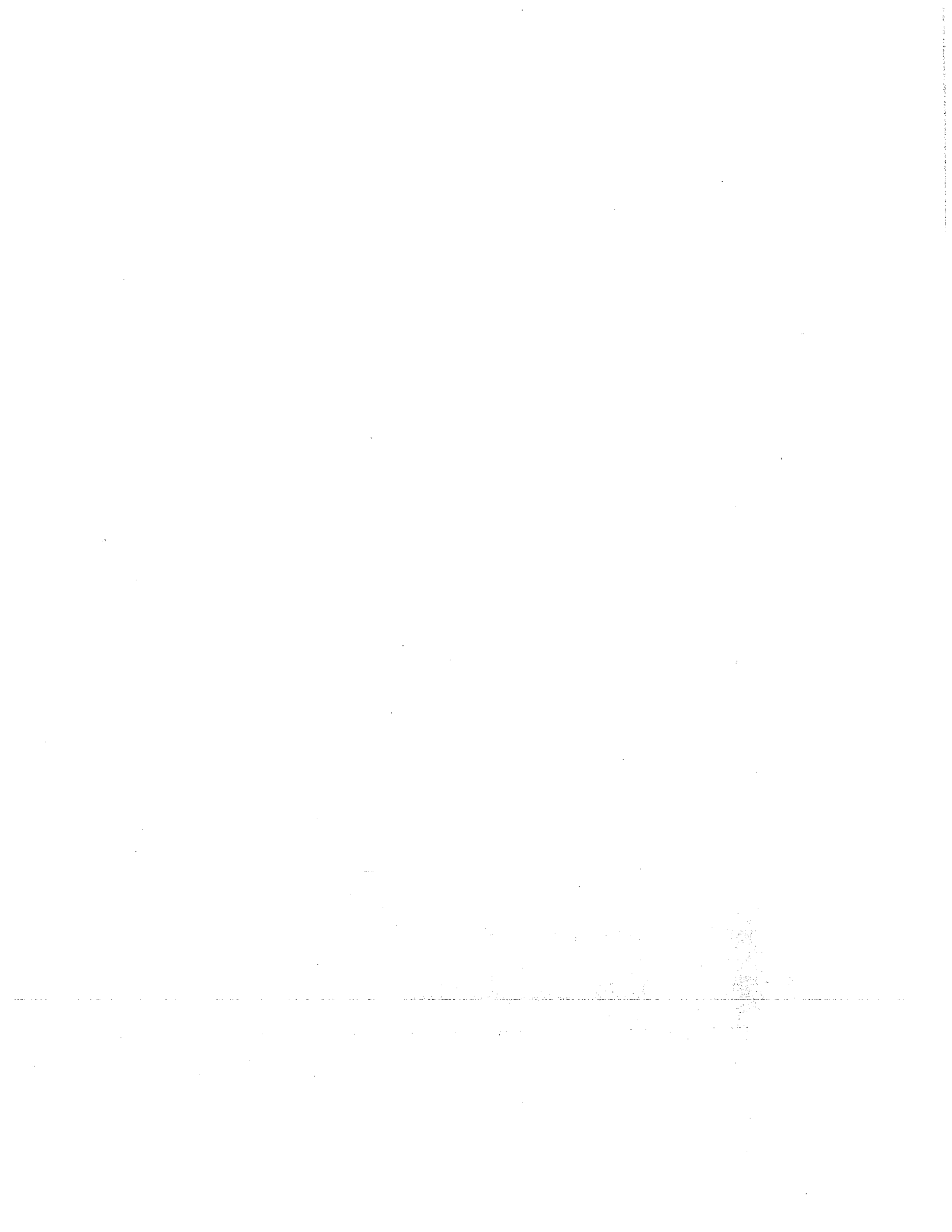

CHAPTER 1
INTRODUCTION AND HISTORICAL REVIEW

One important problem which the world helicopter industry faces is that of vibration reduction and control. In a conventional helicopter with one or more lifting rotors, the flow through the rotor has a large edgewise component in forward flight, which causes the aerodynamic loading to be cyclic. This cyclic rotor loading is the principal reason why vibration levels experienced in helicopters are generally much higher that those associated with fixed wing aircraft.

In the past the military has been the most important client of helicopter companies worldwide. Vibration reduction is very important in the case of military helicopters, in order to reduce fatigue in airframes, mechanical components and nowadays also electronic components, which are all the more frequently finding their way into modern military helicopters. Of course, vibration reduction is also important to increase crew endurance. With present worldwide reduction in military spending, however, helicopter companies are increasingly forced to look at the civil market for future sales. The lack of passenger comfort due to high vibration levels is considered as one important reason why the helicopter has not yet been able to significantly penetrate the passenger transport market.

Important in the quest to achieve "jet smooth" flight with helicopters is the ability to analyze the structural dynamics of the helicopter rotor, and also the rotor-fuselage structure. If the designer is able to accurately predict how the structure will respond under dynamic excitation in various flight conditions, he is in a much better position to devise ways to change those aspects of the response which are considered undesirable. Improving the structural dynamic analysis capability of the helicopter industry therefore goes hand in hand with achieving lower vibration levels in flight. In addition to the goal of vibration reduction, improved techniques

in structural dynamic analysis serve to enhance aeroelastic and mechanical stability analysis capability, which is very important from a safety point of view. The work described in this thesis was performed in an effort to make a positive contribution to the capability of the helicopter industry at large to perform structural dynamic analyses.

The helicopter rotor is a fairly complex structure of interconnected elastic bodies, most important of which are the rotor blades, pitch links, the swash plate mechanism, control rods or other control mechanisms, and the rotor shaft and hub. All helicopter rotor blades are connected to the hub via a system of "hinges". Whereas earlier designs, of which many aircraft are still in extensive use today, used roller bearing flap, lead-lag and pitch hinges, most recent designs tend to use either elastomeric bearings or flexible structural elements as "hinges". The flexible elements (typically beams and therefore often called "flexbeams") are significantly more flexible than the blade or the hub, and tend to distribute the hinge action over some spanwise distance, as opposed to elastomeric or roller element bearings which tend to concentrate the hinge action to specific locations. In designs which use roller bearing lead-lag hinges, and usually also in designs using elastomeric lead-lag hinges, a lead-lag damper is required to ensure stability. Considering all the above mentioned interacting components, it is clear that the helicopter rotor easily qualifies for description as an elastic multi-body system.

Quite often it is impossible to perform a structural dynamic analysis on the rotor in isolation. The multi-body system described above then needs to be expanded to include additional elastic bodies: the main gearbox with its suspension system, engines, interconnecting shafting, the non-rotating control mechanisms, and the tail rotor system: the tail rotor itself — which can be as complex as the main rotor — the tail rotor drive shaft and gear boxes, and the tail boom. The latest trends are to employ vibration absorption devices in the main gearbox suspension

systems. These devices are small multi-body systems in their own right. All of these components combine to form a single multi-body system in which there is a high level of dynamic interaction. This, to a large degree, precludes dynamic analysis on sub-system level. Finally, it may even be necessary to combine the modeling of all these components with a single fuselage model to be able to perform structural dynamic analyses on the aircraft as a whole.

The finite element method, due to its inherent modular nature, is very well suited to analyze complex dynamic multi-body systems. Two alternatives will be briefly mentioned. The first is an analytical approach, usually based on modal decomposition of the motion of elastic bodies. This type of analysis is fairly limited in scope and usually based on numerous simplifying assumptions, without which the analysis very quickly become unmanageable, and with which the results quite often do not correspond with reality. The recent emergence of symbolic computation has indeed opened up new horizons for this approach, and generally speaking it does offer an important advantage of clearer physical insight in the problem. Still, even with symbolic computation, the analytical approach does not match the versatility and accuracy of the finite element method.

The second method is a modal decomposition method, performed within a finite element environment. The finite element method is typically used to determine vibration mode shapes to be used in the modal basis. This method is currently fairly popular amongst helicopter manufacturers. It was investigated by Kang [1], who concluded that for multi-body analysis the full finite element analysis is more practical and cost effective. This thesis therefore concentrates on the use of the full finite element method in solving multi-body structural dynamic problems typical of helicopter rotors.

In structural dynamic analysis the modeling of the dynamic loading is of course very important. In the case of the helicopter, the most important contributor to

this is the aerodynamic loading, which can be exceedingly complex under most flight conditions. Today the most powerful method in modeling helicopter aerodynamics is Computational Fluid Dynamics (CFD). This field of study has great potential for determining the aerodynamic loading during structural dynamic analysis. CFD is also very well suited to complement finite element multi-body analysis, towards achieving the goal of a comprehensive helicopter analysis program. At this time, the aerodynamic and structural dynamic problems are modeled separately, each problem with its own, fully independent mesh structure. Interfaces are required between the structural and aerodynamic modeling, as they feed information to each other in a closed loop. Even though CFD is very important for determining the dynamic loading, it is not addressed any further in this thesis.

Multi-body systems can be broadly categorized into three problem types: multi-body systems consisting of a collection of rigid bodies in arbitrary motion with respect to each other; systems consisting of a collection of elastic bodies where the elastic displacements and rotations with respect to a body attached frame of reference are small; and finally systems consisting of a number of elastic bodies where elastic displacements and rotations can be arbitrarily large. The analysis methodologies that are optimum for each category vary widely.

This thesis is concerned with the analysis of nonlinear elastic multi-body systems, i.e. a collection of bodies in arbitrary motion with respect to each other while each body is undergoing large displacements and rotations with respect to a body attached frame of reference. The focus is on problems where the strains within each elastic body remain small.

Each elastic body is modeled using the finite element method. The use of beam elements will be demonstrated in this work.

1.1 The role of beam modeling in multi-body dynamic analysis of helicopter rotors

Helicopter rotor blades, being long, slender bodies, are particularly well suited to be modeled with beam elements during structural dynamic analysis with the finite element method. A beam element is essentially a one dimensional entity used to model a three dimensional structure in three dimensional space. It is based on a mathematical beam model, which determines the cross sectional strains, displacements and loads, as functions of a single variable describing the position along the beam reference line.

To understand the importance of beam elements, consider a typical modern rotor blade, made of composite materials. The most basic element that can be used to model a three dimensional structure like the blade is the three dimensional brick element. If it is required that the modeling of the blade be such that effects pertaining to the individual composite layers, like the stress or strain in the material, be captured with a fair degree of accuracy, a very fine mesh is required in the cross sectional plane. To obtain reasonable accuracy, it is important that the length to width and length to height ratios of the brick elements be within acceptable limits, typically five to one. It is therefore clear that the fine mesh in the cross sectional plane dictates a fine mesh also in the spanwise direction, which leads to a very large finite element model for a dynamic analysis, especially if this model is to be coupled with a CFD analysis.

Instead of using three dimensional brick elements to solve the above problem, a semi-discretization approach can be used, in which the three dimensional structure is discretized only with respect to the two dimensions corresponding to the cross sectional plane. This discretization is used to obtain cross sectional properties, which are functions only of the spanwise position of the cross section. These sectional properties can then be used in a subsequent multi-body dynamic analysis in which

the blade is modeled with beam elements. This means that the two dimensional cross sectional mesh may be refined to whatever level is required to capture local effects, without causing an increase in size of the multi-body dynamics finite element model. Furthermore, the two dimensional sectional analysis is performed only once for each different section, outside the loop in which the multi-body problem is solved at each time step. This constitutes a significant saving in computational time.

A comprehensive review of beam theories for modeling helicopter blades was recently published by Hodges [2]. The approach by Giavotto, Borri, et al. [3, 4] is probably the most comprehensive and has been extended considerably in [5]. A semi-discretization method, using a finite element sectional analysis, enables the determination of the sectional stiffness tensor for naturally curved and twisted beams, of arbitrary complex cross sectional definition, and made of anisotropic materials. This is done without making any limiting assumption on the sectional deformation other than a small strain assumption. Furthermore, this theory does not rely on the knowledge of the position of any special cross sectional point like the sectional shear center or axial stiffness centroid, and therefore allows an arbitrary location and orientation of the sectional axes system. This is an important advantage in the modeling of beams of which the sectional shear center and axial stiffness centroid changes drastically from one cross section to the next, in the spanwise direction. As part of this thesis, the theory of [5] was implemented in an existing finite element based multi-body dynamic analysis program. The theory developed by [3, 4, 5] is a natural extension of the classical Saint-Venant beam theory, allowing full three dimensional sectional warping, and is therefore referred to, in this thesis, as the *Three dimensional Saint-Venant beam theory.*

The classical Saint-Venant beam theory is the exact solution of the linear elasticity beam problem in the absence of differential warping, and under the assumption that the cross section does not deform in its own plane. Washizu [6] extended the

classical Saint Venant beam theory to model a beam with constrained torsional warping at the beam end (i.e. a differential warping problem). This was achieved by the introduction of an additional degree of freedom, which indicates to what extent the classical Saint-Venant torsional warping function supplements the rotation and displacement of the section in determining the total sectional displacement field. Bauchau et al. [7, 8] extended this methodology to use not only one warping function, but as many "eigenwarping" functions as necessary to achieve the desired accuracy. The three dimensional Saint-Venant beam theory is the exact solution of the linear elasticity beam problem in the absence of differential warping. It seems logical to also extend this theory to be able to analyze differential warping by introducing additional degrees of freedom which determine the participation of chosen warping functions in the sectional deformation, in the same manner as described above, with respect to the classical Saint-Venant beam theory. Such an extension has been developed as part of this work.

A non-linear beam theory allowing for exact geometric modeling of large rotations was developed by Bauchau, et al. [9, 10, 11, 1]. This non-linear beam theory will be used in the modeling of multi-body systems.

1.2 The role of the time integration methods in multi-body dynamic analysis

To perform a multi-body dynamic analysis implies that a time integration procedure is applied to solve the equations of motion of the elastic bodies in the system, and to ensure the satisfaction of all kinematic constraints. Various time integration schemes exist, and some are more suitable for multi-body dynamic analysis than others. Various factors have an influence on the choice of method. This section will introduce the most important of these issues.

In this work, the location of each node in the finite element mesh is represented

by its Cartesian coordinates in an inertial frame, and the rotation of the cross-section at each node is represented by a finite rotation tensor expressed in the same inertial frame. The kinematic constraints among the various bodies are enforced via the Lagrange multiplier technique. Though this approach does not involve the minimum set of coordinates [12], it allows a modular development of finite elements for the enforcement of the kinematic constraints. The representation of the displacements and rotation quantities in a single inertial frame remarkably simplifies the expression for the kinetic energy, as demonstrated by Simo [13].

The equations of motion resulting from the modeling of multi-body systems with the above methodology presents distinguishing features: they are stiff, non-linear, differential-algebraic equations. The stiffness of the system stems from the presence of high frequencies in the elastic members, but also from the infinite frequencies associated with the kinematic constraints. Indeed, no mass is associated with the Lagrange multipliers giving rise to algebraic equations coupled to the other equations of the system which are differential in nature.

The time integration of the resulting equations of motion give rise to a number of problems such as numerical instabilities and high frequency oscillations of a purely numerical origin. A thorough review of time integration schemes used in structural dynamics is found in [14]. The Newmark scheme [15] is a widely used scheme to integrate the equations of motion resulting from finite element discretizations. In particular, the average acceleration method, also known as the trapezoidal rule, is an unconditionally stable, second order accurate scheme when applied to linear problems. The classical stability analysis of this scheme can be readily found in text books [14] and shows that the spectral radius remains exactly equal to unity at all frequencies. An alternate way of proving stability is based on an energy argument. Indeed, it is easily shown that the average acceleration scheme exactly preserves the total energy of the system [18].

Geradin and Cardona [16] have shown that the Newmark scheme presents a weak instability when applied to constrained multi-body systems. The culprit is the presence of algebraic equations which are equivalent to infinite frequencies. Also, for large finite element discretizations, very high frequencies are present in the model and high frequency numerical dissipation is desirable, if not indispensable. Numerical dissipation cannot be introduced in the Newmark method without degrading the accuracy.

The Hilber-Hughes-Taylor (HHT) [17] scheme or α-method was introduced to eliminate the high frequency oscillations of a purely numerical origin resulting from the use of the Newmark scheme for large finite element problems. The HHT scheme alleviates this problem by introducing high frequency numerical dissipation. Geradin and Cardona [16] have shown that the use of this scheme in constrained multi-body problems can yield satisfactory system response. Numerical oscillations are observed in the time history response of accelerations, Lagrange multipliers, and velocities, though to a lesser extent. However, these high frequency oscillations are rapidly damped out. As the complexity of the constrained multi-body system increases, an increasing amount of numerical dissipation is required to avoid numerical instabilities and high frequency oscillations.

Following the HHT scheme, the generalized-α method [19] was introduced that achieves high frequency dissipation while minimizing unwanted low frequency dissipation. Both methods have been successfully used for both linear and nonlinear problems, though unconditional stability can only be proved for linear systems.

Though the approach of increasing the numerical damping to control high frequency oscillations and possible numerical instabilities is satisfactory, numerical oscillations are never completely eliminated. This raises a basic question: why introduce numerical dissipation to control the weak instability inherent to the Newmark scheme in the presence of infinite frequencies, rather than using a scheme that

behaves adequately in the presence of such frequencies?

An energy preserving scheme will be discussed for integration of beam equations. The algorithm presented here is similar to the energy preserving algorithms presented by Simo et al. for rigid body dynamics [20], and by the same author for elastodynamics [21]. The unconditional stability of these schemes stems from a proof of preservation of the total energy of the system.

Though energy preserving schemes perform well, it will be shown that their lack of high frequency numerical dissipation can be a problem. First, the time histories of internal forces and velocities can present a very significant high frequency content. Second, it seems that the presence of high frequency oscillations can hinder the convergence process for the solution of the nonlinear equations of motion. This was observed in several examples where the dynamic response of the system does involve significant high frequency content. The selection of a smaller time step does not necessarily help this convergence process, as a smaller time step allows even higher frequency oscillations to be present in the response. Finally, it seems that the presence of high frequency oscillations also renders strict energy preservation difficult to obtain. This could prove to be a real limitation of energy preserving schemes when applied to more and more complex models. For such models, the use of integration schemes presenting high frequency numerical dissipation becomes increasingly desirable. It seems that the idea from which the energy preserving scheme was born, in some cases also results in its downfall.

It appears that the development of "energy decaying" schemes, i.e. schemes eliminating the energy associated with vibratory motions at high frequency, is desirable. This is particularly important when dealing with large scale problems, or with problems presenting a complex dynamic response such as constrained multi-body problems.

The key to the development of an energy decaying scheme is the derivation of

an *energy decay inequality* [18] rather that the *discrete energy conservation law* which is central to energy preserving schemes. A methodology that can systematically lead to an energy decay inequality is the *time discontinuous Galerkin method* [22] which was initially developed for hyperbolic equations. Hughes and Hulbert [23, 24] have investigated the use of the time discontinuous Galerkin methodology for elastodynamics. They point out that: "classical elastodynamics can be converted to first-order symmetric hyperbolic form, which has proved useful in theoretical studies. Finite element methods for first order symmetric hyperbolic system are thus immediately applicable. However, there seems to be several disadvantages: in symmetric hyperbolic form the state vector consists of displacements, velocities, and stresses which is computationally uneconomical; and the generalization to nonlinear elastodynamics seems possible only in special circumstances." Indeed, writing the nonlinear equations of motion of beams in this symmetric hyperbolic form does not appear to be possible.

In this work an alternate, somewhat hybrid, route is taken. In a first phase, a standard time discontinuous Galerkin method is used to model a single degree of freedom linear oscillator. The equations of motion of this simple system can be readily cast into the symmetric hyperbolic form, and the energy decay inequality follows from the theory of the time discontinuous Galerkin method applied to hyperbolic conservation laws [25, 26]. However, the resulting discretized equations of motion can also be viewed as a finite difference scheme, and moreover, the energy decay inequality can be alternatively obtained by a direct computation of the work done by the discretized inertial and elastic forces over a time step. In other words, the time discontinuous Galerkin formulation is used to obtain a finite difference scheme which can then be proven to imply an energy decaying inequality without resorting to the formalism of the time discontinuous Galerkin method.

In a second phase, the nonlinear equations of motion of beams are discretized

in manner that mimics the finite difference scheme obtained for the linear oscillator. An energy decay inequality is then derived by a direct computation of the work done by the discretized inertial and elastic forces over a time step, mimicking once more the process used for linear oscillator.

The advantages of proceeding in this fashion are numerous. First, the nonlinear equations of motion need not be recast in the symmetric hyperbolic form, which does not seem possible in this case. Second, the state vector only consists of displacements and velocities. Furthermore, the velocities can be readily eliminated resulting in a set of equations solely involving displacements. Third, there is no need to numerically perform the time integrals that appear in the time discontinuous Galerkin formulation. Finally, a rigorous proof of unconditional stability for the nonlinear system is implied by the energy decay inequality. Numerical experimentation indicates that the salient features of the time discontinuous Galerkin method are inherited by the proposed scheme, in particular, unconditional stability for the nonlinear system, and high frequency numerical dissipation with asymptotic annihilation.

The use of an energy decaying scheme is particularly desirable when dealing with constrained multi-body systems. Indeed, typical multi-body systems comprise elastic members and a number of joints, which, from a modeling standpoint, can be viewed as kinematic constraints that must be satisfied together with the differential equations of motion of the elastic members. The presence of multiple constraints in multi-body system renders the system very stiff and increases the need for unconditionally stable integration schemes presenting high frequency numerical dissipation.

Considering the problem of the enforcement of kinematic constraints within the framework of energy decaying schemes, it once again seem impossible, as in the case of a nonlinear beam problem, to cast the kinematic constraint equations in the required first order symmetric hyperbolic form. To circumvent this problem

in the case of a nonlinear beam problem, an energy decay inequality is obtained by a direct computation of the work done by the inertial and elastic forces, as mentioned above. A similar path will be followed for the constraint equations: the forces of constraint will be discretized in such a way that the work they perform exactly vanishes when the constraint condition is exactly enforced. This way of proceeding has two advantages: first, the constraint condition is exactly enforced, and second, the energy decay inequality which guarantees the unconditional stability of the scheme is not upset by spurious numerical work performed by the forces of constraint.

With respect to the energy preserving/decaying scheme applied to multi-body dynamic systems, the two features, energy preservation/decay for elastic elements, and vanishing work of the constraint forces, result in preservation/decay of the total energy of the system, and numerical stability of the integration process is then guaranteed [14].

1.3 Objective and Layout of this thesis

The objective of this thesis is: (1) to implement the three dimensional Saint-Venant beam theory in an existing multi-body dynamic analysis program, based on the finite element method, (2) to derive and implement an extension to this theory to allow analysis in the presence of differential warping and a non-linear strain effect, and (3) to develop and implement a numerical time integration scheme for non-linear analysis of multi-body systems, which is unconditionally stable and presents numerical dissipation characteristics such that unwanted high frequency oscillations are attenuated while the dynamics of interest are not affected in any way.

To this end the thesis is organized in the following way: the beam and the revolute joint are selected as primary examples of an elastic body and a kinematic

constraint, respectively, for use in multi-body dynamic analysis of helicopter rotors. These two examples are used throughout this thesis for the derivation of the necessary theory. Chapter 2 presents the basic equations pertaining to these two examples: the equations of motion of a non-linear beam and the equations of constraint of a revolute joint.

Chapter 3 presents the three dimensional Saint-Venant beam theory and shows how the sectional stiffness tensor, used in the beam equations of motion, is determined. Chapter 4 derives the advanced beam theory, which allows the analysis of beams subjected to differential warping and a non-linear strain effect, and also shows how the sectional inertia tensor, used in the beam equations of motion, is determined. The next chapter presents various numerical examples which were used to validate the implementation of both the three dimensional Saint-Venant beam theory and the advanced beam theory, and it illustrates the use of the advanced beam element, based on the advanced beam theory.

Chapter 6 presents the discretization of finite rotations and the basic discretization of the equations of motion of a beam, which are used with respect to both the energy preserving and the energy decaying schemes. This chapter also introduces the energy preserving scheme for beams and shows how unconditional stability is guaranteed by this method. Chapter 7 discusses the time discontinuous Galerkin scheme for a single degree of freedom system, after which the energy decaying scheme for elastic bodies is modeled, and shows how the unconditional stability of this system can be proven based on an energy argument. It also points to the very favorable numerical dissipation characteristics of this scheme. This chapter finally introduces the energy decaying scheme for beams and shows the unconditional stability of this method based also on an energy argument.

Chapter 8 turns to the kinematic constraint and shows how a single degree of freedom system can be treated as a two degree of freedom system with a single

constraint. This is important, because it allows a clearer understanding of the discretization of a typical equation of constraint in such a way that the work done by the constraint force vanishes exactly, and the discretization of this very basic equation of constraint with the time discontinuous Galerkin method forms a useful parallel for finding the optimum discretization of the equations of constraint in the case of the energy decaying scheme. This chapter next returns to the example of the revolute joint. It presents the basic discretization of the equations of constraint of a revolute joint, which is used with respect to both the energy preserving and energy decaying schemes, and shows how implementing this basic discretization leads to the vanishing of all work done by the forces of constraint, first in the case of the energy preserving scheme, and finally in the case of the energy decaying scheme. The next chapter presents various numerical examples which illustrates the use of both the energy preserving and energy decaying schemes in multi-body dynamic analysis.

The final chapter derives some conclusions and recommendations for future work.

CHAPTER 2
EQUATIONS OF MOTION AND EQUATIONS OF CONSTRAINT

2.1 Introduction

The claim that the energy preserving scheme or decaying scheme for the time integration of multi-body systems is unconditionally stable in non-linear analyses, is based on the proof of preservation of, or decay in, the total energy of all the elastic bodies in the multi-body system, and the proof that the work done by all the discretized forces of constraint in the system vanishes exactly. That the total energy of all the elastic bodies in the system is preserved or decays can only be proven by showing this for each individual type of body, as such a proof is dependent on the equations of motion of each type of body, and the way that these equations are discretized. Likewise, that the work done by all the discretized forces of constraint in the system vanishes exactly can only be proven by showing this with respect to each type of constraint, as such a proof is dependent on the equations of constraint of each type of constraint and the way that these equations are discretized.

It would be impossible to treat all different types of elastic bodies and constraints in a single thesis. Instead, one example of each are chosen and the general theory is derived with reference to these chosen examples. The two examples that are chosen are, in the case of the elastic body, the beam, and in the case of the constraint, the revolute joint. Both the beam and the revolute joint are of prime importance in studying helicopter rotors as multi-body systems.

The equations of motion of a beam and the equations of constraint of a revolute joint will be derived in this chapter. It will be shown, in chapters 6 and 7, how the equations of motion of a beam are discretized so that the total energy is preserved or decays. Also, it will be shown, in chapter 8, how the equations of constraint of

a revolute joint are discretized so that the work done by the discretized forces of constraint vanishes exactly.

If any type of elastic body other than a beam needs to be modeled, a way to discretize the equations of motion of such a type of body needs to be found, that can be proven to imply preservation of, or decay in, energy. This can be done in a way quite similar to what will be shown for the beam. In the same way, if any type of constraint other than a revolute joint needs to be modeled, a way to discretize the equations of constraint of such a type of constraint needs to be found, that can be proven to imply the vanishing of the work done by the discretized forces of constraint. This can be done in a manner quite similar to what will be shown for the revolute joint.

In the modeling of multi-body systems it is of prime importance that no small rotation assumption is made, since the different bodies in such a system can in general be subjected to arbitrary large rotations with respect to each other and with respect to the inertial frame. It is therefore imperative that basic equations of motion, in the case of the beam, and equations of constraint, in the case of the revolute joint, which are all geometrically exact, are used as the basis of the multi-body dynamic analysis. Non-linear beam equations of motion which meet this requirement are derived in section 2.2, while geometrically exact equations of constraint for a revolute joint are derived in section 2.3.

2.2 Equations of motion of a non-linear beam.

Let $\vec{i}_1, \vec{i}_2$, and $\vec{i}_3$ form an inertial triad denoted $\mathcal{S}$; $\vec{e}_{01}, \vec{e}_{02}$, and $\vec{e}_{03}$ be a triad denoted $\mathcal{S}_0$ attached to the reference line of the beam before deformation; and $\vec{e}_1, \vec{e}_2$ and $\vec{e}_3$ a triad denoted $\mathcal{S}^*$ attached to the reference line of the beam after deformation. The planes formed by $\vec{e}_{02}, \vec{e}_{03}$, and $\vec{e}_2, \vec{e}_3$ define the plane of the cross-section of the beam before, and after deformation, respectively (see figure 2.1).

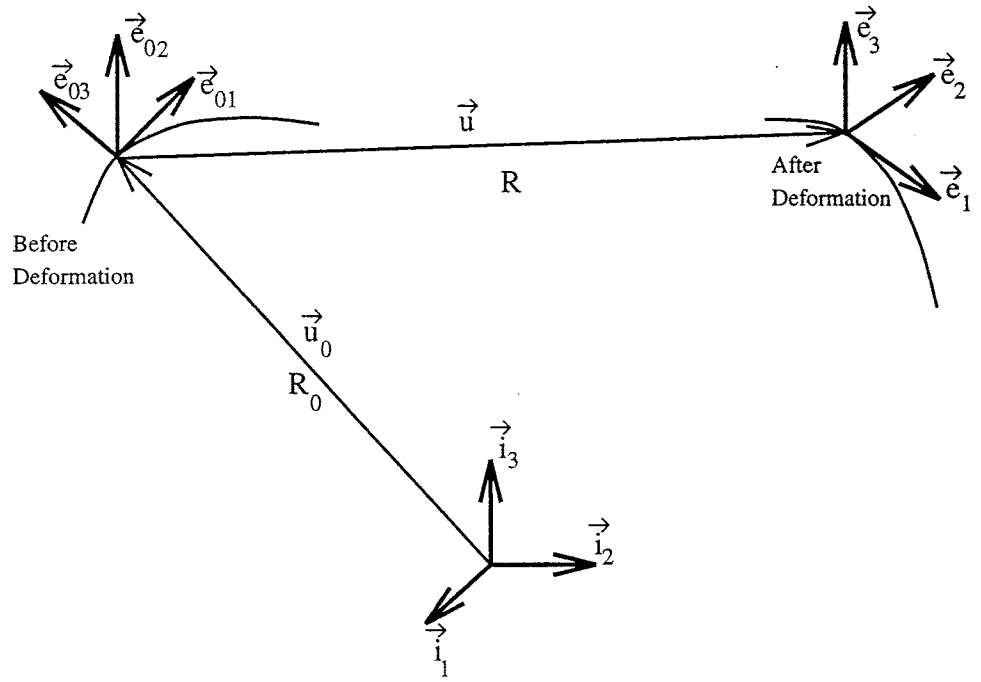

Figure 2.1: Beam reference line in undeformed and deformed position

The strain energy of the beam is written as:

$$V = \frac{1}{2} \int_0^L \underline{e}^{*T} C^* \underline{e}^* \, dx_1 \, , \tag{2.1}$$

where L is the length of the beam and x_1 the curvilinear coordinate along the reference line. C^* are the components of the sectional stiffness tensor and $\underline{e}^*$ the components of the sectional strain vector. Throughout this thesis an asterisk superscript indicates that components are measured in $\mathcal{S}^*$. A [0] superscript will be used to indicate tensor or vector components expressed in $\mathcal{S}_0$, while all 3 and 6 dimensional vectors and tensors expressed in component form in the $\mathcal{S}$ system do not have any superscript by default. This convention does not apply to higher dimensional vectors and matrices like those used in the finite element discretization, where the system in which components are measured is either specifically mentioned or is clear from the context. Also, an underlined symbol indicates a column vector.

The derivation of the sectional stiffness tensor C^* is discussed in chapter 3.

The sectional strains are related to the sectional displacements as:

$$\underline{e}^* = \mathcal{R}^T \underline{e} = \mathcal{R}^T \left| \begin{array}{c} (\underline{u}_o' + \underline{u}') - RR_0\underline{1} \\ \underline{k} \end{array} \right| ; \tag{2.2}$$

where

$$\mathcal{R} = \begin{bmatrix} RR_0 & 0 \\ 0 & RR_0 \end{bmatrix} , \tag{2.3}$$

and where $\underline{1}^T = \lfloor\ 1 \quad 0 \quad 0\ \rfloor$. The following quantities are all measured in $\mathcal{S}$: R_o defines the components of the rotation tensor from $\mathcal{S}$ to $\mathcal{S}_0$; R the components of the rotation tensor from $\mathcal{S}_0$ to $\mathcal{S}^*$; $\underline{u}_o$ the components of the position vector of a point on the reference line before deformation; $\underline{u}$ the components of the displacement vector of the deformed reference line with respect to the undeformed configuration; and $\underline{k}$ the components of the sectional elastic curvature vector, with $\tilde{k} = R'R^T$. Throughout this thesis the notation $(.)'$ is used to denote a derivative with respect to the spanwise curvilinear coordinate (in this chapter, and chapters 6 to 9: x_1), while the notation $\widetilde{(.)}$ is used to indicate the skew symmetric matrix used when the cross product of two vectors $\vec{b}$ and $\vec{a}$, $\vec{b} \times \vec{a}$, is expressed in component form as a matrix multiplication $\tilde{b}\underline{a}$.

The kinetic energy of the beam is expressed as:

$$K = \frac{1}{2} \int_0^L \underline{v}^{*T} M^* \underline{v}^* dx_1 , \tag{2.4}$$

where M^* are the components of the sectional inertia tensor, and $\underline{v}^*$ the components of the sectional velocity vector, both measured in $\mathcal{S}^*$.

Section 4.2.2 discusses the derivation of the sectional inertia tensor M^*, albeit for a more general case, but such that it can also apply, as a special case, to the sectional inertia tensor used in this chapter. The sectional velocities are related to the sectional displacements as:

$$\underline{v}^* = \mathcal{R}^T \underline{v} = \mathcal{R}^T \left| \begin{array}{c} \dot{\underline{u}} \\ \underline{\omega} \end{array} \right| ; \tag{2.5}$$

where $\underline{\omega}$ are the components of the sectional angular velocity, with $\tilde{\omega} = \dot{R}R^T$. Throughout this thesis a superposed dot denotes derivative with respect to time.

Virtual variations in sectional strains and velocities result in:

$$\delta\underline{e}^{*T} = \underline{\delta d}'^T\mathcal{R} + \underline{\delta d}^T\mathcal{U}\left[\left(\widetilde{u_o'} + \tilde{u}'\right)^T\right]\mathcal{R} \tag{2.6}$$

and

$$\delta\underline{v}^{*T} = \underline{\dot{\delta d}}^T\mathcal{R} + \underline{\delta d}^T\mathcal{U}\left[\tilde{\dot{u}}^T\right]\mathcal{R} \tag{2.7}$$

where $\underline{\delta d}^T = \left(\delta\underline{u}^T, \underline{\delta\psi}^T\right)$ are the virtual displacements and rotations measured in $\mathcal{S}$. The virtual rotation is defined as $\widetilde{\delta\psi} = \delta R R^T$, and

$$\mathcal{U}[.] = \begin{bmatrix} 0 & 0 \\ [.] & 0 \end{bmatrix} . \tag{2.8}$$

The equations of motion of the beam can be obtained from Hamilton's Principle that states:

$$\int_{t_i}^{t_f} (\delta K - \delta V + \delta W)\, dt = 0 , \tag{2.9}$$

where δW is the virtual work done by the externally applied forces. Introducing eqs. (2.1) and (2.4) into eq. (2.9) yields:

$$\int_{t_i}^{t_f} \left(\delta\underline{v}^{*T} M^* \underline{v}^* - \delta\underline{e}^{*T} C^* \underline{e}^{*T} + \delta W\right) dt = 0 . \tag{2.10}$$

Finally, the equations of motion are found by introducing eqs. (2.6) and (2.7) into eq. (2.10) to find:

$$\left(\mathcal{R}\underline{p}^*\right)^{\cdot} + \mathcal{U}\left[\tilde{\dot{u}}\right]\mathcal{R}\underline{p}^* - \left(\mathcal{R}\underline{f}^*\right)' - \mathcal{U}\left[\widetilde{u_o'} + \tilde{u}'\right]\mathcal{R}\underline{f}^* = \underline{q} ; \tag{2.11}$$

where the sectional momenta $\underline{p}^* = M^*\underline{v}^*$ and forces $\underline{f}^* = C^*\underline{e}^*$measured in $\mathcal{S}^*$ were defined.

The determination of the sectional stiffness and inertia tensors C^* and M^* are discussed in detail in chapters 3 and 4, respectively. The solution of the equations of motion of a non-linear beam is discussed in chapters 6 and 7.

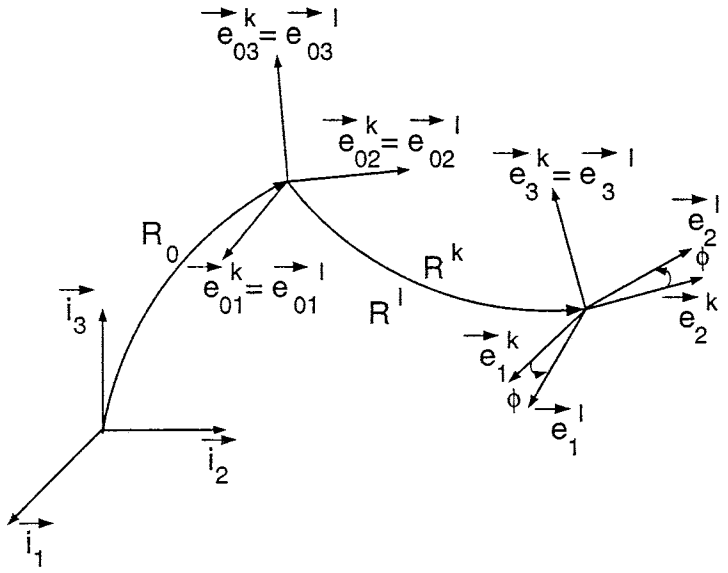

Figure 2.2: Kinematics of a revolute joint

2.3 Constraint equations for a revolute joint

Consider two bodies denoted "k" and "l" linked at a node by a revolute joint (see figure 2.2). In the undeformed configuration, the revolute joint is defined by two coincident triads $\mathcal{S}_0^k$ and $\mathcal{S}_0^l$ with unit vectors $\vec{e}_{0i}^{\,k} = \vec{e}_{0i}^{\,l}$. After deformation, the revolute joint is defined by two distinct triads $\mathcal{S}^k$ and $\mathcal{S}^l$ with unit vectors $\vec{e}_i^{\,k}$ and $\vec{e}_i^{\,l}$, respectively. Let the rotation matrices from $\mathcal{S}$ to $\mathcal{S}_0^k = \mathcal{S}_0^l$, $\mathcal{S}_0^k$ to $\mathcal{S}^k$, and $\mathcal{S}_0^l$ to $\mathcal{S}^l$ be R_0, R^k, and R^l, respectively, all measured in $\mathcal{S}$. The kinematic constraint corresponding to a revolute joint is the coincidence of $\vec{e}_3^{\,k}$ and $\vec{e}_3^{\,l}$. This can be written

$$\underline{\mathcal{C}}^T = \begin{bmatrix} \mathcal{C}_1 & \mathcal{C}_2 & \mathcal{C}_3 \end{bmatrix} = 0 \,, \tag{2.12}$$

where

$$\mathcal{C}_1 = \underline{e}_1^{lT}\underline{e}_3^k; \quad \mathcal{C}_2 = \underline{e}_2^{lT}\underline{e}_3^k; \quad \mathcal{C}_3 = \left(\underline{e}_1^{kT}\underline{e}_1^l\right)\sin\phi + \left(\underline{e}_1^{kT}\underline{e}_2^l\right)\cos\phi \,. \tag{2.13}$$

The third constraint $\mathcal{C}_3$ defines the relative rotation angle ϕ. These constraints are enforced via a Lagrange multiplier technique. The forces of constraint associated

with these constraints are:

$$\begin{aligned}
\underline{f}^k &= s\lambda_1 \widetilde{e_3^k}\underline{e}_1^l + s\lambda_2 \widetilde{e_3^k}\underline{e}_2^l + s\lambda_3 \widetilde{e_1^k}\left(\sin\phi\ \underline{e}_1^l + \cos\phi\ \underline{e}_2^l\right) \\
\underline{f}^l &= -s\lambda_1 \widetilde{e_3^k}\underline{e}_1^l - s\lambda_2 \widetilde{e_3^k}\underline{e}_2^l - s\lambda_3 \widetilde{e_1^k}\left(\sin\phi\ \underline{e}_1^l + \cos\phi\ \underline{e}_2^l\right) \qquad (2.14) \\
f^\phi &= s\lambda_3 \underline{e}_1^{kT}\left(\cos\phi\ \underline{e}_1^l - \sin\phi\ \underline{e}_2^l\right)
\end{aligned}$$

where $\underline{f}^k$ and $\underline{f}^l$ are the constraint moments applied on body "k" and "l", respectively, and f^ϕ the constraint force associated with the degree of freedom ϕ; λ_1, λ_2 and λ_3 the Lagrange multipliers used to enforce the constraint $\mathcal{C}_1$, $\mathcal{C}_2$ and $\mathcal{C}_3$, respectively, and s a scaling factor.

The implementation of the equations of constraint of a revolute joint in a time integration scheme is discussed in chapter 8.

CHAPTER 3
THREE DIMENSIONAL SAINT-VENANT BEAM THEORY

3.1 Introduction

Having decided that a beam model is appropriate for the analysis of helicopter rotor blades, the question is immediately raised: what cross sectional properties of the beam should be used, and how should these properties be determined? This chapter discusses the three dimensional Saint-Venant beam theory, which is the exact solution of the *linear elasticity* beam problem in the *absence of differential warping*. Under only these two limitations, this theory leads to the determination of a 6×6 sectional stiffness matrix, which fully determines the strain energy density of the beam. It will be argued that this stiffness matrix is in fact the sectional stiffness tensor C^* appearing in the equations of motion of the beam, eq. (2.11).

3.1.1 Compatibility of the three dimensional Saint-Venant beam theory with multi-body dynamic analysis

It should be noted that the theory presented in this chapter and in chapter 4 treats a more general case than the rest of this thesis, in the sense that the beam reference line is not assumed to be orthogonal to the plane of the cross section in the undeformed configuration. Whereas x_1, measured in the $\vec{e}_{01}$ direction in the undeformed configuration, is used as spanwise curvilinear coordinate in the rest of the thesis, ξ^1 is introduced in this chapter and also used in chapter 4 to signify this subtle difference.

It should also be pointed out that the definition of the sectional strain vector given in this chapter and also used in chapters 4 and 5, is different from the one given in chapter 2 and used in the rest of the thesis. To emphasize this difference,

two different symbols are used: $\underline{\varepsilon}^*$ for the sectional strain as defined in this chapter, and $\underline{e}^*$ for the sectional strain as defined in chapter 2, both in the $\mathcal{S}^*$ system. As mentioned in chapter 2, when the equations of motion of the beam are derived, it is necessary to account in a rigorous manner for all rotation, large or small; consequently the sectional strain vector is defined without resorting to any small rotation assumption. This means that the equations of motion of the beam are highly non-linear. The equations of motion are, however, derived using a small strain assumption; in fact, the very appearance of a stiffness tensor in a strain energy expression like eq. 2.1, when used in the derivation of equations of motion, indicates that all non-linearities are limited to the definition of the sectional strain, and that a linear sectional constitutive law is used, even though the beam theory itself is non-linear. The sectional strain vector defined in such a way that arbitrary large rotations can be accurately represented is indicated with the symbol $\underline{e}^*$.

In this chapter, on the other hand, the primary interest is merely to determine the sectional stiffness tensor, regardless of whether this tensor is to be used in a small rotation or large rotation environment. A small rotation assumption is indeed employed in the definition of the sectional strain vector, $\underline{\varepsilon}^*$, and consequently also in the derivation of the stiffness tensor. If, however, it can be shown that in the limit as the actual rotation is reduced, the sectional strain as defined without any small rotation assumption, $\underline{e}^*$, approaches the sectional strain obtained with such an assumption, $\underline{\varepsilon}^*$, the sectional stiffness tensor derived with the aid of the small rotation assumption may also be used in the more general large rotation case, even when rotations are large. The reason why this may be done is that the non-linearities of the non-linear theory is limited to the definition of the sectional strain, as pointed out above; the sectional stiffness tensor itself is independent of the sectional strain (otherwise there could not be any use of a linear sectional constitutive law).

It should be born in mind that in this chapter and chapters 4 and 5, the

symbol $\underline{u}$ is used to indicate the components of the displacement vector of *any* point in the beam, and the symbol $\underline{u}_s$ is used to indicate specifically the components of the sectional displacement vector. In the rest of this thesis, though, dealing only with a one dimensional beam, the s-subscript has been dropped from $\underline{u}_s$ so that $\underline{u}$ plainly expresses the components of the sectional displacement vector.

Finally, some of the equations used in the derivation of this theory hold true only with respect to the orientation of the beam in the undeformed configuration. Consequently, in deriving this theory, all the components are expressed in the $\mathcal{S}_0$ system. Yet, in the multi-body analysis these results need to be interpreted with respect to the $\mathcal{S}^*$ system, *without transformation.* The reason for this and why this may be done is explained at the end of section 3.5. To show, however, that the final objective of deriving this theory is in fact to serve the multi-body analysis, the problem statement of this chapter will now be given with components in $\mathcal{S}^*$.

3.1.2 The three dimensional Saint-Venant beam theory

In this chapter it will be shown that there exists a linear sectional constitutive law for beams of a certain class, $\underline{f}^* = C^*\underline{\varepsilon}^*$, such that the strain energy of the beam can be written as:

$$V = \frac{1}{2}\int_0^L \underline{f}^{*T}\underline{\varepsilon}^*\, d\xi^1 = \frac{1}{2}\int_0^L \underline{\varepsilon}^{*T} C^*\underline{\varepsilon}^*\, d\xi^1 \,, \tag{3.1}$$

where L is the length of the beam, ξ^1 the curvilinear coordinate along the reference line, C^* are the components of the sectional stiffness tensor, $\underline{\varepsilon}^*$ the components of the sectional strain vector and $\underline{f}^*$ the components of the sectional stress resultant vector, also called the beam internal forces or merely the sectional forces.

In deriving the three dimensional Saint-Venant beam theory, two distinct solution types are observed: the extremity solution and the central solution [3]. The extremity solution consists of an infinite number of solutions that decay with distance from the end points of the beam, whereas the central solution consists of a

fixed set of the non-decaying solutions which determine sectional properties.

A helicoidal beam, as defined in section 3.2, is used to derive the three dimensional Saint-Venant beam theory. With respect to the central solution, the following assumptions are made: (1) spanwise homogeneity of properties like curvature, sectional dimensions and material properties, (2) no loading of the beam at points other than its end points, where the loads are distributed over the end cross sections in the ideal manner[1], (3) no physical constraint on any warping at any point in the beam, and (4) strains are small, so that higher order strain terms may be neglected, compared to first order terms.

The second assumption precludes any distributed loading, like inertial and gravitational loading due to the distributed mass of the beam. One may visualize the beam which is considered under the second and third assumptions as a free-free beam, in static equilibrium in a zero-force field, subjected to end point loading. The limitation imposed by the third assumption and an aspect of the fourth assumption are addressed in chapter 4. The limitations imposed by the first and second assumptions do not prevent application of the results to general curvilinear finite beam elements, because (1) satisfactory results can be obtained in the case of non-homogeneous spanwise properties by the standard finite element interpolation of the cross sectional properties at the various elemental nodes, and (2) the theory is a linear theory, which means that the resulting stiffness tensor is independent not only of the sectional strain, as pointed out above, but also of the beam loading, and can therefore also be applied to beams which carries loads at locations other than the end points.

The derivation of the three dimensional Saint-Venant beam theory starts with a discussion of the helicoidal beam, the favorable geometric properties of which are used to establish a theory for treating naturally curved and twisted beams. The one

[1]At this stage it is sufficient to say that a non-ideal distribution of the loads on the end cross sections would excite the extremity solution.

dimensional equilibrium equations and the three dimensional strain-displacement relationship for such a beam are derived. The principle of virtual work is then applied to an infinitesimally thin slice of the beam, to obtain a set of second order multivariable differential equations, which can be solved in order to find the cross sectional compliance tensor. Having determined this tensor, the sectional stiffness tensor is readily calculated by inversion of the compliance tensor. Next, stress and strain recovery equations are derived, to enable the calculation of the full three dimensional state of stress or strain at any point on the cross section (and thus any point in the beam), for a given sectional stress resultant. Finally, the strain energy expression of the beam is derived, which was set as goal for this chapter in the beginning of this section.

3.2 The Helicoidal Beam

Consider a naturally curved and twisted beam, of which the position of the undeformed reference line is described by $\vec{x}_0(\xi^1)$, where ξ^1 is a curvilinear coordinate measured along the reference line. Let, at an arbitrary point along the reference line, its curvature vector be given by $\vec{c}$ and be expressed in the $\mathcal{S}$ and $\mathcal{S}_0$ systems by $\underline{c}$ and $\underline{c}^{[0]}$, respectively. Also, let the unit vector tangent to the reference line at this point be given by $\vec{t}$ and expressed in the $\mathcal{S}$ and $\mathcal{S}_0$ systems by $\underline{t}$ and $\underline{t}^{[0]}$, respectively. A helicoidal beam is defined as a beam for which $\frac{d}{d\xi^1}\left(\vec{t}\cdot\vec{e}_i\right) = 0$ and $\frac{d}{d\xi^1}\left(\vec{c}\cdot\vec{e}_i\right) = 0\ ,\ \ i = 1\ldots 3$. Since

$$\frac{d\vec{e}_i}{d\xi^1} = \vec{c}\times\vec{e}_i\ \ ,\ \ i = 1\ldots 3,$$

it follows that for a helicoidal beam

$$\frac{d\vec{t}}{d\xi^1} = \vec{c}\times\vec{t} \tag{3.2}$$

and

$$\frac{d\vec{c}}{d\xi^1} = 0\ . \tag{3.3}$$

In this section the one dimensional equilibrium equations, which relate the stress resultant components at any section at ξ^1 to the components at the origin $\xi^1 = 0$, and the three dimensional strain-displacement relationship, for a helicoidal beam, are derived.

3.2.1 One dimensional equilibrium equations

Using relationships (3.2) and (3.3), Borri et al. [5] shows that the one dimensional equilibrium equations of a helicoidal beam loaded only at its two end points can be written as:

$$\frac{d\underline{f}^{[0]}}{d\xi^1} + \mathcal{T}\underline{f}^{[0]} = 0 \tag{3.4}$$

where $\underline{f}^{[0]}$ is the column vector containing the six internal stress resultants in the local system, i.e. the axial force, transverse shear forces in the $\vec{e}_{02}$ and $\vec{e}_{03}$ directions, the torsional moment and bending moments, about the $\vec{e}_{02}$ and $\vec{e}_{03}$ axes, and where

$$\mathcal{T} = \begin{bmatrix} \tilde{c}^{[0]} & 0 \\ \tilde{t}^{[0]} & \tilde{c}^{[0]} \end{bmatrix} .$$

Using relationships (3.2) and (3.3) it can be shown that $\underline{c}^{[0]} = \underline{c}$ and $\underline{t}^{[0]} = \underline{t}(0)$ are both constant in ξ^1. Therefore, $\mathcal{T}$ is a constant matrix, having the following property:

$$\mathcal{T}^6 + 2c^2\mathcal{T}^4 + c^4\mathcal{T}^2 = 0 ,$$

where $c = \sqrt{\underline{c}^T\underline{c}}$. Following [5], a differential equation is obtained for the internal stress resultants:

$$\frac{d^6\underline{f}^{[0]}}{d\xi^{1\,6}} + 2c^2\frac{d^4\underline{f}^{[0]}}{d\xi^{1\,4}} + c^4\frac{d^2\underline{f}^{[0]}}{d\xi^{1\,2}} = 0 . \tag{3.5}$$

The solution to this differential equation is:

$$\underline{f}^{[0]}(\xi) = (\underline{A}_0 + \underline{B}_0 c\xi^1) + (\underline{A}_c + \underline{B}_c c\xi^1)\cos(c\xi^1) + (\underline{A}_s + \underline{B}_s c\xi^1)\sin(c\xi^1) \tag{3.6}$$

where $c\xi^1$ is the angle through which the cross section is rotated with respect to the cross section orientation at $\xi^1 = 0$, and the constant vectors are given by:

$$\underline{A}_0 = \left[I + \frac{2}{c^2}\mathcal{T}^2 + \frac{1}{c^4}\mathcal{T}^4\right] \underline{f}^{[0]}(0) \tag{3.7}$$

$$\underline{B}_0 = -\frac{1}{c}\mathcal{T}\left[I + \frac{2}{c^2}\mathcal{T}^2 + \frac{1}{c^4}\mathcal{T}^4\right] \underline{f}^{[0]}(0) \tag{3.8}$$

$$\underline{A}_c = -\frac{1}{c^2}\mathcal{T}^2\left[2I + \frac{1}{c^2}\mathcal{T}^2\right] \underline{f}^{[0]}(0) \tag{3.9}$$

$$\underline{B}_c = -\frac{1}{2c^3}\mathcal{T}^3\left[I + \frac{1}{c^2}\mathcal{T}^2\right] \underline{f}^{[0]}(0) \tag{3.10}$$

$$\underline{A}_s = \frac{1}{2c^3}\mathcal{T}^3\left[5I + \frac{3}{c^2}\mathcal{T}^2\right] \underline{f}^{[0]}(0) \tag{3.11}$$

$$\underline{B}_s = -\frac{1}{2c^2}\mathcal{T}^2\left[I + \frac{1}{c^2}\mathcal{T}^2\right] \underline{f}^{[0]}(0)\,. \tag{3.12}$$

3.2.2 Three dimensional strain-displacement relationship

A curvilinear material axes system is now defined. Following the Lagrangian approach [27, pages 52 and 76], the coordinates of a generic material point ξ^1, ξ^2 and ξ^3 in the undeformed configuration are used to describe the position of the point throughout its deformation, where in the undeformed configuration ξ^2 and ξ^3 are measured along $\vec{e}_{02}$ and $\vec{e}_{03}$ respectively. A second, locally orthogonal, curvilinear axes system can also be defined at ξ^1, by measuring α^1 along $\vec{e}_{01}$, α^2 along $\vec{e}_{02}$ and α^3 along $\vec{e}_{03}$.

Consider a generic material point P, as indicated in figure 3.1, of which the position in the undeformed and deformed configuration is given by

$$\vec{x}(\xi^1,\xi^2,\xi^3) = \vec{x}_0(\xi^1) + \xi^2\vec{e}_{02} + \xi^3\vec{e}_{03} = \vec{x}_0 + \vec{b}$$

and

$$\vec{\mathcal{X}}(\xi^1,\xi^2,\xi^3) = \vec{x}(\xi^1,\xi^2,\xi^3) + \vec{u}(\xi^1,\xi^2,\xi^3)$$

respectively, where $\vec{b} = \xi^2\vec{e}_{02} + \xi^3\vec{e}_{03}$ is the position vector of P in the plane of the cross section, relative to the beam reference line, and $\vec{u}$ is the displacement of P during deformation.

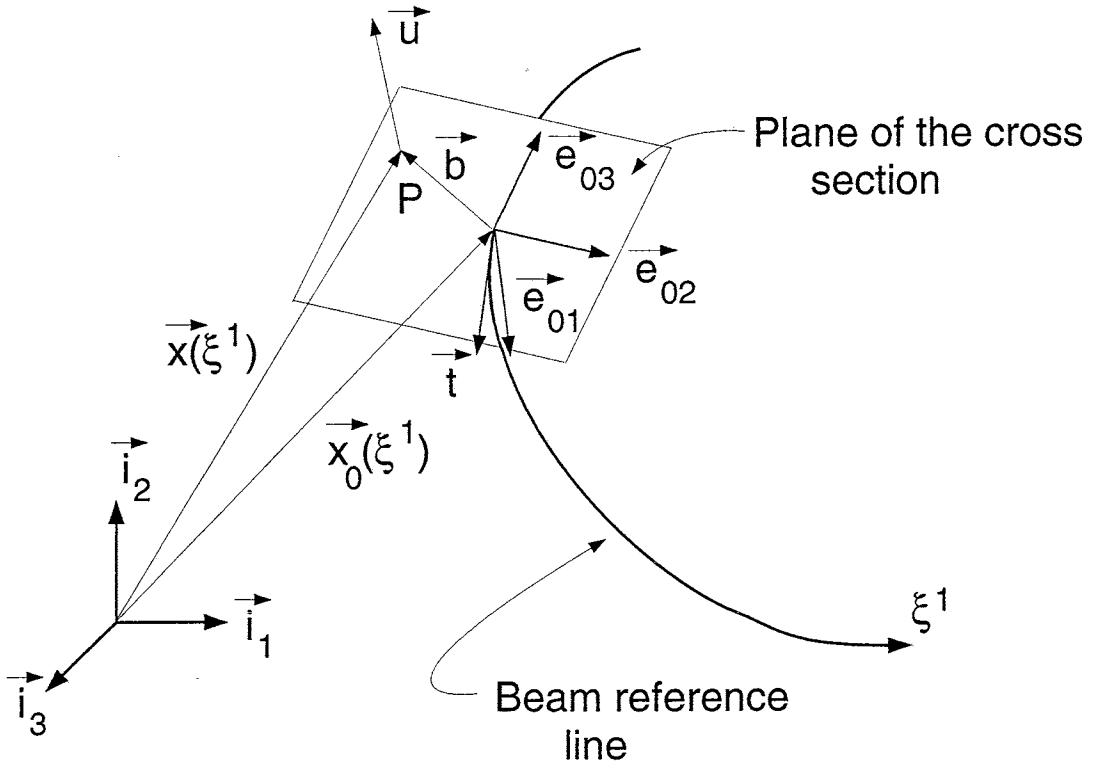

Figure 3.1: The beam reference line, cross section and generic point P, in the plane of the cross section, in the undeformed configuration

The base vectors [27, pages 76–80] associated with P in the undeformed configuration, expressed in the $\mathcal{S}_0$ system, are given by:

$$\underline{g}_1^{[0]} = \left| \begin{array}{c} t_1 + c_2\xi^3 - c_3\xi^2 \\ t_2 - c_1\xi^3 \\ t_3 + c_1\xi^2 \end{array} \right| ; \underline{g}_2^{[0]} = \left| \begin{array}{c} 0 \\ 1 \\ 0 \end{array} \right| ; \underline{g}_3^{[0]} = \left| \begin{array}{c} 0 \\ 0 \\ 1 \end{array} \right| .$$

The metric tensor $g_{ij} = g_{ji}$ associated with P in the undeformed configuration is given by:

$$g_{11} = g + \beta_2^2 + \beta_3^2 \; ; \; g_{12} = -\beta_2$$

$$g_{13} = -\beta_3 \; ; \; g_{22} = g_{33} = 1 \; ; \; g_{23} = 0$$

where $g = (t_1 + c_2\xi^3 - c_3\xi^2)^2 = \det(g_{ij})$, $\beta_2 = -(t_2 - c_1\xi^3)$ and $\beta_3 = -(t_3 + c_1\xi^2)$.

The base vectors associated with P in the deformed configuration, expressed in the $\mathcal{S}_0$ system, are given by:

$$\underline{G}_1^{[0]} = \left| \begin{array}{l} \sqrt{g} + \dfrac{\partial u_1}{\partial \xi^1} - c_3u_2 + c_2u_3 \\ -\beta_2 + \dfrac{\partial u_2}{\partial \xi^1} + c_3u_1 - c_1u_3 \\ -\beta_3 + \dfrac{\partial u_3}{\partial \xi^1} - c_2u_1 + c_1u_2 \end{array} \right|$$

$$\underline{G}_2^{[0]} = \left| \begin{array}{c} \dfrac{\partial u_1}{\partial \xi^2} \\ 1 + \dfrac{\partial u_2}{\partial \xi^2} \\ \dfrac{\partial u_3}{\partial \xi^2} \end{array} \right| ; \underline{G}_3^{[0]} = \left| \begin{array}{c} \dfrac{\partial u_1}{\partial \xi^3} \\ \dfrac{\partial u_2}{\partial \xi^3} \\ 1 + \dfrac{\partial u_3}{\partial \xi^3} \end{array} \right| ,$$

where $\underline{u}^{[0]T} = \lfloor \, u_1 \;\; u_2 \;\; u_3 \, \rfloor$ are the components of $\vec{u}$ in $\mathcal{S}_0$. The metric tensor $G_{ij} = G_{ji}$ associated with P in the deformed configuration is given by:

$$G_{11} = \left(\sqrt{g} + \frac{\partial u_1}{\partial \xi^1} - c_3u_2 + c_2u_3 \right)^2 + \left(\frac{\partial u_2}{\partial \xi^1} - \beta_2 + c_3u_1 - c_1u_3 \right)^2$$

$$
\begin{aligned}
&+\left(\frac{\partial u_3}{\partial \xi^1}-\beta_3-c_2u_1+c_1u_2\right)^2\\
G_{12} &= \left(\sqrt{g}+\frac{\partial u_1}{\partial \xi^1}-c_3u_2+c_2u_3\right)\frac{\partial u_1}{\partial \xi^2}+\left(\frac{\partial u_2}{\partial \xi^1}-\beta_2+c_3u_1-c_1u_3\right)\left(1+\frac{\partial u_2}{\partial \xi^2}\right)\\
&+\left(\frac{\partial u_3}{\partial \xi^1}-\beta_3-c_2u_1+c_1u_2\right)\frac{\partial u_3}{\partial \xi^2}\\
G_{13} &= \left(\sqrt{g}+\frac{\partial u_1}{\partial \xi^1}-c_3u_2+c_2u_3\right)\frac{\partial u_1}{\partial \xi^3}+\left(\frac{\partial u_2}{\partial \xi^1}-\beta_2+c_3u_1-c_1u_3\right)\frac{\partial u_2}{\partial \xi^3}\\
&+\left(\frac{\partial u_3}{\partial \xi^1}-\beta_3-c_2u_1+c_1u_2\right)\left(1+\frac{\partial u_3}{\partial \xi^3}\right)\\
G_{22} &= \left(\frac{\partial u_1}{\partial \xi^2}\right)^2+\left(1+\frac{\partial u_2}{\partial \xi^2}\right)^2+\left(\frac{\partial u_3}{\partial \xi^2}\right)^2\\
G_{33} &= \left(\frac{\partial u_1}{\partial \xi^3}\right)^2+\left(\frac{\partial u_2}{\partial \xi^3}\right)^2+\left(1+\frac{\partial u_3}{\partial \xi^3}\right)^2\\
G_{23} &= \frac{\partial u_1}{\partial \xi^2}\frac{\partial u_1}{\partial \xi^3}+\left(1+\frac{\partial u_2}{\partial \xi^2}\right)\frac{\partial u_2}{\partial \xi^3}+\frac{\partial u_3}{\partial \xi^2}\left(1+\frac{\partial u_3}{\partial \xi^3}\right)\ .
\end{aligned}
$$

The Green-Lagrange strain tensor [27, page 81], expressed in the (ξ^1,ξ^2,ξ^3) system, can now be calculated as $f_{ij}=\frac{1}{2}(G_{ij}-g_{ij})$. The strain tensor ϵ_{ij} in the locally orthogonal system $(\alpha^1,\alpha^2,\alpha^3)$ is obtained by a strain transformation

$$\epsilon_{ij}=f_{kl}\frac{\partial \xi^k}{\partial \alpha^i}\frac{\partial \xi^l}{\partial \alpha^j}\ ;$$

where repeated indices imply summation, as is usual with tensor notation, and where

$$\frac{\partial \xi^1}{\partial \alpha^1}=\frac{1}{\sqrt{g}}\ ;\ \frac{\partial \xi^2}{\partial \alpha^2}=\frac{\partial \xi^3}{\partial \alpha^3}=1$$

$$\frac{\partial \xi^2}{\partial \alpha^1}=\frac{\beta_2}{\sqrt{g}}\ ;\ \frac{\partial \xi^3}{\partial \alpha^1}=\frac{\beta_3}{\sqrt{g}}$$

$$\frac{\partial \xi^1}{\partial \alpha^2}=\frac{\partial \xi^3}{\partial \alpha^2}=\frac{\partial \xi^1}{\partial \alpha^3}=\frac{\partial \xi^2}{\partial \alpha^3}=0\ .$$

The three dimensional Saint-Venant beam theory is a linear theory, based on a small strain assumption. If, in line with this assumption, all the second order strain terms $\frac{\partial u_i}{\partial \xi^j}\frac{\partial u_k}{\partial \xi^l}$, $\frac{\partial u_i}{\partial \xi^j}c_ku_l$ and $c_iu_jc_ku_l$ are neglected as small, compared to the first

order terms, the three dimensional strain field expressed in the locally orthogonal system is given by:

$$\underline{\epsilon}^{[0]} = \mathcal{D}\underline{u}^{[0]} + \mathcal{F}\underline{u}^{[0]\prime}, \tag{3.13}$$

where $\underline{\epsilon}^{[0]T} = \lfloor\ \epsilon_{11}\ \ 2\epsilon_{12}\ \ 2\epsilon_{13}\ \ \epsilon_{22}\ \ \epsilon_{33}\ \ 2\epsilon_{23}\ \rfloor$ and $\underline{u}^{[0]T\prime} = \left\lfloor\ \frac{\partial u_1}{\partial \xi^1}\ \ \frac{\partial u_2}{\partial \xi^1}\ \ \frac{\partial u_3}{\partial \xi^1}\ \right\rfloor$, and where the two linear operator matrices $\mathcal{D}$ and $\mathcal{F}$ are given by:

$$\mathcal{D} = \frac{1}{\sqrt{g}} \begin{bmatrix} \beta_2\frac{\partial}{\partial \xi^2} + \beta_3\frac{\partial}{\partial \xi^3} & -c_3 & c_2 \\ c_3 + \sqrt{g}\frac{\partial}{\partial \xi^2} & \beta_2\frac{\partial}{\partial \xi^2} + \beta_3\frac{\partial}{\partial \xi^3} & -c_1 \\ -c_2 + \sqrt{g}\frac{\partial}{\partial \xi^3} & -c_1 & \beta_2\frac{\partial}{\partial \xi^2} + \beta_3\frac{\partial}{\partial \xi^3} \\ 0 & \sqrt{g}\frac{\partial}{\partial \xi^2} & 0 \\ 0 & 0 & \sqrt{g}\frac{\partial}{\partial \xi^3} \\ 0 & \sqrt{g}\frac{\partial}{\partial \xi^3} & \sqrt{g}\frac{\partial}{\partial \xi^2} \end{bmatrix}$$

and

$$\mathcal{F} = \frac{1}{\sqrt{g}} \begin{bmatrix} 1 & 0 & 0 \\ 0 & 1 & 0 \\ 0 & 0 & 1 \\ 0 & 0 & 0 \\ 0 & 0 & 0 \\ 0 & 0 & 0 \end{bmatrix}.$$

3.3 Central Solution

In this section the central solution associated with the three dimensional Saint-Venant beam theory is derived, following almost exactly the derivation given in [5].

3.3.1 Principle of Virtual Work

Consider the infinitesimally thin disk of material between the cross sectional planes at ξ^1 and $\xi^1 + d\xi^1$ as an elastic body, to which the principle of virtual work may be applied. Due to the assumption of no external loading along the span of the beam, the only external loads acting on the disk are the stresses $-\underline{p}^{[0]}$ and $\underline{p}^{[0]} + d\underline{p}^{[0]}$ acting on the cross sectional faces at ξ^1 and $\xi^1 + d\xi^1$ respectively. The virtual work done by these external stresses under virtual displacements $\delta\underline{u}^{[0]}$ at ξ^1 and $\delta(\underline{u}^{[0]} + d\underline{u}^{[0]})$ at $\xi^1 + d\xi^1$ is given by $\left(\int_A (\delta\underline{u}^{[0]T}\underline{p}^{[0]})'\, dA\right) d\xi^1$, where in this chapter and chapters 4 and 5 $(.)'$ indicates the partial derivative with respect to ξ^1, and A is the area of the cross section. The virtual work done by the internal stresses, in the case of a material obeying Hooke's Law, is $\left(\int_A \delta\underline{\epsilon}^{[0]T} D^{[0]} \underline{\epsilon}^{[0]} \sqrt{g}\, dA\right) d\xi^1$, where $\delta\underline{\epsilon}^{[0]}$ are the six virtual strain components corresponding to the virtual displacement field, g is the metric tensor determinant defined in section 3.2.2, and $D^{[0]}$ is the order 6 material stiffness matrix. The principle of virtual work applied to the disk may then be written as:

$$\delta W = d\xi^1 \int_A \delta\underline{\epsilon}^{[0]T} D^{[0]} \underline{\epsilon}^{[0]} \sqrt{g}\, dA - d\xi^1 \int_A (\delta\underline{u}^{[0]T}\underline{p}^{[0]})'\, dA = 0\,. \tag{3.14}$$

The displacement field of the section at ξ^1 can be semi-discretized, using a two dimensional finite element mesh of the section, containing n nodes:

$$\underline{u}^{[0]}(\xi^1, \xi^2, \xi^3) = N(\xi^2, \xi^3)\underline{U}(\xi^1)\,, \tag{3.15}$$

where $\underline{U}(\xi^1)$ is the $3n$-dimensional column vector of nodal displacement components in all three axes directions $\vec{e}_{01}$, $\vec{e}_{02}$ and $\vec{e}_{03}$, and $N(\xi^2, \xi^3)$ are the standard two dimensional interpolation functions.

Using discretization (3.15), the strain field, eq. (3.13), can be semi-discretized as:

$$\underline{\epsilon}^{[0]} = B\underline{U} + \bar{A}\underline{U}'\,, \tag{3.16}$$

where $B = \mathcal{D}N$ and $\bar{A} = \mathcal{F}N$.

Substituting eqs. (3.15) and (3.16) into eq. (3.14) results in:

$$\delta\underline{U}^T(E\underline{U} + C\underline{U}' - \underline{P}') + \delta\underline{U}'^T(C^T\underline{U} + M\underline{U}' - \underline{P}) = 0\,, \tag{3.17}$$

where

$$\begin{aligned} E &= \int_A B^T D^{[0]} B\sqrt{g}\,dA \qquad C = \int_A B^T D^{[0]} \bar{A}\sqrt{g}\,dA \\ M &= \int_A \bar{A}^T D^{[0]} \bar{A}\sqrt{g}\,dA \qquad \underline{P} = \int_A N^T \underline{p}^{[0]}\,dA\,. \end{aligned} \tag{3.18}$$

From a practical implementation point of view, the sectional area integrals in the above equation implies the procedure usual to finite element analysis, where the integrals are calculated separately for each element and then assembled into the global matrices. Eq. (3.17) implies

$$E\underline{U} + C\underline{U}' = \underline{P}' \tag{3.19}$$

$$C^T\underline{U} + M\underline{U}' = \underline{P}\,. \tag{3.20}$$

As shown by Borri et al. [5], these two equations can be combined into a single second order multivariable homogeneous differential equation with constant coefficients, the corresponding eigensolution of which can be classified into two groups: six purely imaginary eigenvalues corresponding to non-zero stress resultants, which constitutes the central solution, and the eigenvalues with non-zero real parts, which represent exponentially decaying self-equilibrating modes, constituting the extremity solution. The three dimensional Saint-Venant beam theory essentially deals with the central solution, so that no further attention is given to the extremity solution in this chapter, and it is addressed only briefly in chapter 4. The central solution, on the other hand, is obtained more easily through an approach different from the above mentioned eigenanalysis; this approach will be discussed in the rest of this chapter.

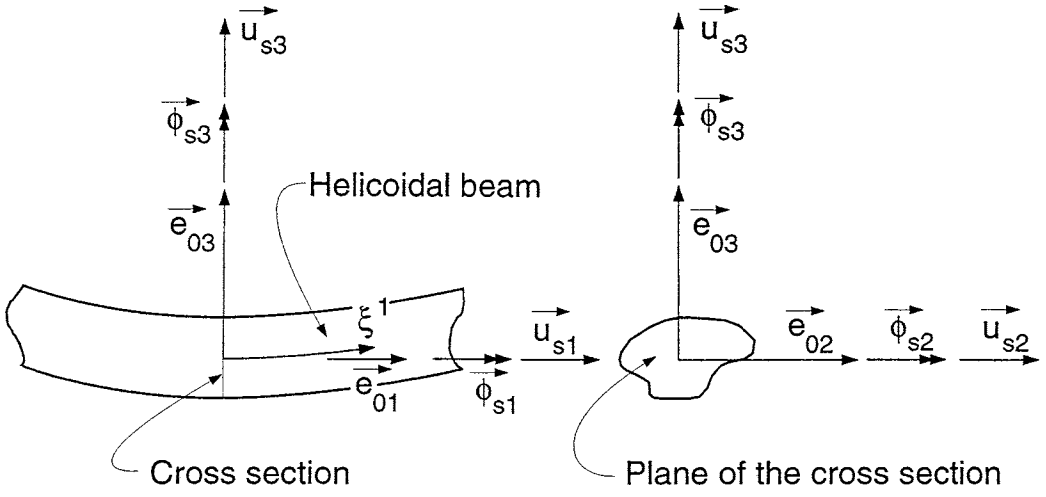

Figure 3.2: Components of the sectional displacement and rotation vectors

3.3.2 Rigid body motion of the beam

To establish some fundamental properties of the M, C and E matrices, consider a rigid body displacement and *small* rotation of the beam as a whole, i.e. in such a manner that no part of the beam is stressed in any way. In this case $\underline{p}^{[0]} = 0$ and $\underline{P} = \underline{P}' = 0$. Let $\underline{u}_s^{[0]}(\xi^1)$ and $\underline{\phi}_s^{[0]}(\xi^1)$ describe the displacement and small rotation of the section at ξ^1 (see figure 3.2). Due to the rigid body nature of the displacement and rotation,

$$\underline{u}^{[0]}(\xi^1, \xi^2, \xi^3) = \underline{u}_s^{[0]}(\xi^1) - \tilde{b}^{[0]}\underline{\phi}_s^{[0]}(\xi^1) \,, \tag{3.21}$$

where $\underline{b}^{[0]} = \lfloor\ 0 \quad \xi^2 \quad \xi^3\ \rfloor^T$ are the components of $\vec{b}$ (see figure 3.1). Eq. (3.21) may now be applied to each node in the mesh, resulting in

$$\underline{U} = Z\underline{X}^{[0]} \,, \tag{3.22}$$

where $\underline{X}^{[0]T} = \lfloor\ \underline{u}_s^{[0]T} \quad \underline{\phi}_s^{[0]T}\ \rfloor$, $Z^T = [\ Z_1^T \quad Z_2^T \quad \cdots \quad Z_n^T\ ]$, and $Z_i = [\ I_3 \quad -\tilde{b}_i^{[0]}\ ]$, $i = 1 \ldots n$, I_3 indicating an identity matrix of order 3.

Also, due to the rigid body nature of the displacement and rotation, $\underline{u}_s^{[0]\prime} =$

$-\tilde{c}^{[0]}\underline{u}_s^{[0]} - \tilde{t}^{[0]}\underline{\phi}_s^{[0]}$ and $\underline{\phi}_s^{[0]\prime} = -\tilde{c}^{[0]}\underline{\phi}_s^{[0]}$, implying that for the rigid body motion,

$$\underline{X}^{[0]\prime} = \mathcal{T}^T \underline{X}^{[0]} , \tag{3.23}$$

Since it is assumed that the beam properties are uniform in the spanwise direction, Z is invariable with respect to ξ^1. Differentiating eq. (3.22) with respect to ξ^1 and using eq. (3.23) leads to:

$$\underline{U}' = Z\mathcal{T}^T \underline{X}^{[0]} . \tag{3.24}$$

Substituting this and eq. (3.22) in eqs. (3.19) and (3.20), with $\underline{P} = \underline{P}' = 0$ for the rigid body motion, the following two identities or fundamental properties of the matrices M, C and E are established:

$$CZT^T + EZ \equiv 0 \tag{3.25}$$

$$MZT^T + C^T Z \equiv 0 . \tag{3.26}$$

3.3.3 Sectional displacement

The Euler-Bernoulli Beam theory, as generalized to the Timoshenko Beam Theory, is based on two assumptions: (1) that the cross section does not deform in its own plane during deformation of the beam, and (2) that the cross section remains plane after deformation. These two assumptions determines an assumed sectional displacement field and can be expressed mathematically, using the notation employed for the helicoidal beam thus far, as:

$$\underline{u}^{[0]}(\xi^1, \xi^2, \xi^3) = \underline{u}_s^{[0]}(\xi^1) - \tilde{b}^{[0]}\underline{\phi}_s^{[0]}(\xi^1) , \tag{3.27}$$

i.e. exactly the same equation as eq. (3.21), only used here in a slightly different context. Whereas the classical Saint-Venant beam theory retains only the first of the Bernoulli assumptions, supplementing the axial displacement field expressed by

eq. (3.27) with an out-of-plane warping, the three dimensional Saint-Venant theory does not make any limiting assumption on the sectional displacement field apart from those pertaining to small strains. Yet it is still very convenient to have a sectional displacement field that has some correspondence with the Bernoulli field. This is achieved by considering the sectional displacement to be comprised of a "Bernoulli" part, which does not strain the section, expressed by the right hand side of eq. (3.27), and a general, three dimensional warping (i.e. out-of-plane warping, like the classical Saint-Venant case, but also in plane warping), to account for all cross sectional distortion:

$$\underline{u}^{[0]}(\xi^1,\xi^2,\xi^3) = \underline{u}_s^{[0]}(\xi^1) - \tilde{b}^{[0]}\underline{\phi}_s^{[0]}(\xi^1) + \underline{w}^{[0]}(\xi^1,\xi^2,\xi^3)\,. \tag{3.28}$$

In the beginning of chapter 2.2, reference is made to "the plane of the cross section in the deformed configuration". Whereas this idea follows naturally from the Bernoulli beam theory, it may not be so clear how it should be interpreted in the case of the three dimensional Saint-Venant beam theory, since no assumption is made about planar sections before deformation remaining plane during deformation. In this case, eq. (3.28) allows the idea of the plane of the section in the deformed configuration to become much clearer: it can most easily be defined as the plane of the cross section in the undeformed configuration, subjected to only the Bernoulli part of the displacement field given in this equation.

The Bernoulli part are determined by three sectional displacement and three sectional rotation components, all six of which are independent of each other. The displacement field given by the above equation is therefore six times indeterminate, as each of the independent Bernoulli components can just as well be expressed in terms of the warping function, $\underline{w}$. Six constraints are therefore required on the warping function in eq. (3.28) to make this displacement field fully determinate.

Using eq. (3.28), the term describing the virtual work done by the external

stresses, in the principle of virtual work eq. (3.14), can now be written as:

$$\begin{aligned} d\xi^1 \int_A \left(\delta \underline{u}^{[0]T} \underline{p}^{[0]}\right)' dA &= d\xi^1 \int_A \left\{\left(\delta \underline{u}_s^{[0]T} + \delta \underline{\phi}_s^{[0]T} \tilde{b}^{[0]}\right) \underline{p}^{[0]}\right\}' dA \\ &\quad + d\xi^1 \int_A \left(\delta \underline{w}^{[0]T} \underline{p}^{[0]}\right)' dA \\ &= \left[\left[\begin{array}{cc} \delta \underline{u}_s^{[0]T} & \delta \underline{\phi}_s^{[0]T} \end{array}\right] \underline{f}^{[0]\prime} + \left[\begin{array}{cc} \delta \underline{u}_s^{[0]T\prime} & \delta \underline{\phi}_s^{[0]T\prime} \end{array}\right] \underline{f}^{[0]} \right. \\ &\quad \left. + \int_A \left(\delta \underline{w}^{[0]T} \underline{p}^{[0]}\right)' dA \right] d\xi^1 , \end{aligned} \tag{3.29}$$

where the following relationship between the stress resultant components $\underline{f}^{[0]}$ and the stress components $\underline{p}^{[0]}$ has been used:

$$\underline{f}^{[0]} = \int_A \begin{bmatrix} I_3 \\ \tilde{b} \end{bmatrix} \underline{p}^{[0]} dA \, .$$

With the aid of eq. (3.4), eq. (3.29) may be further simplified to:

$$\begin{aligned} \int_A \left(\delta \underline{u}^{[0]T} \underline{p}^{[0]}\right)' dA &= \underline{f}^{[0]T} \delta \left| \begin{array}{c} \underline{u}_s^{[0]\prime} + \tilde{c}^{[0]} \underline{u}_s^{[0]} + \tilde{t}^{[0]} \underline{\phi}_s^{[0]} \\ \underline{\phi}_s^{[0]\prime} + \tilde{c}^{[0]} \underline{\phi}_s^{[0]} \end{array} \right| + \int_A \left(\delta \underline{w}^{[0]T} \underline{p}^{[0]}\right)' dA \\ &= \underline{f}^{[0]T} \delta \left(\underline{X}^{[0]\prime} - \mathcal{T}^T \underline{X}^{[0]}\right) + \left(\int_A \delta \underline{w}^{[0]T} \underline{p}^{[0]} \, dA\right)' . \end{aligned}$$

The principle of virtual work may therefore be written as:

$$\int_A \delta \underline{\epsilon}^{[0]T} D^{[0]} \underline{\epsilon}^{[0]} \sqrt{g} \, dA = \underline{f}^{[0]T} \delta \left(\underline{X}^{[0]\prime} - \mathcal{T}^T \underline{X}^{[0]}\right) + \left(\int_A \delta \underline{w}^{[0]T} \underline{p}^{[0]} \, dA\right)' . \tag{3.30}$$

Borri et al. [4, 5] suggest that in order to make the displacement given by eq. (3.28) fully determinate, it is appropriate to define the warping $\underline{w}^{[0]}(\xi^1, \xi^2, \xi^3)$ in such a way that the following orthogonality condition is met:

$$\int_A \underline{w}^{[0]T} \underline{p}^{[0]} \, dA = 0 \, ; \tag{3.31}$$

warping satisfying this condition being referred to as intrinsic warping. In doing so, an intrinsic cross sectional strain measure definition follows from eq. (3.30) as

$$\underline{\varepsilon}^{[0]}(\xi^1) = \underline{X}^{[0]\prime}(\xi^1) - \mathcal{T}^T \underline{X}^{[0]}(\xi^1) \, . \tag{3.32}$$

The implication of using the intrinsic warping and intrinsic sectional strain is that the principle of virtual work, eq. (3.30), can be expressed as:

$$\int_A \delta\underline{\epsilon}^{[0]T} D^{[0]} \underline{\epsilon}^{[0]} \sqrt{g}\, dA = \delta\underline{\varepsilon}^{[0]T} \underline{f}^{[0]} \,. \tag{3.33}$$

Being able to write the principle of virtual work in this form lies at the very heart of claiming that this actually represents a beam theory, since eq. (3.33) basically says that the virtual work per unit span done by the three dimensional internal stresses during a virtual displacement of the beam equals the virtual work per unit span done by the one dimensional stress resultants — the "external loading" of the cross section.

3.3.4 Calculation of cross sectional properties

One may view eq. (3.22) as the discretized equivalent of eq. (3.21). If the warping function $\underline{w}^{[0]}$ is discretized with the same interpolation functions as was used in eq. (3.15), i.e.

$$\underline{w}^{[0]}(\xi^1, \xi^2, \xi^3) = N(\xi^2, \xi^3)\underline{W}(\xi^1) \,, \tag{3.34}$$

then the discretized equivalent of eq. (3.28) is given by:

$$\underline{U} = Z\underline{X}^{[0]} + \underline{W} \,. \tag{3.35}$$

Borri et al. [5] propose a method of determining the central solution in which the orthogonality condition (3.31) is not imposed at first; instead six arbitrary independent constraints are applied to remove the six singularities in the system matrix[2], the resulting system of equations are solved and the intrinsic warping is then recovered with a transformation involving the orthogonality condition. With this in mind, the focus is returned to eq. (3.30). The term in this equation, describing the virtual work per unit span done by the three dimensional internal stresses, can once

[2]The system matrix has not yet been defined, but this is addressed below.

again be discretized as in section 3.3.1. Using eqs. (3.18) and (3.34), the discretized form of the principle of virtual work can then be written as:

$$\delta\underline{U}^T(E\underline{U}+C\underline{U}')+\underline{U}^{T'}(C^T\underline{U}+M\underline{U}')=\delta\underline{\varepsilon}^{[0]T}\underline{f}^{[0]}+\delta\underline{W}^T\underline{P}'+\delta\underline{W}^{T'}\underline{P}\,.$$

In this equation, $\underline{U}$ can be replaced by the right hand side of eq. (3.35). The arbitrariness of the virtual displacement implies that $\delta\underline{W}'$, $\delta\underline{W}$ and $\delta\underline{\varepsilon}^{[0]}$ are all arbitrary. Using this information together with eq. (3.32), and invoking identities (3.25) and (3.26), allow the derivation of the following three sets of equations:

$$M\underline{W}'+C^T\underline{W}+MZ\underline{\varepsilon}^{[0]}=\underline{P} \tag{3.36}$$

$$C\underline{W}'+E\underline{W}+CZ\underline{\varepsilon}^{[0]}=\underline{P}' \tag{3.37}$$

$$Z^TM\underline{W}'+Z^TC^T\underline{W}+Z^TMZ\underline{\varepsilon}^{[0]}=\underline{f}^{[0]}\,. \tag{3.38}$$

Premultiplying eq. (3.36) with Z^T and comparing the result with eq. (3.38) confirms that $\underline{f}^{[0]}=Z^T\underline{P}$, as expected.

Differentiating eq. (3.36) with respect to ξ^1, using the resulting equation to eliminate $\underline{P}'$ from eq. (3.37) and combining this with eq. (3.38) leads to:

$$\bar{M}\underline{Y}''-\bar{H}\underline{Y}'-\bar{E}\underline{Y}=\underline{Q}\,, \tag{3.39}$$

where $\underline{Y}^T=\left\lfloor\ \underline{W}^T\ \ \underline{\varepsilon}^{[0]T}\ \right\rfloor$, $\underline{Q}^T=\left\lfloor\ \underline{0}^T\ \ -\underline{f}^{[0]T}\ \right\rfloor$, and

$$\bar{M}=\begin{bmatrix} M & 0\\ 0 & 0\end{bmatrix}$$

$$\bar{H}=\begin{bmatrix} C-C^T & -MZ\\ Z^TM & 0\end{bmatrix}$$

$$\bar{E}=\begin{bmatrix} E & CZ\\ Z^TC^T & Z^TMZ\end{bmatrix}\,.$$

In the above the order of the various zero matrices should be clear from the context in which they appear.

The particular solution $\underline{Y}(\xi^1)$ of the differential eq. (3.39) can be determined for a known excitation; the form of $\underline{f}^{[0]}(\xi^1)$ given by eq. (3.6) suggest a solution of the form:

$$\underline{Y}(\xi^1) = \underline{Y}_0 + \underline{Y}_{0v} c\xi^1 + (\underline{Y}_c + \underline{Y}_{cv} c\xi^1)\cos(c\xi^1) + (\underline{Y}_s + \underline{Y}_{sv} c\xi^1)\sin(c\xi^1)\,. \quad (3.40)$$

Substituting this into eq. (3.39) leads to four sets of algebraic equations, two of which are complex[3], from which, in the sequence given, the unknown coefficient vectors in the solution (3.40) can be determined:

$$\bar{E}\underline{Y}_{0v} = -\underline{\beta}_0 \quad (3.41)$$

$$\bar{E}\underline{Y}_0 = -\underline{\alpha}_0 - c\bar{H}\underline{Y}_{0v} \quad (3.42)$$

$$\left(c^2\bar{M} - ic\bar{H} + \bar{E}\right)(\underline{Y}_{cv} + i\underline{Y}_{sv}) = -\underline{\beta} \quad (3.43)$$

$$\left(c^2\bar{M} - ic\bar{H} + \bar{E}\right)(\underline{Y}_c + i\underline{Y}_s) = -\underline{\alpha} + c\left(\bar{H}^T - 2ic\bar{M}\right)(\underline{Y}_{cv} + i\underline{Y}_{sv})\,, \quad (3.44)$$

where $i = \sqrt{-1}$ and

$$\underline{\alpha}_0^T = \left\lfloor\ \underline{0}^T \quad -\underline{A}_0^T\ \right\rfloor\ ;\ \underline{\alpha}_c^T = \left\lfloor\ \underline{0}^T \quad -\underline{A}_c^T\ \right\rfloor\ ;\ \underline{\alpha}_s^T = \left\lfloor\ \underline{0}^T \quad -\underline{A}_s^T\ \right\rfloor\ ;$$

$$\underline{\beta}_0^T = \left\lfloor\ \underline{0}^T \quad -\underline{B}_0^T\ \right\rfloor\ ;\ \underline{\beta}_c^T = \left\lfloor\ \underline{0}^T \quad -\underline{B}_c^T\ \right\rfloor\ ;\ \underline{\beta}_s^T = \left\lfloor\ \underline{0}^T \quad -\underline{B}_s^T\ \right\rfloor\ ;$$

$$\underline{\alpha} = \underline{\alpha}_c + i\underline{\alpha}_s\ ;\ \underline{\beta} = \underline{\beta}_c + i\underline{\beta}_s\,.$$

The solution procedure described above allows for the solution of $\underline{Y}^T(\xi^1) = \left\lfloor\ \underline{W}^T(\xi^1) \quad \underline{\varepsilon}^{[0]T}(\xi^1)\ \right\rfloor$ in terms of the stress resultant at the origin $\underline{f}^{[0]}(0)$. In particular, the warping $\underline{W}(0)$, its spanwise derivative $\underline{W}'(0)$ and the sectional strain $\underline{\varepsilon}^{[0]}(0)$ at the origin can be determined. Also, using eq. (3.36), $\underline{P}(0)$ can be determined. By chosing a unit value for one component of $\underline{f}^{[0]}(0)$, with all other components being

[3]The complex form is introduced merely to aid in the numerical solution: in doing so the favorable bandwidth of matrices $\bar{M}$, $\bar{H}$ and $\bar{E}$ are retained.

zero, solving eq. (3.39) and cycling through the process until the solution is obtained for all six components of $\underline{f}^{[0]}(0)$, the following linear relationships are established:

$$\underline{W}(0) = \mathcal{W}(0)\underline{f}^{[0]}(0) \,, \tag{3.45}$$

$$\underline{\varepsilon}^{[0]}(0) = S^{[0]}(0)\underline{f}^{[0]}(0) \tag{3.46}$$

and

$$\underline{P}(0) = \Pi(0)\underline{f}^{[0]}(0) \,, \tag{3.47}$$

where $\mathcal{W}(0)$, $S^{[0]}(0)$ and $\Pi(0)$ are linear operator matrices.

Realizing that the choice of the origin of the ξ^1 axis along the reference line is arbitrary, it is clear that $\mathcal{W}(0)$, $S^{[0]}(0)$ and $\Pi(0)$ are characteristic properties of the cross section, expressed in the sectional axis system, which, due to the assumption of spanwise homogeneity, does not change with ξ^1. This means that eqs. (3.45) to (3.47) are equally valid at any value of ξ^1 other than zero, i.e.

$$\underline{W}(\xi^1) = \mathcal{W}\underline{f}^{[0]}(\xi^1) \,, \tag{3.48}$$

$$\underline{\varepsilon}^{[0]}(\xi^1) = S^{[0]}\underline{f}^{[0]}(\xi^1) \tag{3.49}$$

and

$$\underline{P}(\xi^1) = \Pi\underline{f}^{[0]}(\xi^1) \,. \tag{3.50}$$

The matrix $S^{[0]}$ is identified as the cross sectional compliance tensor. The i-th column of $\mathcal{W}$ is the discretized warping of the section due to a stress resultant vector such that all components are zero, except the i-th, which has a unit value. Since this is a characteristic function of the cross section, $\mathcal{W}$ is the characteristic warping matrix of the section. Furthermore, since $\underline{f}^{[0]} = Z^T\underline{P}$,

$$Z^T\Pi \equiv I \,. \tag{3.51}$$

Due to the fact that eq. (3.28) is six times indeterminate, both matrices E and $\bar{E}$ are six times singular. As mentioned before, six arbitrary independent constraints

are applied[4] to remove these singularities from E and the system matrix, $\bar{E}$. This is necessary in order to be able to solve eqs. (3.41) and (3.42). All of the above relationships holds for the solution obtained in this way; the only problem is that since the orthogonality condition, eq. (3.31), is not necessarily met, the warping and sectional strain obtained in this manner are not necessarily the intrinsic warping and intrinsic sectional strain. These can, however, be recovered easily by the following procedure suggested by Borri et al. [5].

To distinguish this solution from the intrinsic solution, all quantities pertaining to the solution obtained with the arbitrary constraints are indicated with an overbar. The discretized form of the orthogonality condition is written as

$$\underline{P}^T \underline{W} \equiv 0 \,, \tag{3.52}$$

which implies

$$\Pi^T \mathcal{W} \equiv 0 \,. \tag{3.53}$$

The nodal displacement vector $\underline{U}$ is the same for the two solutions, thus:

$$\underline{U} = Z\underline{\bar{X}}^{[0]} + \underline{\bar{W}} = Z\underline{X}^{[0]} + \underline{W} \,.$$

Therefore,

$$\underline{\bar{W}} - \underline{W} = Z(\underline{X}^{[0]} - \underline{\bar{X}}^{[0]}) \,, \tag{3.54}$$

from which it is evident that the intrinsic warping and the warping corresponding to the use of six arbitrary constraints differ by a rigid displacement of the cross section. On the other hand, the two warpings are caused by the same loading condition, therefore

$$\underline{\bar{W}} - \underline{W} = (\bar{\mathcal{W}} - \mathcal{W})\underline{f}^{[0]} \,. \tag{3.55}$$

If it is now assumed that a constant operator $\mathcal{Q}$ exists such that

$$\underline{\bar{W}} - \underline{W} = Z\mathcal{Q}\underline{f}^{[0]} \,, \tag{3.56}$$

[4]In practice this is done most easily by assigning an extremely high value to the diagonal term in E corresponding to each degree of freedom constrained.

then

$$\bar{\mathcal{W}} - \mathcal{W} = Z\mathcal{Q}\,, \tag{3.57}$$

and, from eqs. (3.54) and (3.56)

$$\underline{X}^{[0]} - \bar{\underline{X}}^{[0]} = \mathcal{Q}\underline{f}^{[0]}\,. \tag{3.58}$$

Premultiplying eq. (3.57) with Π^T and invoking eqs. (3.51) and (3.53) allows $\mathcal{Q}$ to be determined:

$$\mathcal{Q} = \Pi^T\bar{\mathcal{W}}\,.$$

The intrinsic characteristic warping matrix is then determined using eq. (3.57):

$$\mathcal{W} = [I - Z\Pi^T]\bar{\mathcal{W}}\,.$$

The intrinsic sectional strain can be obtained from

$$\begin{aligned}\underline{\varepsilon}^{[0]} - \bar{\underline{\varepsilon}}^{[0]} &= \underline{X}^{[0]\prime} - \bar{\underline{X}}^{[0]\prime} - \mathcal{T}^T[\underline{X}^{[0]} - \bar{\underline{X}}^{[0]}] \\ &= \mathcal{Q}\underline{f}^{[0]\prime} - \mathcal{T}^T\mathcal{Q}\underline{f}^{[0]}\,,\end{aligned}$$

where eq. (3.58) was used. With the aid of eq. (3.4), the "intrinsic" sectional compliance tensor can then be calculated as:

$$S^{[0]} = \bar{S}^{[0]} - \mathcal{Q}\mathcal{T} - \mathcal{T}^T\mathcal{Q}\,.$$

The cross sectional stiffness tensor is obtained by inverting the cross sectional compliance tensor[5]: $C^{[0]} = S^{[0]^{-1}}$. The sectional stiffness relationship, i.e. the inverse of eq. (3.49) can therefore be written as:

$$\underline{f}^{[0]}(\xi^1) = C^{[0]}\underline{\varepsilon}^{[0]}(\xi^1)\,. \tag{3.59}$$

[5]No reference is made in this thesis to the sectional stiffness tensor expressed in the $\mathcal{S}$ system. The $*$ or [0] superscripts used everywhere should help to distinguish the 6×6 stiffness tensor from C, the $3n \times 3n$ matrix defined in eq. (3.18).

3.4 Stress and strain recovery

In order to calculate the three dimensional stress or strain at any point in the cross section, due to a given stress resultant, eq. (3.35) may be substituted into eq. (3.16). Using the definition of the sectional strain, eq. (3.32), the three dimensional strain may be expressed as:

$$\underline{\epsilon}^{[0]} = \bar{A}[Z\underline{\varepsilon}^{[0]} + \underline{W}'] + B\underline{W} + [\bar{A}ZT^T + BZ]\underline{X}^{[0]} \,. \tag{3.60}$$

Using the same kind of argument employed in section 3.3.2, consider once again a rigid body motion of the beam as a whole, without straining the beam in any way. Under such circumstances, $\underline{\epsilon}^{[0]} = \underline{\varepsilon}^{[0]} = \underline{W}' = \underline{W} = 0$, while $\underline{X}^{[0]}$ takes on any arbitrary value, depending on the displacement of the beam. With these values, eq. (3.60) establishes another useful identity:

$$[\bar{A}ZT^T + BZ]\underline{X}^{[0]} \equiv 0 \,. \tag{3.61}$$

That this identity also holds for the case when the beam is strained follows from the arbitrariness of $\underline{X}^{[0]}$ and the fact that $[\bar{A}ZT^T + BZ]$ is independent of the loading of and the strain in the beam.

Using this identity, eqs. (3.48) and (3.49), and the fact that differentiating eq. (3.48) together with eq. (3.4) implies

$$\underline{W}' = \mathcal{W}\underline{f}^{[0]\prime} = -\mathcal{W}\mathcal{T}\underline{f}^{[0]} \,, \tag{3.62}$$

eq. (3.60) can be written as

$$\underline{\epsilon}^{[0]} = \begin{bmatrix} \bar{A} & B \end{bmatrix} \begin{bmatrix} ZS^{[0]} - \mathcal{W}\mathcal{T} \\ \mathcal{W} \end{bmatrix} \underline{f}^{[0]} \,. \tag{3.63}$$

The three dimensional stress $\underline{\sigma}^{[0]}$ is obtained by using the material stiffness relationship:

$$\underline{\sigma}^{[0]} = D^{[0]}\underline{\epsilon}^{[0]} \,. \tag{3.64}$$

3.5 Strain energy expression

The strain energy of the beam is given by

$$V = \frac{1}{2}\int_0^L \int_A \underline{\epsilon}^{[0]T} D^{[0]} \underline{\epsilon}^{[0]} \sqrt{g}\, dA\, d\xi^1 \ . \tag{3.65}$$

Substituting eq. (3.63) into the above equation and using the sectional integral definitions, eq. (3.18), leads to

$$\begin{aligned} V \ = \ & \frac{1}{2}\int_0^L \underline{f}^{[0]T} \Big[S^{[0]} Z^T M Z S^{[0]} + \mathcal{W}^T C Z S^{[0]} - \mathcal{T}^T \mathcal{W}^T M Z S^{[0]} \\ & + S^{[0]} Z^T C^T \mathcal{W} + \mathcal{W}^T E \mathcal{W} - \mathcal{T}^T \mathcal{W}^T C^T \mathcal{W} \\ & - S^{[0]} Z^T M \mathcal{W} \mathcal{T} - \mathcal{W}^T C \mathcal{W} \mathcal{T} + \mathcal{T}^T \mathcal{W}^T M \mathcal{W} \mathcal{T} \Big] \underline{f}^{[0]} d\xi^1 \ . \end{aligned} \tag{3.66}$$

Substituting eq. (3.48) into the discretized form of the orthogonality condition, eq. (3.52), and realizing that this holds for arbitrary values of $\underline{f}^{[0]}$, leads to $\underline{P}^T \mathcal{W} \equiv 0$. Differentiating eq. (3.52) with respect to ξ^1 results in:

$$\underline{P}^{T\prime} \underline{W} + \underline{P}^T \underline{W}' \equiv 0 \ .$$

Using eq. (3.62), this can be written as

$$\underline{P}^{T\prime} \underline{W} - \underline{P}^T \mathcal{W} \mathcal{T} \underline{f}^{[0]} = \underline{P}^{T\prime} \underline{W} \equiv 0 \ .$$

Substituting eqs. (3.37), (3.48), (3.49) and (3.62) into the above equation results in

$$- \mathcal{W}^T C \mathcal{W} \mathcal{T} + \mathcal{W}^T E \mathcal{W} + \mathcal{W}^T C Z S^{[0]} \equiv 0 \ . \tag{3.67}$$

Substituting eqs. (3.36), (3.48), (3.49) and (3.62) into eq. (3.52) results in

$$- \mathcal{W}^T M \mathcal{W} \mathcal{T} + \mathcal{W}^T C^T \mathcal{W} + \mathcal{W}^T M Z S^{[0]} \equiv 0 \ . \tag{3.68}$$

Substituting eqs. (3.48), (3.49) and (3.62) into eq. (3.36) and comparing the result with equation(3.50) leads to:

$$\Pi = -M \mathcal{W} \mathcal{T} + C^T \mathcal{W} + M Z S^{[0]} \ .$$

Premultiplying this equation with $S^{[0]}Z^T$ and invoking the identity, equation(3.51) results in:

$$-S^{[0]}Z^TMW\mathcal{T}+S^{[0]}Z^TC^T\mathcal{W}+S^{[0]}Z^TMZS^{[0]}=S^{[0]}\,. \tag{3.69}$$

Substituting eqs. (3.67) to (3.69) into eq. (3.66) therefore results in:

$$V=\frac{1}{2}\int_0^L \underline{f}^{[0]T}S^{[0]}\underline{f}^{[0]}d\xi^1\,,$$

while using eq. (3.59) allows this equation to be written as:

$$V=\frac{1}{2}\int_0^L \underline{\varepsilon}^{[0]T}C^{[0]}\underline{\varepsilon}^{[0]}d\xi^1\,. \tag{3.70}$$

Only little attention has been given until now to the fact that the strain energy expression which is pursued in this chapter, eq. (3.1), expresses components in the $\mathcal{S}^*$ system, whereas all components considered until now are given in $\mathcal{S}_0$. It is important to note that in deriving the sectional stiffness tensor, a small rotation assumption is implied by eq. (3.28). Since both $\underline{\varepsilon}^{[0]}$ and $C^{[0]}$ are independent of the actual sectional displacement $\underline{X}^{[0]}$, one could arbitrarily drive down the rotation during deformation (by reducing the applied loading) to the point that $\underline{\varepsilon}^{[0]}=\underline{\varepsilon}^*$ and $C^{[0]}=C^*$. This means that with $\underline{X}^{[0]}$ sufficiently small, eq. (3.70) is the same as eq. (3.1).

The important question, however, is how all of this should be interpreted when eq. (3.1) is applied to a case involving large rotation during deformation, as suggested in the introduction to this chapter. To answer this, one needs to realize that in the above derivation, the sectional stiffness tensor is expressed in the local sectional axes system, which in a large rotation case corresponds to $\mathcal{S}^*$. This means that even in the large rotation case, $C^{[0]}$ in eq. (3.70) should be interpreted to be equivalent to C^* in eq. (3.1), without any transformation.

Another way of looking at this issue is to simply say that, in the derivation of the three dimensional Saint-Venant beam theory, the rotation during deformation

is so small, that the rotation matrix between $\mathcal{S}_0$ and $\mathcal{S}^*$ is an identity matrix. In that case, eqs. 3.2 and 3.3, which are normally valid only with respect to the beam in the undeformed configuration, become also valid for the beam in the deformed configuration. The whole derivation can then be repeated in terms of components in the $\mathcal{S}^*$ system, to directly give eq. (3.1).

3.6 Conclusion

In conclusion, a strain energy expression

$$V = \frac{1}{2} \int_0^L \underline{\varepsilon}^{*T} C^* \underline{\varepsilon}^* \, d\xi^1 \tag{3.71}$$

has been established, for naturally curved and twisted beams, made of anisotropic materials. This expression has been shown to be closely related to a linear sectional constitutive law $\underline{f}^* = C^* \underline{\varepsilon}^*$. It has been shown how the sectional stiffness tensor C^* is calculated, and that, with the spanwise distribution of either $\underline{f}^*$ or $\underline{\varepsilon}^*$ known, the full three dimensional state of stress at any point in the beam can be calculated.

CHAPTER 4
ADVANCED BEAM THEORY

4.1 Introduction

In this chapter two extensions to the three dimensional Saint-Venant beam theory, derived in chapter 3, are presented, both of which are of prime importance in the modeling of helicopter rotor blades. The first deals with differential warping. A modal method is presented to model this effect. The second extension deals with the non-linear effect of increase in especially the torsional and shear stiffness of the section when the beam is subjected to high axial loading (which is common in helicopter rotors due to centrifugal loading). Since this effect has to do with higher order sectional strain terms, it will be referred to in the rest of this thesis as the "non-linear strain effect". In the derivation of the kinetic energy expression of the advanced beam theory, it will be pointed out how this derivation may be modified to render the sectional inertia tensor as an alternative result.

4.2 Analysis of beams subjected to differential warping

In the beginning of chapter 3, one of the assumptions made with respect to the central solution is the absence of any physical constraint on the warping. When this condition is not met, a state of differential warping is said to exist, because the warping then needs to change in the spanwise direction in a way different from that prescribed by eq. (3.48). The three dimensional Saint-Venant theory is the exact solution of the linear elasticity beam problem in the absence of differential warping. In this section a first extension to this theory is investigated: a modal method which allows analysis in the presence of differential warping.

To obtain the central solution, it was convenient to split up the sectional

displacement field into a "Bernoulli part" and a warping (see eqs. (3.28) and (3.35)). This warping function was fully determined by the applied stress resultant loading $\underline{f}^{[0]}$, as indicated in eq. (3.48). To study differential warping, it is necessary to allow the warping to change in the spanwise direction under influencing factors other than only $\underline{f}^{[0]}$. To this end, one may decompose the warping function in eq. (3.35) into m warping modes, each multiplying a corresponding modal participation factor $\lambda_i, i = 1...m$. If W is the $(3n \times m)$ modal matrix, of which the i-th column is filled with the i-th warping mode shape, the sectional displacement field can be expressed as:

$$\underline{U} = Z\underline{X}^{[0]} + W\underline{\lambda}\,. \tag{4.1}$$

A logical choice of modal warping functions to be included in the modal basis are the six central solution characteristic intrinsic warping functions. If these are all included, at least the central solution should be recovered from the modal method. The choice is however not limited to the characteristic warping functions. The extremity solution mode shapes, which are also warping functions, may also be used. Even though this possibility was always kept in mind during the development of the computer code based on the advanced beam theory, the use of the extremity solution modes were never numerically investigated.

4.2.1 Strain Energy

Substituting eq. (4.1) into the three dimensional strain field, eq. (3.16), and using the sectional strain definition, eq. (3.32) and identity (3.61), results in:

$$\underline{\epsilon}^{[0]} = \bar{A}Z\underline{\varepsilon}^{[0]} + BW\underline{\lambda} + \bar{A}W\underline{\lambda}'\,.$$

The strain energy of the beam, as given by eq. (3.65), can now be expressed as:

$$V = \frac{1}{2}\int_0^L \int_A [\underline{\varepsilon}^{[0]T} Z^T \bar{A}^T D^{[0]} \bar{A} Z \underline{\varepsilon}^{[0]} + \underline{\varepsilon}^{[0]T} Z^T \bar{A}^T D^{[0]} BW\underline{\lambda} + \underline{\varepsilon}^{[0]T} Z^T \bar{A}^T D^{[0]} \bar{A} W\underline{\lambda}'$$
$$+ \underline{\lambda}^T W^T B^T D^{[0]} \bar{A} Z \underline{\varepsilon}^{[0]} + \underline{\lambda}^T W^T B^T D^{[0]} BW\underline{\lambda} + \underline{\lambda}^T W^T B^T D^{[0]} \bar{A} W\underline{\lambda}'$$

$$+\underline{\lambda}'^T W^T \bar{A}^T D^{[0]} \bar{A} Z \underline{\varepsilon}^{[0]} + \underline{\lambda}'^T W^T \bar{A}^T D^{[0]} B W \underline{\lambda} + \underline{\lambda}'^T W^T \bar{A}^T D^{[0]} \bar{A} W \underline{\lambda}'] \sqrt{g}\, dA\, d\xi^1 \ .$$

Using the sectional integrals, eq. (3.18), the above expression can be simplified to:

$$V = \frac{1}{2} \int_0^L \left| \begin{array}{ccc} \underline{\varepsilon}^{[0]T} & \underline{\lambda}^T & \underline{\lambda}'^T \end{array} \right| \left[\begin{array}{ccc} Z^T M Z & Z^T C^T W & Z^T M W \\ W^T C Z & W^T E W & W^T C W \\ W^T M Z & W^T C^T W & W^T M W \end{array} \right] \left| \begin{array}{c} \underline{\varepsilon}^{[0]} \\ \underline{\lambda} \\ \underline{\lambda}' \end{array} \right| d\xi^1 \ . \quad (4.2)$$

The modal method sectional stiffness matrix $\mathbf{C}$ is now defined as:

$$\mathbf{C} = \left[\begin{array}{ccc} Z^T M Z & Z^T C^T W & Z^T M W \\ W^T C Z & W^T E W & W^T C W \\ W^T M Z & W^T C^T W & W^T M W \end{array} \right] \quad (4.3)$$

and the modal method sectional strain vector $\underline{\boldsymbol{\varepsilon}}$ as

$$\underline{\boldsymbol{\varepsilon}} = \left| \begin{array}{c} \underline{\varepsilon}^* \\ \underline{\lambda} \\ \underline{\lambda}' \end{array} \right| \quad (4.4)$$

allowing to write eq. (4.2) as

$$V = \frac{1}{2} \int_0^L \underline{\boldsymbol{\varepsilon}}^T \mathbf{C} \underline{\boldsymbol{\varepsilon}}\, d\xi^1 \ . \quad (4.5)$$

In the above definition of $\underline{\boldsymbol{\varepsilon}}$, $\underline{\varepsilon}^*$ was introduced instead of $\underline{\varepsilon}^{[0]}$. This was done, once again, because of the fact that the derived stiffness matrix is expressed in the local sectional axis system, which is $\mathcal{S}^*$ in the presence of large rotations, i.e. both $\mathbf{C}$ and $\underline{\boldsymbol{\varepsilon}}$ should be interpreted as being expressed in $\mathcal{S}^*$.

4.2.2 Kinetic Energy

The displacement field of all points on the cross section was discretized using eq. (3.15). Substituting eq. (4.1) into eq. (3.15) results in:

$$\begin{aligned} \underline{u}^{[0]}(\xi^1, \xi^2, \xi^3) &= N Z \underline{X}^{[0]} + N W \underline{\lambda} \\ &= N Z \underline{X}^{[0]} + w \underline{\lambda} \end{aligned}$$

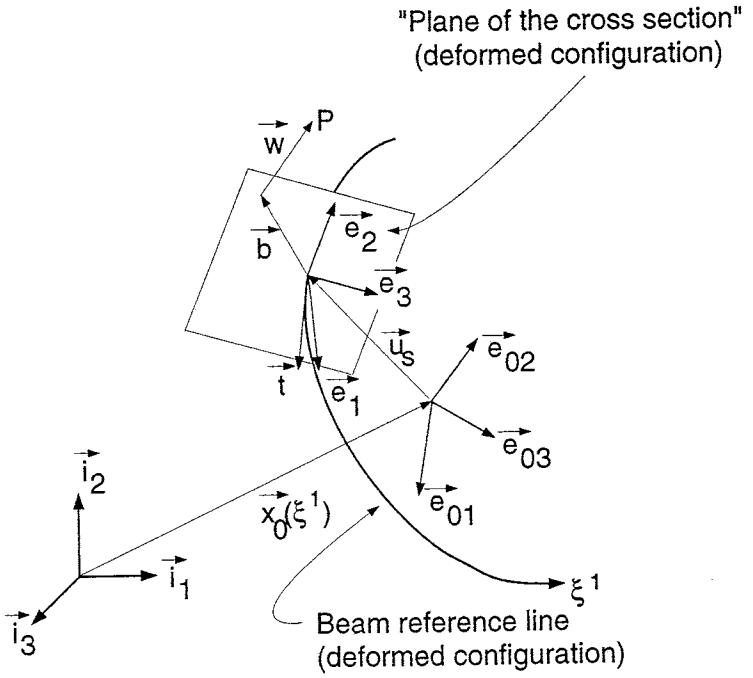

Figure 4.1: Position of generic point P, initially in the plane of the cross section, after deformation

where $w(\xi^2, \xi^3) = NW$ is a $3 \times m$ matrix of functions, the j-th column of which corresponds to the three dimensional warping function across the section associated with the j-th mode, measured in the local sectional axis system (i.e. the columns of W are the discretized representation of the columns of w).

Consider once again a point P in the plane of the cross section (see figure 3.1). After deformation the position vector of P, in the $\mathcal{S}$ system components, is (see figure 4.1):

$$\underline{\mathcal{X}} = \underline{x}_0 + \underline{u}_s + RR_0(\underline{b}^* + \underline{w}^*) \, . \tag{4.6}$$

Since the warping is a purely linear extension to the problem kinematics, it is clear that the modal representation of the warping displacement at point P, $\underline{w}^*$ in eq. (4.6), is exactly $w\underline{\lambda}$. This equation may therefore be written as:

$$\underline{\mathcal{X}} = \underline{x}_0 + \underline{u}_s + RR_0(\underline{b}^* + w\underline{\lambda}) \, .$$

The velocity of point P is then:

$$\begin{aligned}\dot{\underline{\mathcal{X}}} &= \dot{\underline{u}}_s + RR_0 w\dot{\underline{\lambda}} + \dot{R}R^T RR_0(\underline{b}^* + w\underline{\lambda}) \\ &= \dot{\underline{u}}_s + RR_0 w\dot{\underline{\lambda}} + \tilde{\omega}RR_0(\underline{b}^* + w\underline{\lambda}) \\ &= \dot{\underline{u}}_s + RR_0\left[w\dot{\underline{\lambda}} + \underline{\omega}^*(\underline{b}^* + w\underline{\lambda})\right] . \end{aligned} \tag{4.7}$$

The kinetic energy of the beam is given by:

$$K = \frac{1}{2}\int_0^L \int_A \rho\dot{\underline{\mathcal{X}}}^T\dot{\underline{\mathcal{X}}}\sqrt{g}dA\, d\xi^1 . \tag{4.8}$$

Substituting eq. (4.7) into eq. (4.8) and simplifying leads to:

$$\begin{aligned} K &= \frac{1}{2}\int_0^L \Big\{\int_A \rho\sqrt{g}dA\dot{\underline{u}}_s^T\dot{\underline{u}}_s + 2\dot{\underline{u}}_s^T RR_0\left[\int_A \rho w\sqrt{g}dA\dot{\underline{\lambda}}\right. \\ &\quad \left. + \tilde{\omega}^*\left(\int_A \rho\underline{b}^*\sqrt{g}dA + \int_A \rho w\sqrt{g}dA\underline{\lambda}\right)\right] + \dot{\underline{\lambda}}^T\int_A \rho w^T w\sqrt{g}dA\dot{\underline{\lambda}} \\ &\quad + 2\underline{\lambda}^T\left(\int_A \rho w^T\tilde{b}^{*T}\sqrt{g}dA\underline{\omega}^* + \int_A \rho w^T\widetilde{w\underline{\lambda}}^T\sqrt{g}dA\underline{\omega}^*\right) + \underline{\omega}^{*T}\int_A \rho\tilde{b}^*\tilde{b}^{*T}\sqrt{g}dA\underline{\omega}^* \\ &\quad + 2\underline{\omega}^{*T}\int_A \rho\tilde{b}^*\widetilde{w\underline{\lambda}}^T\sqrt{g}dA\underline{\omega}^* + \underline{\omega}^{*T}\int_A \rho\widetilde{w\underline{\lambda}}\widetilde{w\underline{\lambda}}^T\sqrt{g}dA\underline{\omega}^*\Big\}\, d\xi^1 . \end{aligned}$$

The kinetic energy associated with the warping of the cross section is small compared to that associated with the rotation and translation of the cross section. The third order terms involving $\underline{\lambda}$ and $\dot{\underline{\lambda}}$ may therefore be neglected in the above kinetic energy expression, allowing this to be written as:

$$\begin{aligned} K &= \frac{1}{2}\int_0^L \Big\{m\dot{\underline{u}}_s^T\dot{\underline{u}}_s + 2\dot{\underline{u}}_s^T RR_0\chi^T\dot{\underline{\lambda}} + 2\dot{\underline{u}}_s^T RR_0\tilde{m}^{*T}\underline{\omega}^* + \dot{\underline{\lambda}}^T\Psi\dot{\underline{\lambda}} \\ &\quad + 2\dot{\underline{\lambda}}^T\Gamma\underline{\omega}^* + \underline{\omega}^{*T}\bar{I}^*\underline{\omega}^*\Big\}\, d\xi^1 , \end{aligned}$$

where the following sectional mass integrals are defined (keeping in mind that $\underline{b}^{[0]} = \underline{b}^*$): $m = \int_A \rho\sqrt{g}dA$, the mass per unit length of the beam, $\underline{m}^* = \int_A \rho\underline{b}^{[0]}\sqrt{g}dA$, the vector of static offset per unit length, $\bar{I}^* = \int_A \rho\tilde{b}^{[0]}\tilde{b}^{[0]T}\sqrt{g}dA$, the tensor of moment of inertia per unit length, and

$$\chi = \int_A \rho w^T\sqrt{g}dA = W^T\int_A \rho N^T\sqrt{g}dA$$

$$\Gamma = \int_A \rho w^T \tilde{b}^{[0]T} \sqrt{g} dA = W^T \int_A \rho N^T \tilde{b}^{[0]T} \sqrt{g} dA$$
$$\Psi = \int_A \rho w^T w \sqrt{g} dA = W^T \int_A \rho N^T N \sqrt{g} dA W \ .$$

The modal method sectional velocity vector $\underline{\mathbf{v}}$ and inertia matrix $\mathbf{M}$ are defined as:

$$\underline{\mathbf{v}} = \begin{vmatrix} R_0^T R^T \underline{\dot{u}}_s \\ R_0^T R^T \underline{\omega} \\ \underline{\dot{\lambda}} \end{vmatrix}$$

and

$$\mathbf{M} = \begin{bmatrix} m & 0 & 0 & & \\ 0 & m & 0 & \tilde{m}^{*T} & \chi^T \\ 0 & 0 & m & & \\ & \tilde{m}^* & & \bar{I}^* & \Gamma^T \\ & \chi & & \Gamma & \Psi \end{bmatrix},$$

so that the kinetic energy can finally be written as:

$$K = \frac{1}{2} \int_0^L \underline{\mathbf{v}}^T \mathbf{M} \underline{\mathbf{v}} \, d\xi^1 \ . \tag{4.9}$$

It may be fitting to focus attention for a moment on the kinetic energy expression associated with the central solution. Considering eq. (3.28), it can be argued that the kinetic energy associated with any sectional intrinsic warping is negligibly small[1] compared to the kinetic energy associated with the sectional displacement degrees of freedom $\underline{X}^{[0]}$. With this approximation the kinetic energy expressions of the Bernoulli and three dimensional Saint-Venant beam theories are identical, and may be derived in a similar manner as the kinetic energy expression (4.9) above, by simply disregarding all terms associated with warping. The result is the kinetic

[1]This approximation is not made in the case of the advanced beam theory, because it would lead to zero inertia being associated with the warping modal participation factors $\underline{\lambda}$, which can cause problems in the time integration process.

energy expression (2.4), where the sectional inertia tensor M^* is given by:

$$M^* = \begin{bmatrix} m & 0 & 0 & \\ 0 & m & 0 & \tilde{m}^{*T} \\ 0 & 0 & m & \\ & \tilde{m}^* & & \bar{I}^* \end{bmatrix}.$$

It is clear that M^* is contained as a sub-matrix in the modal method sectional inertia matrix $\mathbf{M}$.

Standard finite element discretization of the strain and kinetic energy expressions, eqs. (4.5) and (4.9), can now be used to implement this modal method in an advanced beam element, which can treat differential warping. At each node of this beam element, in addition to the usual six degrees of freedom corresponding to $\underline{X}^{[0]}$, m degrees of freedom exist: the m components of $\underline{\lambda}$. Even though these additional degrees of freedom correspond to modal participation factors, they can be considered as displacement degrees of freedom, and continuity of $\underline{\lambda}$ is therefore enforced across element boundaries, as is done for $\underline{X}^{[0]}$.

4.3 Analysis of beams subjected to the non-linear strain effect

In this section the second extension to the three dimensional Saint-Venant beam theory is investigated: the inclusion in the strain energy expression of non-linear sectional strain terms to account for a non-linear strain effect, which is sometimes called the trapeze effect.

Bauchau et al. [11] derived a non-linear beam theory for composite materials, based on the classical Saint-Venant beam theory. In doing so, fully non-linear equations were derived to express the non-zero components of the three dimensional strain tensor in terms of the sectional strain tensor of the beam. In applying these equations to composite materials, the importance of not neglecting terms quadratic in either one of the three dimensional shear strain components, compared to terms

linear in the axial strain component, was emphasized. The reason for this is that in the case of highly anisotropic composite materials, the shear strain is not necessarily of the same order of magnitude (i.e. as small) as the axial strain. These terms are shown in [11] to appear only in the expression for the axial strain and are expressed in terms of three components of the sectional strain tensor: the two transverse shear strains and the elastic twist rate. An example given by [11], of a thin walled hollow beam with a circular cross section, made of unidirectional composite material, with the fibers aligned with the beam axis, shows that the torsional stiffness of such a beam is highly dependent on the axial strain in the beam, as the beam is put under axial tension. It furthermore shows that the ability of the beam model to predict this torsional stiffening under tension is directly related to the inclusion of these quadratic shear terms in the formulation.

This non-linear effect can be very important in helicopter rotor blades, which nowadays quite often employ large portions of spanwise unidirectional composite fibers and which are subjected to high axial tension, due to centrifugal loading. For this reason it is important to provide the capability to model this effect.

The central solution derived in chapter 3 is a linear theory and in its derivation the small strain assumption is used. A non-linear extension to the three dimensional Saint-Venant beam theory, which applies to the case of straight untwisted beams and which accounts for stiffening of the blade due to pre-stress, was presented by Borri, et al. [4]. A different approach is followed in this work. The expression for the three dimensional strain tensor component corresponding to direct strain in the axial direction is supplemented with the two quadratic shear strain terms indicated by [11], expressed in terms of the two sectional transverse shear strains ε_2 and ε_3, and the sectional elastic twist rate ε_4, ε_i being the i-th component of $\underline{\varepsilon}^{[0]}$. This means that

$$\epsilon_{11}(\xi^1,\xi^2,\xi^3) = \epsilon_{11L}(\xi^1,\xi^2,\xi^3) + [\frac{1}{2}(\varepsilon_2(\xi^1) - b_3\varepsilon_4(\xi^1))^2 + \frac{1}{2}(\varepsilon_3(\xi^1) + b_2\varepsilon_4(\xi^1))^2] \,,$$

where $\epsilon_{11L}(\xi^1,\xi^2,\xi^3)$ indicates the *linear* part of the three dimensional strain in the axial direction, as given by eq. (3.13). The linear three dimensional strain expression (3.63) is therefore supplemented, using also eq. (3.59), as follows:

$$\underline{\epsilon}^{[0]} = [\bar{A}Z + BWC^{[0]} - \bar{A}W\mathcal{T}C^{[0]}]\underline{\varepsilon}^{[0]} + [\frac{1}{2}(\varepsilon_2 - b_3\varepsilon_4)^2 + \frac{1}{2}(\varepsilon_3 + b_2\varepsilon_4)^2]\Phi \ ,$$

where $\Phi^T = \lfloor\ 1 \quad 0 \quad 0 \quad 0 \quad 0 \quad 0\ \rfloor$. The strain energy of the beam, as given by eq. (3.65), can now be expressed as:

$$\begin{aligned} V \ = \ & \frac{1}{2}\int_0^L \int_A \underline{\varepsilon}^{[0]T}(Z^T\bar{A}^T D^{[0]}\bar{A}Z + Z^T\bar{A}^T D^{[0]}BWC^{[0]} - Z^T\bar{A}^T D^{[0]}\bar{A}W\mathcal{T}C^{[0]} \\ & + C^{[0]}W^T B^T D^{[0]}\bar{A}Z + C^{[0]}W^T B^T D^{[0]}BWC^{[0]} - C^{[0]}W^T B^T D^{[0]}\bar{A}W\mathcal{T}C^{[0]} \\ & - C^{[0]}\mathcal{T}^T W^T\bar{A}^T D^{[0]}\bar{A}Z - C^{[0]}\mathcal{T}^T W^T\bar{A}^T D^{[0]}BWC^{[0]} \\ & + C^{[0]}\mathcal{T}^T W^T\bar{A}^T D^{[0]}\bar{A}W\mathcal{T}C^{[0]})\underline{\varepsilon}^{[0]}\sqrt{g}\,dA\,d\xi^1 \\ & + \int_0^L \int_A \underline{\varepsilon}^{[0]T}(Z^T\bar{A}^T D^{[0]}\Phi + C^{[0]}W^T B^T D^{[0]}\Phi - C^{[0]}\mathcal{T}^T W^T\bar{A}^T D^{[0]}\Phi)\cdot \\ & \left\{\frac{1}{2}(\varepsilon_2 - b_3\varepsilon_4)^2 + \frac{1}{2}(\varepsilon_3 + b_2\varepsilon_4)^2\right\}\sqrt{g}\,dA\,d\xi^1 \ , \end{aligned} \tag{4.10}$$

where fourth order terms in ε_i where neglected.

Eight additional sectional integrals, all $(3n \times 1)$ column vectors, are now defined:

$$\begin{aligned} \underline{\alpha}_0 &= \int_A \bar{A}^T D^{[0]}\Phi\sqrt{g}\,dA & \underline{\beta}_0 &= \int_A B^T D^{[0]}\Phi\sqrt{g}\,dA \\ \underline{\alpha}_2 &= \int_A \bar{A}^T D^{[0]}\Phi b_2\sqrt{g}\,dA & \underline{\beta}_2 &= \int_A B^T D^{[0]}\Phi b_2\sqrt{g}\,dA \\ \underline{\alpha}_3 &= \int_A \bar{A}^T D^{[0]}\Phi b_3\sqrt{g}\,dA & \underline{\beta}_3 &= \int_A B^T D^{[0]}\Phi b_3\sqrt{g}\,dA \\ \underline{I}_\alpha &= \int_A \bar{A}^T D^{[0]}\Phi(b_2^2 + b_3^2)\sqrt{g}\,dA & \underline{I}_\beta &= \int_A B^T D^{[0]}\Phi(b_2^2 + b_3^2)\sqrt{g}\,dA \ . \end{aligned} \tag{4.11}$$

The first integral term in eq. (4.10) reduces to $\frac{1}{2}\int_0^L \underline{\varepsilon}^{[0]T}C^{[0]}\underline{\varepsilon}^{[0]}\,d\xi^1$, exactly as in section 3.5. Substituting the sectional integrals, eq. (4.11) into the second integral term in eq. (4.10) leads to:

$$V \ = \ \frac{1}{2}\int_0^L \underline{\varepsilon}^{[0]T}C^{[0]}\underline{\varepsilon}^{[0]}\,d\xi^1$$

$$+\int_0^L \underline{\varepsilon}^{[0]T}\left[(Z^T - C^{[0]}\mathcal{T}^T\mathcal{W}^T)\left(\underline{\alpha}_0\frac{\varepsilon_2^2+\varepsilon_3^2}{2} + \underline{\alpha}_2\varepsilon_3\varepsilon_4 - \underline{\alpha}_3\varepsilon_2\varepsilon_4 + \frac{I_\alpha\varepsilon_4^2}{2}\right)\right.$$
$$\left. + C^{[0]}\mathcal{W}^T\left(\underline{\beta}_0\frac{\varepsilon_2^2+\varepsilon_3^2}{2} + \underline{\beta}_2\varepsilon_3\varepsilon_4 - \underline{\beta}_3\varepsilon_2\varepsilon_4 + \frac{I_\beta\varepsilon_4^2}{2}\right)\right]\, d\xi^1$$

$$= \frac{1}{2}\int_0^L \underline{\varepsilon}^{[0]T}C^{[0]}\underline{\varepsilon}^{[0]}\, d\xi^1 + V_t\,, \tag{4.12}$$

where

$$V_t = \int_0^L \underline{\varepsilon}^{[0]T}\left[(Z^T - C^{[0]}\mathcal{T}^T\mathcal{W}^T)\left(\underline{\alpha}_0\frac{\varepsilon_2^2+\varepsilon_3^2}{2} + \underline{\alpha}_2\varepsilon_3\varepsilon_4 - \underline{\alpha}_3\varepsilon_2\varepsilon_4 + \frac{I_\alpha\varepsilon_4^2}{2}\right)\right.$$
$$\left. + C^{[0]}\mathcal{W}^T\left(\underline{\beta}_0\frac{\varepsilon_2^2+\varepsilon_3^2}{2} + \underline{\beta}_2\varepsilon_3\varepsilon_4 - \underline{\beta}_3\varepsilon_2\varepsilon_4 + \frac{I_\beta\varepsilon_4^2}{2}\right)\right]\, d\xi^1\,.$$

From eq. (4.12) it is clear that the strain energy is no longer a quadratic form of $\underline{\varepsilon}^{[0]}$, so that a linear relationship between the $\underline{f}^{[0]}$ and $\underline{\varepsilon}^{[0]}$ no longer exist. It is, however, possible to perform a quasi-linearization, which allows the expression of an increment in $\underline{f}^{[0]}$ in terms of a tangent stiffness matrix post multiplied by the corresponding increment in $\underline{\varepsilon}^{[0]}$. In this case the tangent stiffness matrix is a function of $\underline{\varepsilon}^{[0]}$.

The quasi-linearization is performed by expanding the strain energy in a variational form about a reference strain energy level $\bar{V}$ as follows:

$$V = \bar{V} + \delta V + \frac{1}{2}\delta^2 V + \ldots$$

When dealing with this expansion, it is clear that one can temporarily focus on V_t only. Defining four (6×1) column vectors:

$$\begin{aligned}
\underline{\theta} &= (Z^T - C^{[0]}\mathcal{T}^T\mathcal{W}^T)\underline{\alpha}_0 + C^{[0]}\mathcal{W}^T\underline{\beta}_0\\
\underline{\eta} &= (Z^T - C^{[0]}\mathcal{T}^T\mathcal{W}^T)\underline{\alpha}_2 + C^{[0]}\mathcal{W}^T\underline{\beta}_2\\
\underline{\gamma} &= (Z^T - C^{[0]}\mathcal{T}^T\mathcal{W}^T)\underline{\alpha}_3 + C^{[0]}\mathcal{W}^T\underline{\beta}_3\\
\underline{\mu} &= (Z^T - C^{[0]}\mathcal{T}^T\mathcal{W}^T)\underline{I}_\alpha + C^{[0]}\mathcal{W}^T\underline{I}_\beta
\end{aligned}$$

allows V_t to be written as:

$$V_t = \int_0^L \underline{\varepsilon}^{[0]T}\left[\frac{1}{2}\underline{\theta}(\varepsilon_2^2+\varepsilon_3^2) + \underline{\eta}\varepsilon_3\varepsilon_4 - \underline{\gamma}\varepsilon_2\varepsilon_4 + \frac{1}{2}\underline{\mu}\varepsilon_4^2\right]\, d\xi^1\,.$$

The first variation in V_t can now be written as:

$$\delta V_t = \int_0^L \underline{f}_t^{[0]T} \delta \underline{\varepsilon}^{[0]} \, d\xi^1 \ , \tag{4.13}$$

where the components of $\underline{f}_t^{[0]T} = \lfloor \ f_{t1} \quad f_{t2} \quad f_{t3} \quad f_{t4} \quad f_{t5} \quad f_{t6} \ \rfloor$ are given in Appendix B.

The second variation in V_t can now be written as:

$$\delta^2 V_t = \int_0^L \delta \underline{\varepsilon}^{[0]T} C_t^{[0]}(\underline{\varepsilon}^{[0]}) \delta \underline{\varepsilon}^{[0]} \, d\xi^1 \ , \tag{4.14}$$

where $C_t^{[0]}(\underline{\varepsilon}^{[0]})\delta\underline{\varepsilon}^{[0]} = \delta \underline{f}_t^{[0]}$ and where the elements of matrix $C_t^{[0]}(\underline{\varepsilon}^{[0]})$ are also given in Appendix B.

Having found expressions for δV_t and $\delta^2 V_t$ in terms of $\delta\underline{\varepsilon}^{[0]}$, the first and second variations of the strain energy can be readily found, as is normally done in non-linear finite element analyses. The fact that the sectional stiffness matrix now has meaning only in a quasi-linearized sense, does not really complicate matters with respect to implementation in a multi-body dynamic analysis, since this type of analysis is non-linear in nature anyway. In practice it merely means that within each non-linear analysis iteration, the elemental internal force vector at each Gauss point needs to be supplemented by $\underline{f}_t^{[0]}$ and the elemental sectional stiffness matrix by $C_t^{[0]}$. Modeling of the non-linear strain effect therefore does not involve any additional degrees of freedom, as is the case with the modeling of differential warping, described in section 4.2.

4.4 Conclusion

This chapter discussed the theory of two important extensions to the three dimensional Saint-Venant beam theory: the ability to model differential warping and the non-linear strain effect. The use of this capability is illustrated in chapter 5, where a number of numerical examples are discussed.

CHAPTER 5
NUMERICAL EXAMPLES: CROSS SECTIONAL ANALYSIS

5.1 Introduction

This chapter presents numerical examples of the application of the three dimensional Saint-Venant beam theory to determine sectional properties of beams and the usage of these properties in structural dynamic analysis with beam elements.

A finite element method computer program was developed to perform a two dimensional sectional analysis on a beam cross section, in order to determine the sectional stiffness and inertia tensors C^* and M^*. This analysis is based on the three dimensional Saint-Venant beam theory. After validation of this program, it was linked to two different multi-body dynamic finite element analysis codes, one based on the generalized-α method [19] and the second based on the energy preserving and energy decaying schemes, which are discussed in chapters 6 to 9. For both these programs, the sectional analysis program operates as a pre-processor which calculates the sectional stiffness and inertia tensors for as many cross sections as necessary.

As a first expansion of the sectional analysis program, a stress and strain recovery module was added. A typical result of a multi-body dynamic analysis is the time histories of the stress resultants at various points along the span of a beam. The stress and strain recovery module allows the calculation of the full three dimensional stress and strain time history at any point on the cross section for which the stress resultant time history is known.

With respect to the calculation of the sectional stiffness tensor and stress and strain recovery, the examples quoted in this chapter do not primarily serve to justify the usage of the three dimensional Saint-Venant theory — this has been

done sufficiently well by Borri, et al. [5] — instead, the purpose of these examples are mainly to validate the implementation of this theory in the sectional analysis program.

A second expansion of the sectional analysis program was to add the calculation of all the matrices necessary to implement the advanced beam theory, discussed in chapter 4. The following matrices and column vectors are calculated for each section analyzed: $\mathbf{C}$, $\mathbf{M}$, $\underline{\theta}$, $\underline{\eta}$, $\underline{\gamma}$ and $\underline{\mu}$. Together with this expansion of the sectional analysis program, the multi-body dynamic analysis code based on the generalized-α method was also expanded to provide, in addition to the regular beam element with six degrees of freedom per node (three translations and three rotations), an "advanced beam element", based on the advanced beam theory, with $6 + m$ degrees of freedom per node, where m is the number of modes chosen to be used in the modal approximation.

Some numerical examples are presented in section 5.2, to show how the sectional analysis program was validated during the various stages of development. This section concludes with a discussion of the analysis of a practical helicopter blade section. The results pertaining to the advanced beam theory are presented in section 5.3. To aid in the interpretation of the sectional stiffness and compliance tensors given in various tables in these two sections, a summary of the symbols used are given in table 5.1.

5.2 Validation of central and extremity solution calculation

In this section a number of examples are presented to show how the implementation of the three dimensional Saint-Venant beam theory in the sectional analysis program was validated.

Sectional strain $\underline{\varepsilon}^*$ components		Sectional stress resultant $\underline{f}^*$ components	
ε_1	sectional axial strain	f_1	axial force
ε_2	sectional shear strain with respect to $\vec{e}_1$ and $\vec{e}_2$	f_2	transverse shear force in the $\vec{e}_2$ direction
ε_3	sectional shear strain with respect to $\vec{e}_1$ and $\vec{e}_3$	f_3	transverse shear force in the $\vec{e}_3$ direction
ε_4	elastic curvature component about $\vec{e}_1$ (i.e. twist)	f_4	torsional moment
ε_5	elastic curvature component about $\vec{e}_2$ (i.e. bending)	f_5	bending moment about $\vec{e}_2$
ε_6	elastic curvature component about $\vec{e}_3$ (i.e. bending)	f_6	bending moment about $\vec{e}_3$

Table 5.1: Symbols used in sectional stiffness and compliance tensor listings

5.2.1 Solid rectangular section

The most simple case used for validation of the central and extremity solution calculation is the solid rectangular section of 240 *mm* x *120 mm*, made of an isotropic, homogeneous material, where this section is part of a straight, untwisted beam (i.e. a beam with zero curvature). Giavotto et al. [3] analyzed this section and quoted both central and extremity solution results. The same mesh as in [3] was used in the validation: nine eight-noded quadrilateral elements arranged in a 3x3 pattern, resulting in 120 degrees of freedom. The results of [3] were duplicated exactly by the sectional analysis program, with respect to both the central and extremity solutions.

5.2.2 Hollow rectangular section

Whereas the above example is a good test for the basic operation of the program, the second example provided validation of the capability to analyze a section made of non-homogeneous anisotropic materials. This case deals with a beam made of composite material, with zero curvature and with a hollow, thin-walled, rectangular cross section[1]. This beam was the object of experimental, numerical and analytical studies, carried out by Chopra, et al. [28, 29]. The results of these studies were subsequently used by Borri, et al. [5] in a comparison with results obtained with the three dimensional Saint-Venant beam theory.

The outside dimensions of the cross section is 0.953 *in.* x 0.537 *in.* Results are available for a number of different composite lay-ups in the walls of the section. In all cases all four walls consist of six plies of thickness of 0.005 *in.*, giving a constant wall thickness of 0.03 *in.* The material properties are listed in table 5.2. Three different lay-ups were analyzed with the sectional analysis program and the results compared to those of [5]: two which result in beam extension-torsion coupling and

[1]To distinguish this cross section from another hollow rectangular section of different dimensions, referred to in section 5.3.2, the cross section described in this section is labeled "Hollow rectangular section 1".

Longitudinal modulus of elasticity	E_L	20.59×10^6 *psi*
Transverse modulus of elasticity	E_T	1.42×10^6 *psi*
Shearing modulus	G_{LT}	0.87×10^6 *psi*
Poisson's ratio	ν_{LT}	0.42

Table 5.2: Hollow rectangular section 1: Ply material properties

one which results in beam torsion-bending coupling. The lay-ups of these three cases are given in table 5.3, specimens numbers 2, 3 and 8. These numbers correspond to the numbers assigned to these lay-ups by [5]. The finite element mesh used in the sectional analysis is shown in figure 5.1. This mesh consists of 288 eight-noded quadrilateral elements, with 960 nodes and 2880 degrees of freedom, and is similar, but not identical, to the mesh used by [5]. The choice of the beam reference line is such that its intersection with the plane of the section is coincident with the geometric center of the section.

Two diagonal and two off-diagonal components of the sectional compliance tensor, as calculated with the three dimensional Saint-Venant beam theory, are listed in [5]. These are compared with the results calculated with the sectional analysis program in tables 5.4 and 5.5. Note that the signs of the results of [5] are reversed in table 5.5, as it is assumed that the direction for a positive fiber orientation angle used by [5] is the reverse of the one used in this work. The results of the sectional analysis program are seen to be in every good agreement with those listed in [5].

The three dimensional stress and strain distributions across the wall were also calculated by Borri, et al. and are given in graph form, for one of the lay-ups (specimen 3) at two positions and for an unit applied axial force and an unit applied

Specimen Number	Upper wall	Lower wall	Left side wall	Right side wall
2	$[15°]_6$	$[15°]_6$	$[15°]_6$	$[15°]_6$
3	$[30°, 0°]_3$	$[30°, 0°]_3$	$[30°, 0°]_3$	$[30°, 0°]_3$
8	$[15°]_6$	$[-15°]_6$	$[\mp 15°]_3$	$[\pm 15°]_3$
A	$[15°]_6$	$[15°]_6$	$[\mp 15°]_3$	$[\pm 15°]_3$

A positive fiber angle is measured as a positive rotation about an inward normal to the wall center line. The 0° orientation angle implies alignment with the $\vec{e}_1$ axis. All lay-up sequences are specified from the inside towards the outside.

Table 5.3: Hollow rectangular section 1: Lay-up of cases analyzed

Specimen Number	Borri, et al. [5]		Sectional analysis program	
	S^*_{44} $rad/in.^2/lb.$	S^*_{55} $rad/in.^2/lb.$	S^*_{44} $rad/in.^2/lb.$	S^*_{55} $rad/in.^2/lb.$
2	1.125×10^{-4}	2.665×10^{-5}	1.120×10^{-4}	2.665×10^{-5}
3	6.445×10^{-5}	1.844×10^{-5}	6.440×10^{-5}	1.841×10^{-5}
8	8.332×10^{-5}	2.380×10^{-5}	8.333×10^{-5}	2.375×10^{-5}

Table 5.4: Hollow rectangular section 1: Two diagonal components of the sectional compliance tensor, for different material lay-ups

Specimen Number	Borri, et al. [5]		Sectional analysis program	
	S^*_{14} $1/in./lb.$	S^*_{45} $rad/in.^2/lb.$	S^*_{14} $1/in./lb.$	S^*_{45} $rad/in.^2/lb.$
2	-8.34×10^{-6}	0	-8.34×10^{-6}	0
3	-2.70×10^{-6}	0	-2.69×10^{-6}	0
8	0	-2.47×10^{-5}	0	-2.47×10^{-5}

Table 5.5: Hollow rectangular section 1: Two off-diagonal components of the sectional compliance tensor, for different material lay-ups

torsional moment [5, pages 52–59]. Within the accuracy allowed by these graphs, these results were duplicated with the sectional analysis program.

Another lay-up for the walls of the hollow rectangular beam was investigated, one not considered by [5] and therefore labeled as specimen A in table 5.3. This case was actually analyzed due to a misinterpretation of lay-up specification in [5], and could therefore not be used for validation. The results are nevertheless mentioned here, because they clearly show the importance of the three dimensional Saint-Venant theory in the analysis of beams made of composite materials. A sectional analysis was also performed on the section with this lay-up with another program, based on a thin walled approximation to the classical Saint-Venant beam theory. The sectional stiffness tensor, as calculated by the thin walled approximation to the classical Saint-Venant beam theory, and the three dimensional Saint-Venant beam theory, are given in tables 5.6 and 5.7, respectively. Both these tensors were calculated for the choice of the beam reference line such that its intersection with the plane of the section is coincident with the geometric center of the section. The most significant differences between these two tensors — as large as 15.2% — are between the diagonal components and are summarized in table 5.8. It is believed

	ε_1	ε_2	ε_3	ε_4	ε_5	ε_6
f_1	143.1	0.000	0.000	7.077	0.000	0.000
f_2	0.000	9.136	0.000	0.000	-4.864	0.000
f_3	0.000	0.000	4.053	0.000	0.000	-2.015
f_4	7.077	0.000	0.000	1.708	0.000	0.000
f_5	0.000	-4.864	0.000	0.000	7.020	0.000
f_6	0.000	0.000	-2.015	0.000	0.000	17.36

Unit system: *lb.-in.*

Table 5.6: Hollow rectangular section 1: Sectional stiffness tensor C^*, multiplied by 10^{-4}, of the lay-up specimen A, as calculated with a thin walled approximation to the classical Saint-Venant beam theory.

	ε_1	ε_2	ε_3	ε_4	ε_5	ε_6
f_1	128.2	0.000	.0154	7.095	0.000	.1416
f_2	0.000	8.938	0.000	0.000	-4.715	0.000
f_3	.0154	0.000	4.456	-.0037	0.000	-1.864
f_4	7.095	0.000	-.0037	1.734	0.000	.0374
f_5	0.000	-4.715	0.000	0.000	6.703	0.000
f_6	.1416	0.000	-1.864	.0374	0.000	15.07

Unit system: *lb.-in.*

Table 5.7: Hollow rectangular section 1: Sectional stiffness tensor C^*, multiplied by 10^{-4}, of the lay-up specimen A, as calculated with the three dimensional Saint-Venant beam theory

that these differences can be ascribed to significant in-plane warping of the section, especially in the cases of bending about the $\vec{e}_3$ axis and axial loading, due to the nature of the composite lay-up. The classical Saint-Venant theory is believed to be inaccurate, because it cannot capture this in-plane distortion due to its basic assumption, shared by the Bernoulli theory, that the cross section does not deform in its own plane. The three dimensional Saint-Venant beam theory, on the other hand, was specifically developed to capture all sectional warping, and is therefore believed to give the more reliable result of the two methods. Interestingly enough, if this comparison is repeated with homogeneous isotopic material properties, the classical and three dimensional Saint-Venant theories are in pretty good agreement, even though the classical theory is implemented with a thin walled approximation. In this case the in-plane cross sectional distortion under either axial loading or bending is limited to Poisson effects, which are accounted for in the implementation

Diagonal component corresponding to	Classical Saint-Venant theory	Three dimensional Saint-Venant theory	Percentage error
f_1 & ε_1	1.431×10^6	1.282×10^6	11.6
f_2 & ε_2	9.136×10^4	8.938×10^4	2.2
f_3 & ε_3	4.053×10^4	4.456×10^4	-9.0
f_4 & ε_4	1.708×10^4	1.734×10^4	-1.5
f_5 & ε_5	7.020×10^4	6.703×10^4	4.7
f_6 & ε_6	1.736×10^5	1.507×10^5	15.2

Unit system: *lb.-in.*

Three dimensional Saint-Venant beam theory
result used as reference in error calculation

Table 5.8: Hollow rectangular section 1: Comparison of the diagonal components of the sectional stiffness tensor C^*, as calculated with a thin walled approximation to the classical Saint-Venant beam theory, and the three dimensional Saint-Venant beam theory

of the classical Saint-Venant theory, thus allowing accurate results. This example illustrates that the three dimensional Saint-Venant theory is to be preferred above the classical Saint-Venant theory in the analysis of any beam section where the possibility of significant in-plane warping exists, in particular modern helicopter blades made of composite materials.

5.2.3 Sections of beams with high curvature

The two examples treated in this section deals with solid section highly curved beams, the first a 120 *mm* x 120 *mm* square section made of an isotropic material, with a 200 *mm* radius of curvature, the second being a 6 *mm* x 1 *mm* rectangular section made of four layers of composite material, in a $[0°/90°]_s$ lay-up. These two cases were once again analyzed by Borri, et al. [5], but the only results published are graphs of some components of three dimensional stress and strain. Suffice it to say, then, that the stress and strain graphs [5, pages 40 and 63] were duplicated with the sectional analysis program, with meshes of similar size, to the accuracy allowed by these graphs.

5.2.4 The ONERA section: an experimental helicopter rotor blade

The French national research organization responsible for aeronautical engineering, ONERA, developed an experimental all composite rotor blade, highly flexible in torsion. This organization then performed a well controlled set of experiments to measure the static response of the blade when subjected to various loading conditions. One of the purposes of this research effort is the validation by ONERA of their in-house rotorcraft structural dynamics code. This validation is currently under way and is taking on a two phase approach.

During the first phase, which has recently been completed, ONERA calculated the blade static response with their blade modeling software, but using a single

sectional stiffness tensor calculated with the sectional analysis program developed as part of this thesis research project, for a large spanwise portion of the blade. This is reasonable, because the blade does in fact have a constant section for a large portion of its span, around its mid-span position. In the regions where the section is different from the mid-span section, sectional properties derived from a different source were used. The results of this investigation is published in [30].

During the second phase, which is still to be completed, ONERA plans to use sectional stiffness tensors calculated with the sectional analysis program at all substantially different sections along the span. It is expected that, in addition to the ONERA analysis, an analysis of this blade, with the use of the advanced beam element, will prove to be very interesting, once all the different sectional analyses are completed.

The mid-span section of the ONERA blade, used in the first phase of the project (here-after referred to as the ONERA section), has the following geometric properties: it has an OA 209 airfoil shape with a 123 mm chord length, including an aluminum trailing edge tab. It has a fairly high pre-twist of $14.12°/m$, with the axis of pre-twist at 25% chord, from the leading edge. The two dimensional finite element mesh used to perform the sectional analysis is shown in figure 5.2, with details of the leading and trailing edges in figures 5.3 to 5.5. The section comprises the following components, which are indicated on the above mentioned finite element mesh graphs: a four layered composite skin, one unidirectional leading edge and two unidirectional trailing edge stiffeners — one on either side of the root of the aluminum trailing edge tab, a leading edge balancing mass and foam, which fills the remaining cavity. The balancing mass and tab are not continuous in the spanwise direction, and are therefore considered to be non-structural masses, with respect to the out-of-plane stiffness properties. In the plane of the section their full stiffness contribution were taken into account. The materials used for the various

Four layered composite skin	
Inner layer:	8 warp woven E glass fiber E/1454/759 (BROCHIER)
Outer Layers:	$[0°, 90°, 0°]$ E glass fiber Fibredux 913-GE-5 (BROCHIER)
Unidirectional leading and trailing edge stiffeners:	R Glass fiber BR/H10/30 (BROCHIER)
Leading edge balancing mass	INERMET
Trailing edge tab	Aluminum
Foam filler	Polyurethane, 80 kg/m^3

Table 5.9: ONERA section: Material properties

components are summarized in table 5.9. The finite element model of the section comprised 630 eight noded quadrilateral and six noded triangular elements and 1959 nodes for a total of 5877 degrees of freedom. In the thickness direction, the skin was modeled with one element per composite layer.

To study the effect of the high pre-twist of this blade, the analysis was performed both with and without the pre-twist. The calculated sectional compliance and stiffness tensors, with and without the pre-twist, are given in tables 5.10 to 5.13. Considering either the stiffness or compliance tensor: without pre-twist, the 3 x 3 sub-matrix pertaining to (f_1, f_5, f_6) and $(\varepsilon_1, \varepsilon_5, \varepsilon_6)$ is seen to be totally decoupled from the 3 x 3 sub-matrix pertaining to (f_2, f_3, f_4) and $(\varepsilon_2, \varepsilon_3, \varepsilon_4)$. This is due to the fact that the material properties are such that no coupling between direct stress/strain and shear strain/stress is introduced. The first mentioned sub-matrix is driven by the direct stress and strain characteristics, while the second mentioned sub-matrix is driven by shear stress and strain characteristics. In any case where

	f_1	f_2	f_3	f_4	f_5	f_6
ε_1	625.9	0.000	0.000	0.000	-82.49	2.979
ε_2	0.000	13360.	-2219.	186.4	0.000	0.000
ε_3	0.000	-2219.	10420.	-246.6	0.000	0.000
ε_4	0.000	186.4	-246.6	148.4	0.000	0.000
ε_5	-82.49	0.000	0.000	0.000	70.07	-.9530
ε_6	2.979	0.000	0.000	0.000	-.9530	.7102

Unit system: *N-mm*

Table 5.10: ONERA section: Cross sectional compliance tensor S^*, multiplied by 10^{10}, for the case with no pre-twist

	f_1	f_2	f_3	f_4	f_5	f_6
ε_1	629.6	-29.30	32.57	-22.69	-82.59	2.707
ε_2	-29.30	13290.	-2192.	185.0	3.342	1.697
ε_3	32.57	-2192.	10420.	-244.6	-1.475	-.7219
ε_4	-22.69	185.0	-244.6	147.1	.5043	1.699
ε_5	-82.59	3.342	-1.475	.5043	70.09	-.9474
ε_6	2.707	1.697	-.7219	1.699	-.9474	.7315

Unit system: *N-mm*

Table 5.11: ONERA section: Cross sectional compliance tensor S^*, multiplied by 10^{10}, for the case with the correct pre-twist

	ε_1	ε_2	ε_3	ε_4	ε_5	ε_6
f_1	19.09	0.000	0.000	0.000	21.78	-50.85
f_2	0.000	.7833	.1494	-.7359	0.000	0.000
f_3	0.000	.1494	1.027	1.520	0.000	0.000
f_4	0.000	-.7359	1.520	70.84	0.000	0.000
f_5	21.78	0.000	0.000	0.000	170.2	137.0
f_6	-50.85	0.000	0.000	0.000	137.0	14480.

Unit system: *N-mm*

Table 5.12: ONERA section: Cross sectional stiffness tensor C^*, multiplied by 10^{-6}, for the case with no pre-twist

	ε_1	ε_2	ε_3	ε_4	ε_5	ε_6
f_1	19.08	-.0020	.0214	3.489	21.78	-50.48
f_2	-.0020	.7875	.1481	-.7442	-.0312	.0150
f_3	.0214	.1481	1.027	1.559	-.0126	-3.048
f_4	3.489	-.7442	1.559	74.12	1.210	-180.2
f_5	21.78	-.0312	-.0126	1.210	170.2	137.1
f_6	-50.48	.0150	-3.048	-180.2	137.1	14450.

Unit system: *N-mm*

Table 5.13: ONERA section: Cross sectional stiffness tensor C^*, multiplied by 10^{-6}, for the case with the correct pre-twist

these two sub-matrices are decoupled, the concepts of sectional shear center and axial stiffness centroid are meaningful. It can be shown that the first mentioned sub-matrix is not diagonal, because the intersection of the beam reference line with the sectional plane is not coincident with the sectional axial stiffness centroid, and the $\vec{e}_2$ and $\vec{e}_3$ axes are not parallel to the principal axes of bending. Likewise, it can be shown that the second mentioned sub-matrix is not diagonal, because the intersection of the beam reference line with the sectional plane is not coincident with the sectional shear center, and the $\vec{e}_2$ and $\vec{e}_3$ axes are not parallel to the principal axes of shear. This, in fact, provides a definition for the sectional shear center and axial stiffness centroid, as those two points on the sectional plane, which, if chosen for the intersection of the beam reference line with this plane and given the decoupling of the two 3 x 3 sub-matrices described above, would result in the decoupling of f_4, ε_4 from $(\varepsilon_2, \varepsilon_3), (f_2, f_3)$, and f_1, ε_1 from $(\varepsilon_5, \varepsilon_6), (f_5, f_6)$, respectively[2]. Once either of these decouplings is effected, the principal axes of shear or bending, whichever is the case, may be established as those directions, which, if chosen for $\vec{e}_2$ and $\vec{e}_3$, would decouple f_2, ε_2 from ε_3, f_3, and f_5, ε_5 from ε_6, f_6, respectively[3]. With material coupling between direct stress/strain and shear strain/stress, or with non-zero pre-twist, the sectional stiffness and compliance tensors are in general fully populated. For the pre-twisted blade this is evident in tables 5.11 and 5.13. When these tensors are fully populated, the concepts of *sectional* shear center, axial stiffness centroid and principal axes of shear and bending break down, because the necessary decoupling cannot be effected merely by choice of reference line location and the directions of $\vec{e}_2$ and $\vec{e}_3$.

The intrinsic characteristic warping functions of the ONERA section are shown

[2]These two decouplings implies that the torsional and axial sectional degrees of freedom, respectively, are decoupled from all the other sectional degrees of freedom.

[3]These two decouplings implies that the two sectional transverse shear and two bending degrees of freedom, respectively, are decoupled from all the other sectional degrees of freedom.

(exaggerated) in figures 5.6 to 5.11. On these graphs, the deformed shapes are drawn in a slightly lighter shade than the undeformed two dimensional mesh, which lies in the Y–Z plane[4]. Of particular interest is the intrinsic characteristic warping function associated with a transverse shear force f_2, shown in figure 5.7. This figure clearly shows the effect of the high stiffness of the leading and trailing edge stiffeners, as compared to the low stiffness of the foam, in the three distinct, almost planar areas into which the section deforms. It is also to be noted that in all six cases, the intrinsic characteristic warping function is a fully three dimensional deformation. This is related to the fact that for the twisted blade the stiffness and compliance tensors are fully populated. In the case of a beam where the direct stress/strain related sub-matrix is decoupled from the shear stress/strain related sub-matrix, as explained above, the characteristic intrinsic warpings associated with axial force or bending moments are strictly in-plane (i.e. two dimensional), while the characteristic intrinsic warpings associated with transverse shear forces or torsional moments are strictly out-of-plane (i.e. one dimensional). An example of such a case is discussed in section 5.3.

To conclude this section, the exercise with the ONERA section also illustrated the following important point: with traditional beam models, which are based on the Bernoulli assumption that the section does not deform in its own plane, it is customary to neglect the contribution of low stiffness filler materials like foam, especially if the calculations are of a preliminary nature. This approach can lead to significant errors though, when applied in the case of the three dimensional Saint-Venant beam theory. The filler material, even though it may be relatively flexible and therefore have a small direct contribution to the sectional stiffness, may play an important role in preventing the collapse of the section due to in-plane warping. This is especially true of sections with very thin walls, like the ONERA section. If an analysis

[4]The introduction of (X, Y, Z) in these figures, rather than $(\vec{e}_1, \vec{e}_2, \vec{e}_3)$, is a by-product of the commercially available mesh generation program that was used to generate the mesh.

is made on a hollow section comprising only the four layered skin of the ONERA section, with appropriate modification at the trailing edge to close the section in the absence of the trailing edge tab, the torsional stiffness[5] of the section is calculated by the sectional analysis program as 28.11 $N{\cdot}m^2$, in the case of zero pre-twist. An approximate analytical solution [31, pp. 332 and 333] for a closed thin-walled hollow section of an untwisted beam, based on the assumption of no deformation in the plane of the cross section, renders a torsional stiffness of 27.42 $N{\cdot}m^2$, which is in good agreement with the program result. As mentioned above, the material of the ONERA blade does not introduce any coupling between direct stress/strain and shear strain/stress, so that the untwisted hollow blade does not have any in-plane components in the intrinsic characteristic warping function associated with torsional loading. The section therefore does not violate the assumption of the approximate analytical solution, which explains the good correlation between its result and the program result. If the correct pre-twist is introduced, the intrinsic characteristic warping function associated with torsional loading is no longer out-of-plane only, and the in-plane components tend to collapse the section. The result is that the torsional stiffness as calculated by the sectional analysis program, drops to 16.50 $N{\cdot}m^2$, whereas one would expect the torsional stiffness of a beam to increase with increasing pre-twist, if the section does not significantly deform in its own plane. If the whole sectional cavity is now filled with foam only, the torsional stiffness calculated by the sectional analysis program, with the pre-twist, increases to 34.68 $N{\cdot}m^2$. This result, compared to the result with no pre-twist, reflects the expected trend. The additional stiffness is not directly attributed to the foam, but the foam significantly reduces the in-plane components of the warping, causing the stiffening of the section in torsion in an indirect way. This result clearly indicates the importance of including relatively flexible filler materials in the model during sectional analysis with the

[5] the reciprocal of S^*_{44}

three dimensional Saint-Venant beam theory. It should be clearly understood that the requirement to also model flexible filler materials is *not* a disadvantage of using the three dimensional Saint-Venant beam theory; instead, it actually emphasizes how the modeling of the beam with this method represents a solution of the beam problem that is closer to physical reality than traditional beam models based on assumptions of no cross sectional deformation.

5.3 Advanced beam theory

The validation of the advanced beam theory, and specifically the implementation of the advanced beam element, is difficult, due to the lack of analytical solutions with which the results can be compared. An analytical solution for the torsional problem of a thin walled closed section under constrained warping conditions is available, and will be used in section 5.3.2 in the validation of the advanced beam element in torsion. With respect to the other five stress resultants, it is realized that the advanced beam element has, to a large degree, not been validated yet. On the other hand, it is also true that when dealing with constrained warping, especially in the context of helicopter rotor blades and flex-beams, the torsional problem is generally considered to be significantly more important than the two transverse shear problems, while the warping problem associated with axial and bending loading has received little attention. These seemingly less important problems may become more important in the future as more exotic materials and geometric configurations, which introduce more coupling in the sectional stiffness tensor, are employed. One possibility for further validation work is the comparison of results calculated with the advanced beam element with those obtained with three dimensional elements, quite similar to the approach followed by Borri et al. with respect to the central solution [5]. Comparison with experimental studies would also be beneficial. A good opportunity for such a comparison will be afforded by the completion of the

second phase of the research project dealing with the ONERA blade, mentioned in section 5.2.4.

Three examples are now presented to illustrate how the advanced beam theory and its implementation has been validated to date.

5.3.1 Comparison between the advanced beam element and the regular beam element, in the absence of differential warping and nonlinear strain effects

The first step in the validation of the advanced beam element, is to make sure that it does in fact give the same response as the regular beam element using the central solution stiffness, when a case involving no differential warping and no nonlinear strain effects, is analyzed, especially if the modal basis of the advanced beam element is chosen to include all six the intrinsic characteristic warping functions. Several such tests were conducted, and one example will be discussed briefly: a straight, untwisted cantilevered beam of length 4.5 *in.* with free warping at at all spanwise locations, including the cantilevered end, subjected to the following static load stepping sequence: an applied tip torque of 50 *lb.in.* followed by the addition of an applied tip bending moment about the $\vec{e}_3$ axis, also of 50 *lb.in.* The spanwise homogeneous cross section of the beam is that corresponding to the hollow rectangular section, discussed in section 5.2.2, using specimen 2 in table 5.3. The beam is modeled with, in the one case, three cubic regular beam elements, and in the second case three cubic advanced beam elements, employing a three point Gaussian quadrature in both cases. In the advanced beam element case, the modal basis consists of the six intrinsic characteristic warping functions.

The first six natural vibration eigenvalues of the beam were calculated, in the unloaded configuration, and for both load steps. The no load eigenvalues are summarized in table 5.14, and the eigenvalues under both the tip torsional and

Eigenvalue Number	Frequency (Hz)		Mode description
	Regular beam element	Advanced beam element	
1	1 115.9	1 115.9	Bending about $\vec{e}_2$
2	1 699.1	1 694.8	Bending about $\vec{e}_3$
3	3 119.0	3 129.2	Torsion / Axial
4	5 032.1	5 268.5	Bending about $\vec{e}_2$
5	6 864.6	7 148.0	Bending about $\vec{e}_2$
6	9 358.1	9 608.2	Torsion / Axial

Table 5.14: Comparison of the natural frequencies of vibration of a cantilevered beam with free warping and no load, as calculated with regular and advanced beam elements

bending moments in table 5.15. The tip displacement and conformal rotation vector components under the loading of both load steps are shown in table 5.16.

It needs to be pointed out that, due to the material coupling associated with the section specimen 2, all natural vibration bending modes labeled to be about the $\vec{e}_2$ axis also contain significant bending about $\vec{e}_3$, and vice versa. The fifth mode in both tables 5.14 and 5.15 was particularly difficult to label; it is basically a third bending about $\vec{e}_2$ coupled with a second bending about $\vec{e}_3$ mode. Similarly, torsional and axial motion are highly coupled in the modes which would otherwise be labeled torsional modes. This is to be expected, if the coupling term listed for this section in table 5.5 is taken into account. In the unloaded beam, the bending and torsional/axial modes are fully decoupled. In the case of the fully loaded beam, however, the torsional/axial modes and the bending modes are slightly coupled.

There is good agreement between the two models on the mode shapes. With respect to the natural frequencies the agreement is fairly good, though not exact.

Eigenvalue Number	Frequency (Hz)		Mode description
	Regular beam element	Advanced beam element	
1	1 116.4	1 113.5	Bending about $\vec{e}_2$
2	1 699.5	1 685.7	Bending about $\vec{e}_3$
3	3 118.8	3.127.0	Torsion / Axial
4	5 043.9	5 285.3	Bending about $\vec{e}_2$
5	6 850.6	7 122.9	Bending about $\vec{e}_2$
6	9 358.1	9 602.5	Torsion / Axial

Table 5.15: Comparison of the natural frequencies of vibration of a cantilevered beam with free warping, and applied tip bending and torsional moments of 50 *lb.in.* each, as calculated with regular and advanced beam elements

The largest difference is found in the case of the fourth mode, where the advanced beam element model results are 4.7% and 4.8% higher than the results of regular beam element model, in the no loading and full loading case, respectively.

The reason for the differences in the natural frequencies being small, for both methods, between the unloaded and fully loaded cases, is obvious when the calculated tip displacements, given in table 5.16, are considered. It is clear that the applied loading is so small that the beam still behaves in a fairly linear manner. The two models are in good agreement with respect to the calculated tip displacements and rotations. In the case of the largest difference, the advanced beam element result is 1.8% higher than the regular beam element result.

It is therefore concluded that the advanced beam element with the six intrinsic characteristic warping functions in the modal basis, essentially gives the same results as a regular beam element using the sectional stiffness properties obtained from the

Applied tip loading:		Torsional moment of 50 *lb.in.* only	Torsional and bending moments of 50 *lb.in.* (bending about $\vec{e}_3$)
Regular beam element	u_{s1}	-1.876×10^{-3}	-1.880×10^{-3}
	u_{s2}	0.0	5.391×10^{-3}
	u_{s3}	0.0	3.526×10^{-3}
	a_1	2.521×10^{-2}	2.521×10^{-2}
	a_2	0.0	0.0
	a_3	0.0	2.417×10^{-3}
Advanced beam element	u_{s1}	-1.888×10^{-3}	-1.895×10^{-3}
	u_{s2}	0.0	5.479×10^{-3}
	u_{s3}	0.0	3.588×10^{-3}
	a_1	2.521×10^{-2}	2.523×10^{-2}
	a_2	0.0	0.0
	a_3	0.0	2.456×10^{-3}

Displacements in *in.*
All components in $\mathcal{S}$ system

Table 5.16: Comparison of the components of the static tip displacement and conformal rotation vectors, of a cantilevered beam with free warping, under applied tip bending and torsional moments, as calculated with regular and advanced beam elements

central solution, in the case of free warping at all spanwise locations.

5.3.2 Clamped-free beam with hollow rectangular section

In this section a straight, untwisted clamped-free beam with a thin walled, hollow rectangular cross section, subjected to a tip torque, is considered. In terms of boundary conditions, this beam differs from the cantilevered beam described in section 5.3.1 in that the warping is fully constrained at the clamped end (or root) of the beam, while it is free everywhere else. The analysis will be limited to materials which do not introduce any coupling, and a case with constant wall thickness. An analytical solution is available for this example [31, pp. 338–341]. Following the implementation of this solution by [6], the torsional rotation of the tip of the beam ϕ_t under applied loading of a tip torque T_t , is given by:

$$\phi_t = \left[1 - \left(\frac{a-b}{a+b}\right)^2 \frac{\tanh kL}{kL}\right] \frac{LT_t}{I_p - C^2/J} \ , \tag{5.1}$$

where L is the length of the beam, $2a$ and $2b$ are the width and height of the rectangular cross section, respectively; using the notation of [32, p. 121], $A_{nn} = A_{11} - A_{12}^2/A_{22}$ and $A_{qq} = A_{66}$ are the laminate axial and shear stiffness coefficients for a laminate with no coupling ($A_{16} = A_{26} = 0$) and in which the circumferential direct stress is zero, and

$$J_w = \frac{4}{3} A_{nn} \frac{a^2 b^2 (a-b)^2}{a+b} \ ,$$

$$J = -C = 4 A_{qq} ab \frac{(a-b)^2}{a+b} \ ,$$

$$I_p = 4ab A_{qq} (a+b) \ ,$$

$$k^2 = \frac{J I_p - C^2}{I_p J_w} \ .$$

A 480 *mm* long beam with a 160 *mm* x 40 *mm* cross section[6] was analyzed. The wall thickness is 1.5 *mm*. The beam material is T300/5208 Graphite/epoxy.

[6]This section is labeled "Hollow rectangular section 2".

Longitudinal modulus of elasticity	E_L	$181.0 \times 10^9\ N/m^2$
Transverse modulus of elasticity	E_T	$10.3 \times 10^9\ N/m^2$
Shearing modulus	G_{LT}	$7.17 \times 10^9\ N/m^2$
Poisson's ratio	ν_{LT}	0.28

Table 5.17: Hollow rectangular section 2: Ply material properties

Three different lay-ups of this material were investigated, in each case the specified lay-up was used for all four walls: $[0°]_{12}$, $[45°_2, -45°_2, 0°_2]_s$ and $[0°_2, 45°_2, -45°_2]_s$. Once again, the 0° orientation angle implies alignment with the $\vec{e}_1$ axis. Due to the thin walled assumption, the analytical result is the same for the last two layups. The material properties are given in table 5.17.

The sectional analysis program was used to determine the sectional stiffness properties, with a mesh of 480 eight noded quadrilateral elements and 1600 nodes, for a total of 4800 degrees of freedom.

Once again the beam was analyzed with both regular and advanced beam elements. At the tip of the beam, the regular beam element is expected to perform well. Near the root of the beam, however, it is inaccurate, because it does not provide for the differential warping in the root zone and the warping constraint at the root. The beam is modeled with, in the one case, three equal length cubic regular beam elements, and in the second case, three equal length cubic advanced beam elements, employing a three point Gaussian quadrature in both cases. In the advanced beam element case, the modal basis consists of the six intrinsic characteristic warping functions.

In the analytical solution, eq. 5.1, the coefficient $\left[1 - \left(\frac{a-b}{a+b}\right)^2 \frac{\tanh kL}{kL}\right]$ may be considered as a correction factor that accounts for the constrained warping, through

the term $\left(\frac{a-b}{a+b}\right)^2 \frac{\tanh kL}{kL}$, because in the case of free warping, the tip rotation is given by

$$\phi_t = \frac{LT_t}{I_p - C^2/J} \quad .$$

The term $\left(\frac{a-b}{a+b}\right)^2 \frac{\tanh kL}{kL}$ is large for materials with large A_{nn}/A_{qq} ratios, such as spanwise unidirectional composites (and it is also large for short beams). For metals or materials of which the properties approach isotropy, this ratio is usually relatively small, so that the effect of constrained warping on the tip rotation is not so prominent as for a spanwise unidirectional composite beam of the same length. This trend is clearly born out by the analysis. The tip rotation ϕ_t as calculated using the analytical solution and the two finite element models are summarized in table 5.18. It is clear that the difference between the regular beam element result and the analytical solution is much smaller in the case of the $[45^\circ_2, -45^\circ_2, 0^\circ_2]_s$ and $[0^\circ_2, 45^\circ_2, -45^\circ_2]_s$ lay-ups, than in the case of the spanwise unidirectional beam.

The advanced beam element seems to over-correct for the effect of the constrained warping (i.e. adding a warping constraint to a beam, stiffens the beam; the advanced beam element seems to exaggerate this stiffening effect). The reason for this is not clear at this time. One possible explanation for the discrepancy is the fact that some small relaxation of the warping constraint is inherent in the thin walled assumption of the analytical solution. If this were the (only) reason for the discrepancy, the analytical and advanced beam element results would approach each other as the wall thickness is reduced. A single analysis on a beam of even smaller wall thickness, however, did not show such a trend, but may also not be conclusive in ruling out this explanation altogether.

The results of table 5.18 show that the advanced beam element performs significantly better than the regular beam element, in the case of constrained torsional warping. This performance improvement warrants the implementation of this element in a multi-body analysis program which is to be used in helicopter structural

Layup:		$[0°]_{12}$	$[45°_2, -45°_2, 0°_2]_s$	$[0°_2, 45°_2, -45°_2]_s$
Analytical Solution	Angle	1.050×10^{-4}	2.446×10^{-5}	2.446×10^{-5}
Regular beam element	Angle	1.168×10^{-4}	2.521×10^{-5}	2.525×10^{-5}
	% difference	11.2	3.1	3.2
Advanced beam element	Angle	9.868×10^{-5}	2.411×10^{-5}	2.414×10^{-5}
	% difference	-6.0	-1.4	-1.3

Rotation angle in radians
Percentage difference is relative to analytical solution

Table 5.18: Hollow rectangular section 2: Comparison of the tip rotation angle under an applied tip torque, as calculated using the analytical solution, and two finite element models employing either regular or advanced beam elements

dynamics. Modern blade to hub attachments, like flexbeams, regularly employ spanwise unidirectional fibers over a short span, with a high degree of constrained warping. The performance of the advanced beam element in such a situation is clearly illustrated by the next example.

5.3.3 The MBB prototype tail rotor flexbeam

A rotor structural dynamic analysis was performed on the four bladed prototype bearingless tail rotor, developed by what then used to be the MBB helicopter company, in Germany in the late 1970s [33]. This rotor was developed as an alternative tail rotor for this company's MBB-BO 105 and MBB-BK 117 light utility helicopters. In this case, the rotor blade is connected to the hub by, (1) on the hub side, a short beam with a rectangular section, stiff in bending in the lead-lag direction and flexible in bending in the flap direction, which performs as "flapping hinge", and (2) on the blade side, a longer beam with a cruciform section. This cruciform section beam is more flexible in bending in the lead-lag direction and more stiff in bending in the flap direction than the first beam, and exceptionally flexible in torsion. It therefore acts as both flap and lead-lag "hinges", but primarily as "pitch bearing". The rotor does not have any other device which accommodates the pitch control of the blade; the blade pitch control mechanism, which is connected directly to the blade outboard of the cruciform section beam, actually needs to twist this beam to effect any pitch rotation of the blade.

The structural part of the cruciform section is shown in figure 5.12. Each arm of the cruciform is slotted towards the sectional shear center, to reduce torsional stiffness. The beam is made of glass fiber, in two fiber orientations: the central part of each of the four arms is made of a $[\pm 45°]$ layup, which supports two thick, spanwise unidirectional straps on either side, eight straps in total. The fiber orientation is also indicated in figure 5.12, the parts of the section with the $[\pm 45°]$ layup being

shaded to distinguish these from the unidirectional parts. The four unidirectional straps on the two horizontal arms each carries an elastomeric lead-lag damping device, which was not taken into account in this analysis, as it does not have any significant contribution to the sectional stiffness. Taking into account that flapping corresponds to bending about $\vec{e}_2$ and lead-lag motion to bending about $\vec{e}_3$, figure 5.12 also indicates that the cruciform section is more flexible in flap-wise bending than in lead-lag bending.

From the figures contained in [33] it is clear that the warping at the outboard side of the cruciform flexbeam is to a large degree fully constrained. At the inboard side there is a gradual transition from the "flapping hinge" rectangular section to the cruciform section, which makes it difficult to judge whether the warping is constrained or not. As the cruciform flexbeam is relatively short and a large portion of its material is spanwise unidirectional fibers, it is significantly stiffened in torsion by constrained torsional warping effects.

The presence of spanwise unidirectional fibers at a location relatively far from the sectional axial stiffness centroid, together with the high axial centrifugal loading, also makes the cruciform flexbeam a prime candidate to study the non-linear strain effect (trapeze effect). Previously it was found by Bauchau, et al. [34] that regular beam elements that accurately predicts the overall torsional stiffness of the MBB blade with cruciform flexbeam at zero rotational speed, significantly under-predicts the torsional stiffness at nominal rotor speed. To solve this problem the use of non-linear shell elements to model open composite sections like this cruciform was proposed in [34].

The physical dimensions of the cruciform section are not given by [33], but it could be approximately determined from the supplied bending stiffness distribution graphs, a scale drawing of the section and published properties of the material. The width and height of the cruciform were therefore scaled as 27.5 *mm* and 36 *mm*,

Longitudinal modulus of elasticity	E_L	$38.6 \times 10^9\ N/m^2$
Transverse modulus of elasticity	E_T	$8.27 \times 10^9\ N/m^2$
Shearing modulus	G_{LT}	$4.14 \times 10^9\ N/m^2$
Poisson's ratio	ν_{LT}	0.26

Table 5.19: MBB cruciform flexbeam: material properties

respectively. The rotor radius is given by [33] as 975 *mm*, while the length of the different components in the spanwise direction could also be determined approximately, from the given stiffness graphs. The cruciform flexbeam is about 228 *mm* long, extending from approximately the 72 *mm* to the 300 *mm* radial positions.

An analysis was performed on the cruciform section with the sectional analysis program, using the mesh indicated in figure 5.12. This model consists of 248 eight noded quadrilateral and six noded triangular elements, with 861 nodes and a total of 2583 degrees of freedom. In the analysis the properties of SCOTCHPLY 1002 glass/epoxy was used, as given in table 5.19. The intersection of the beam reference line with the plane of the section was chosen at the geometric center of the section. Since no material or geometric couplings exists, for this choice and the orientation of the $\vec{e}_2$ and $\vec{e}_3$ directions, the sectional stiffness tensor is diagonal and the sectional shear center and axial stiffness centroid lie on the reference line. The diagonal of the calculated sectional stiffness tensor is given in table 5.20. The success of the scaling of the sectional dimensions can partially be judged by comparing the two bending stiffnesses as calculated by the analysis with the target values from the graphs in [33], also included in the table.

The intrinsic characteristic warpings are shown (exaggerated) in figures 5.13 to 5.18, with the undeformed section indicated in broken lines. As noted before,

	Sectional Analysis	Graphs in [33]
Axial stiffness	1.163×10^7 N	
Transverse shear stiffness, with respect to $\vec{e}_1$ and $\vec{e}_2$	1.261×10^6 N	
Transverse shear stiffness, with respect to $\vec{e}_1$ and $\vec{e}_3$	1.015×10^6 N	
Torsional stiffness	11.48 $N{\cdot}m^2$	
Bending stiffness, about $\vec{e}_2$	444.0 $N{\cdot}m^2$	437 $N{\cdot}m^2$
Bending stiffness, about $\vec{e}_3$	960.6 $N{\cdot}m^2$	1100 $N{\cdot}m^2$

Table 5.20: MBB cruciform flexbeam: Cross sectional stiffness characteristics

the intrinsic characteristic warpings associated with axial force and bending are strictly in-plane, and those associated with transverse shear and torsion are strictly out-of-plane, due to the fact that no coupling exists. The intrinsic characteristic warping associated with torsional loading is especially significant: it clearly shows the torsional softening effect of the slots in the four arms of the cruciform. In providing these slots, section is allowed to warp more than what would have been the case otherwise, thereby reducing the torsional stiffness.

Next, the whole blade was analyzed with the multi-body analysis program. Once again two models of the blade was made, one employing only regular beam elements, and the second with advanced beam elements on the cruciform flexbeam portion of the blade and regular elements everywhere else. In both cases the blade was modeled with six cubic elements, employing three point Gaussian quadrature: one element for the "flap hinge", three for the cruciform flexbeam and two for the airfoil portion of the blade. For all advanced beam elements the modal basis

consists of the six intrinsic characteristic warping functions. The beam element mesh is shown in figure 5.19, where inter-element nodes are indicated with dots and internal nodes with asterisk symbols. The boundary conditions imposed were those of a cantilevered beam at the root of the "flap hinge" beam, at the radial position 23 *mm*. The whole system is allowed to rotate about the rotor axis of rotation, at the zero radial position. The nominal rotor speed is 211.8 *rad/s*. The natural frequencies and vibration modes of the blade were calculated at 20% intervals from 0 to 120% nominal rotor speed. The results obtained with the regular beam element are shown in figure 5.20, for the first four vibration modes. At nominal rotor speed, the natural frequency of the first lead-lag and flapping modes were calculated as 0.764 and 1.049 per revolution, respectively, compared to the values quoted in [33] of 0.685 and 1.043 per revolution, respectively. (Unfortunately no other natural frequencies were given in [33].)

Three different configurations were studied with the model with advanced beam elements on the cruciform flexbeam: (1) free warping everywhere, but accounting for the non-linear strain effect (labeled "regular beam element with trapeze effect" on the graphs), (2) the same as (1), but also constraining all warping at the outboard end of the cruciform flexbeam (labeled "advanced beam element with constraints on all modes at the outboard side only"), and (3) the same as (1) but constraining all warping at both inboard and outboard ends of the cruciform flexbeam (labeled as "advanced beam element with constraints on all modes at both in– and the outboard sides"). The results calculated for these three configurations and the regular beam element model are compared in figures 5.21 to 5.24. Very good agreement is found between the four configurations with respect to the natural frequencies of the first and second flapping modes (figures 5.21 and 5.22). The first lead-lag mode natural frequency is predicted slightly higher across the whole speed range in the case of the constrained warping on both sides, as compared to the

other three configurations, which are in fair agreement (figure 5.23). With respect to the first torsional mode natural frequency, the four configurations render wide ranging results (figure 5.24). The regular element model predicts frequencies which are known to be too low, as pointed out by [34]. Adding the non-linear strain effect modeling to this, increases the calculated natural frequency at operating speed by 7.6%. Adding to this the modeling of constrained warping on the outboard side only, increases the calculated natural frequency by an additional 2.1%, while adding the inboard constraint as well further raises this frequency by 2.4%. This means that the model with constraints on all modes at both the in- and outboard sides and with the non-linear strain effect taken into account predicts a torsional natural frequency 12.1% higher than the model with regular beam elements.

The overall torsional stiffness of the blade, as indicated by the tip rotation under an applied tip torque, was calculated at zero speed and at nominal operating speed, for all four configurations discussed above, and are listed in table 5.21, together with corresponding values given in [33]. The calculated values are much higher than the quoted values. This discrepancy can be explained by realizing that no torsional stiffness data other than these two values were given by [33], which means that a sectional torsional stiffness had to be selected almost at random for the airfoil portion of the blade. This was selected to be significantly higher than the sectional torsional stiffness of the cruciform flexbeam. Also, there is some uncertainty about the interpretation of the two values given by [33]. What is important, though, is the trend which these two values represent: they indicate a 52% increase in torsional stiffness when the rotor speeds up from rest to operating speed. The corresponding increase calculated with the regular beam elements is 37% only, an increase ascribed to an inertial effect, the so-called tennis racket effect. The other main contributor to the torsional stiffening of the blade as it speeds up is the non-linear strain effect, and all three the configurations which included the modeling of

Cruciform flexbeam configuration	Torsional stiffness ($N{\cdot}m/deg.$)		Percentage change
	0% speed	100% speed	
Regular Beam Element	0.686	0.941	37
Regular Beam Element with Trapeze Effect	0.686	1.086	58
Advanced Beam Element with constraints on all modes at the outboard side only	0.730	1.130	54
Advanced Beam Element with constraints on all modes at both the in- and outboard sides	0.780	1.177	51
Values from [33]	0.33	0.5	52

Table 5.21: MBB cruciform flexbeam: Comparison of blade torsional stiffness values

this effect showed percentage increases much closer to the value reported by [33]. Of these, the result of the configuration with constrained warping on both sides is the closest to the [33] result.

5.4 Conclusion

This chapter demonstrated the use of the three dimensional Saint-Venant beam theory to determine beam sectional stiffness properties for regular beam elements used in finite element multi-body dynamic analyses. It also explained how the implementation of this theory has been validated. The presented examples, in particular the ONERA experimental blade example, powerfully illustrate an important advantage of the semi-discretization method: the sectional modeling can be performed to high levels of detail, without impacting negatively on the size of the multi-body dynamic analysis model.

Some numerical examples to validate and demonstrate the advanced beam theory were presented, and it was shown that the beam element based on this theory has great potential in modeling modern helicopter blades and blade-hub attachments. It was also pointed out that further validation of the advanced beam element is required.

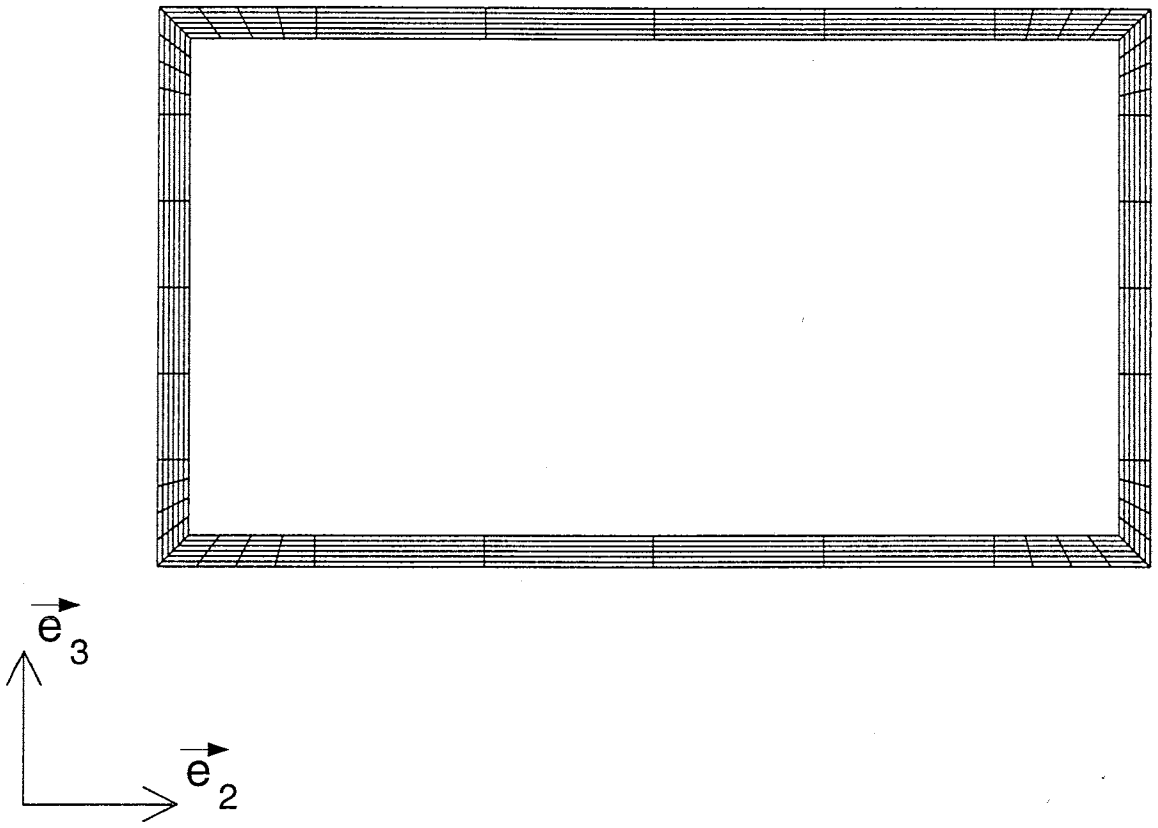

Figure 5.1: Hollow rectangular section 1: Finite element mesh of section

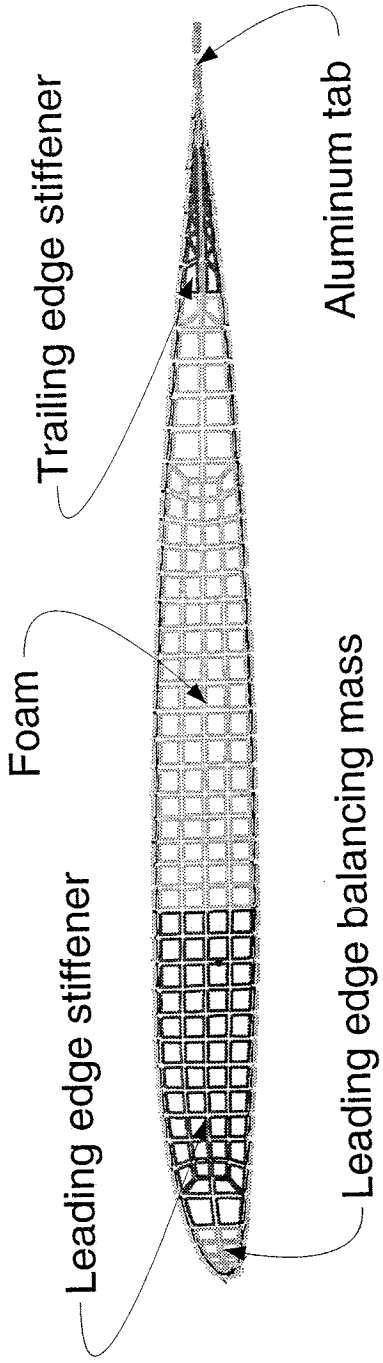

Figure 5.2: ONERA section: Finite element mesh of section

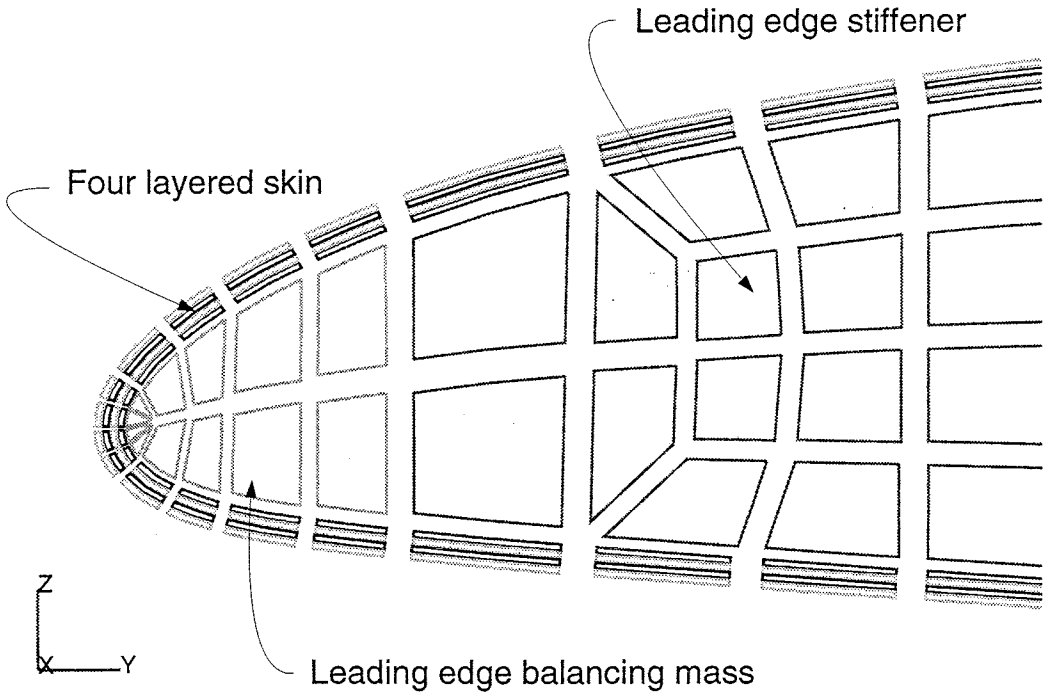

Figure 5.3: ONERA section: Detail of leading edge finite element mesh

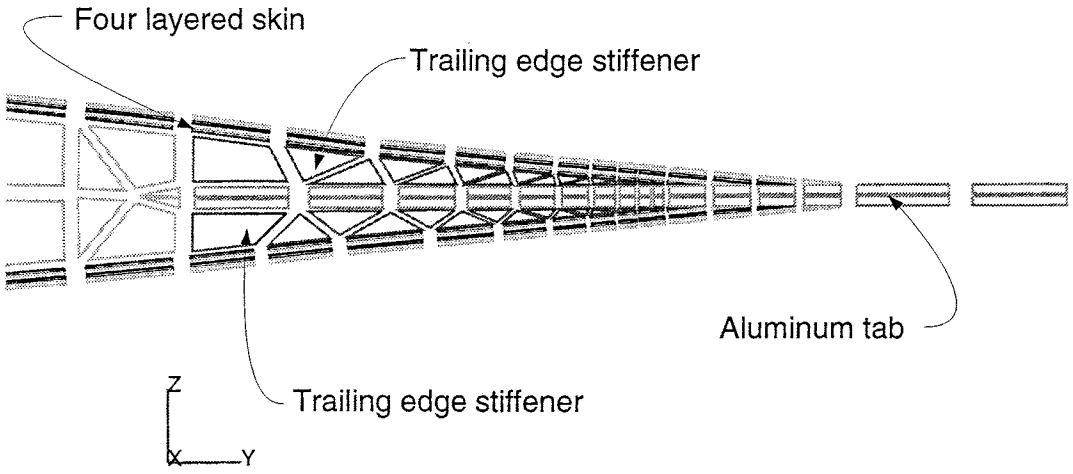

Figure 5.4: ONERA section: Detail of trailing edge finite element mesh

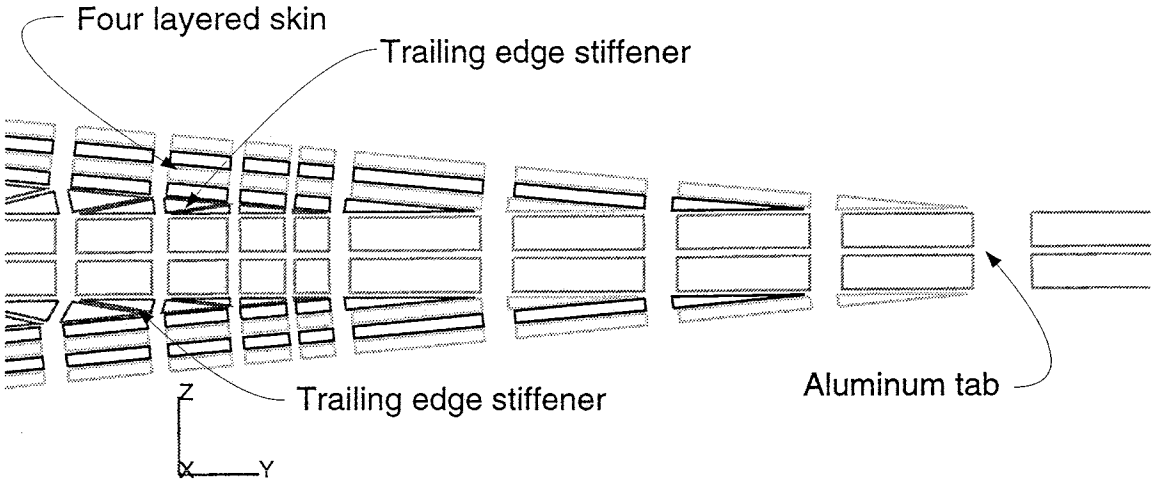

Figure 5.5: ONERA section: Refined detail of trailing edge finite element mesh, showing the connection between the aluminum tab and the four layered composite skin

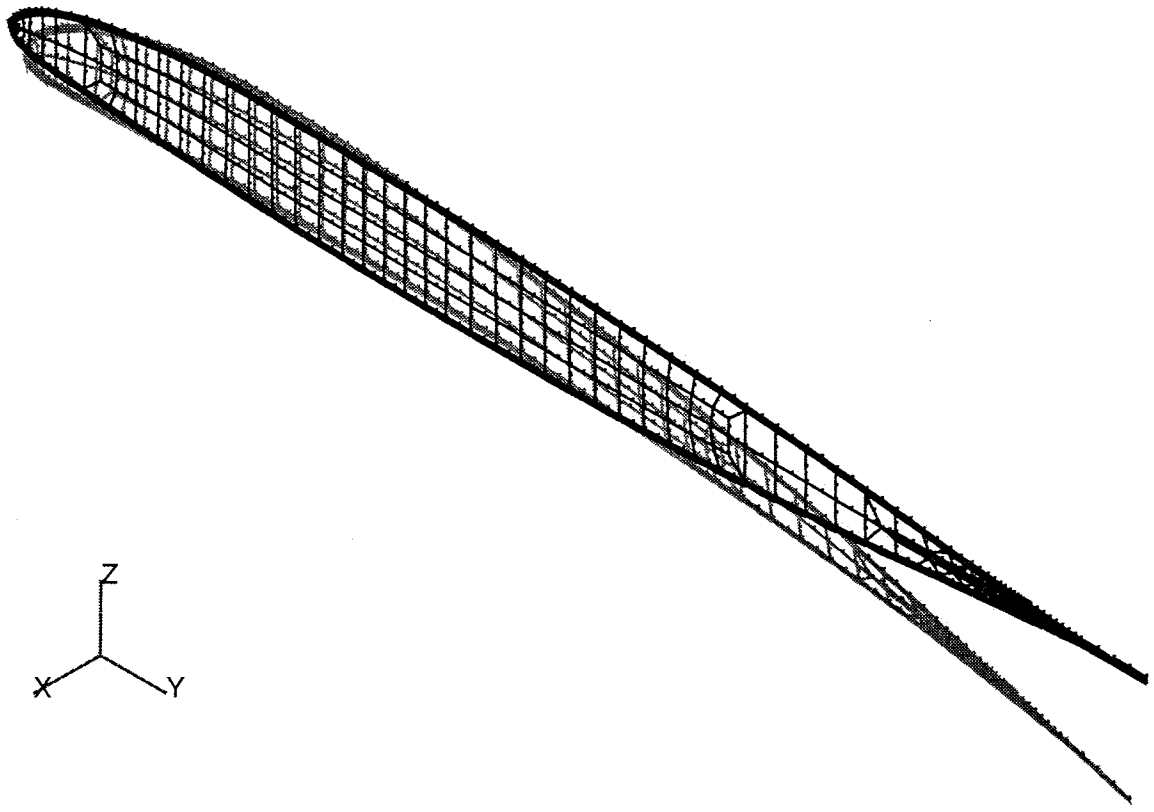

Figure 5.6: ONERA section: Characteristic warping associated with an axial force

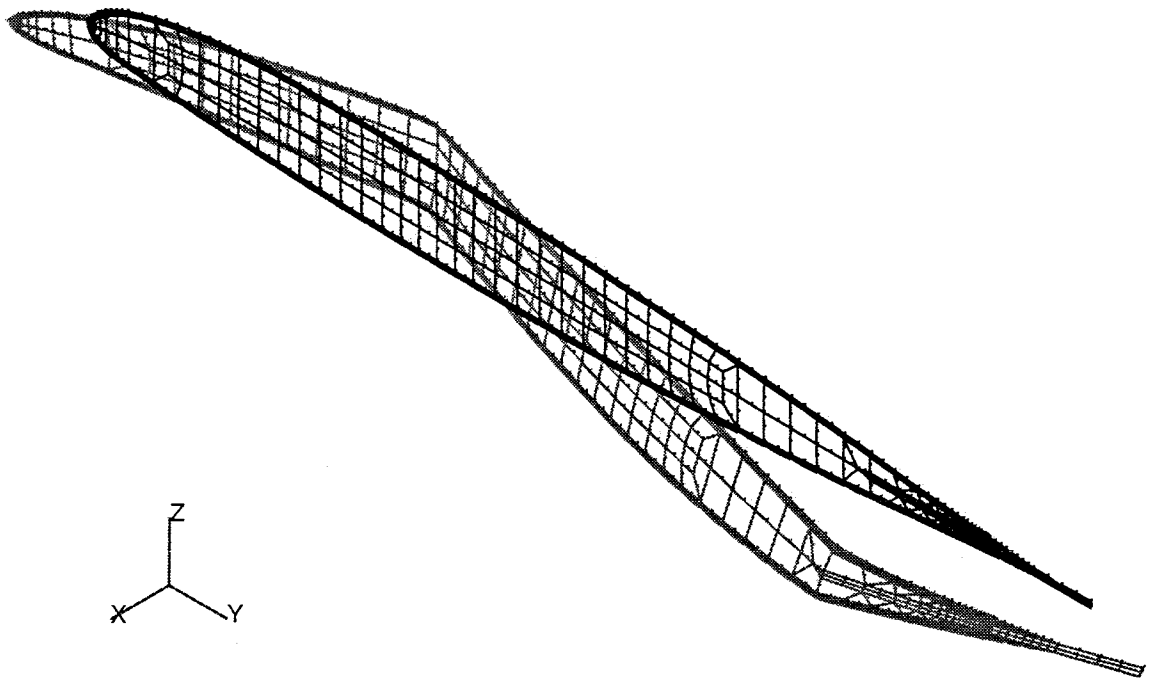

Figure 5.7: ONERA section: Characteristic warping associated with a transverse shear force in the $\vec{e}_2$ (or Y) direction

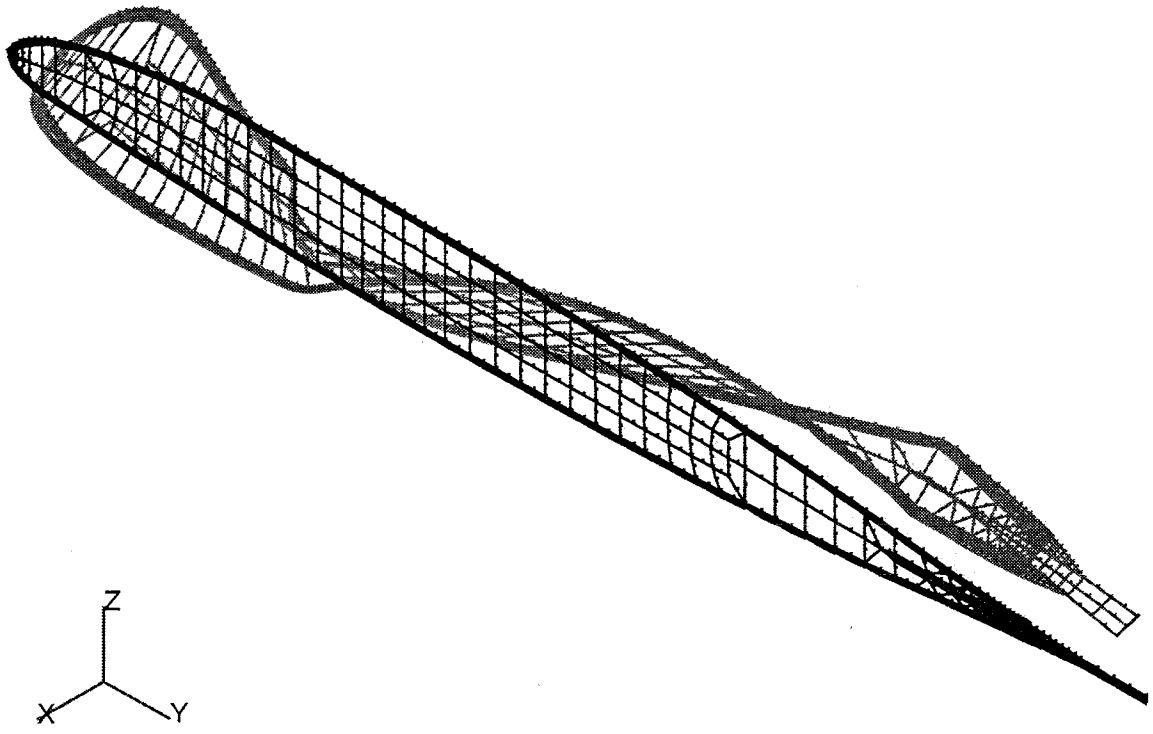

Figure 5.8: ONERA section: Characteristic warping associated with a transverse shear force in the $\vec{e}_3$ (or Z) direction

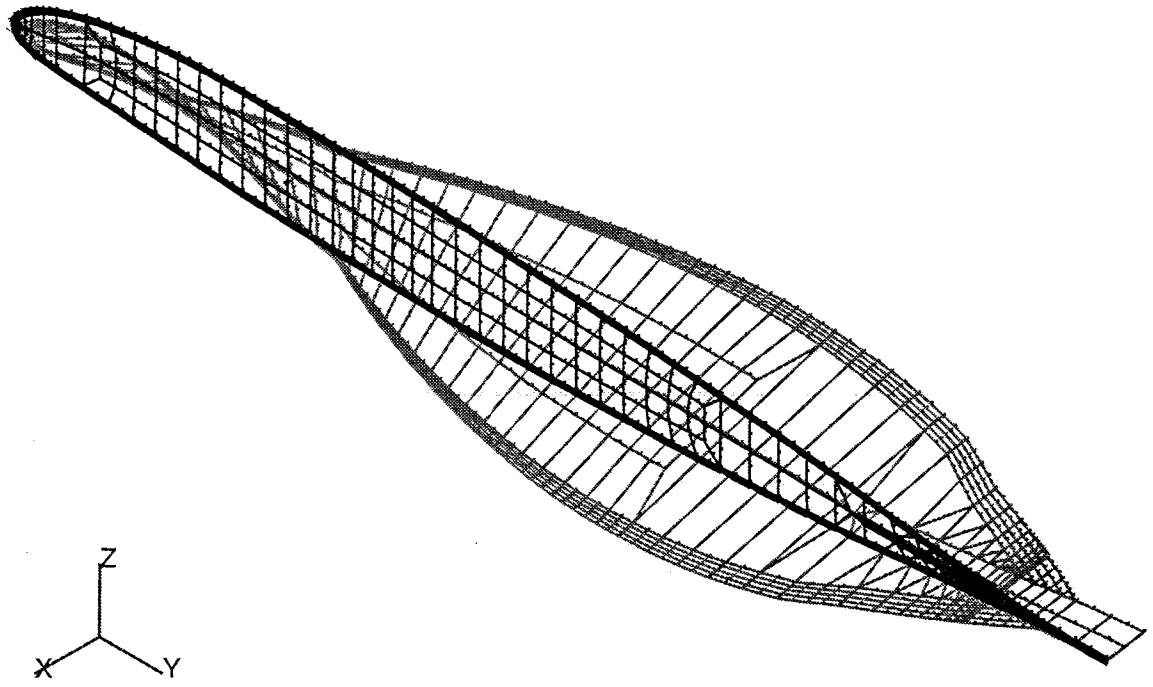

Figure 5.9: ONERA section: Characteristic warping associated with a torsional moment

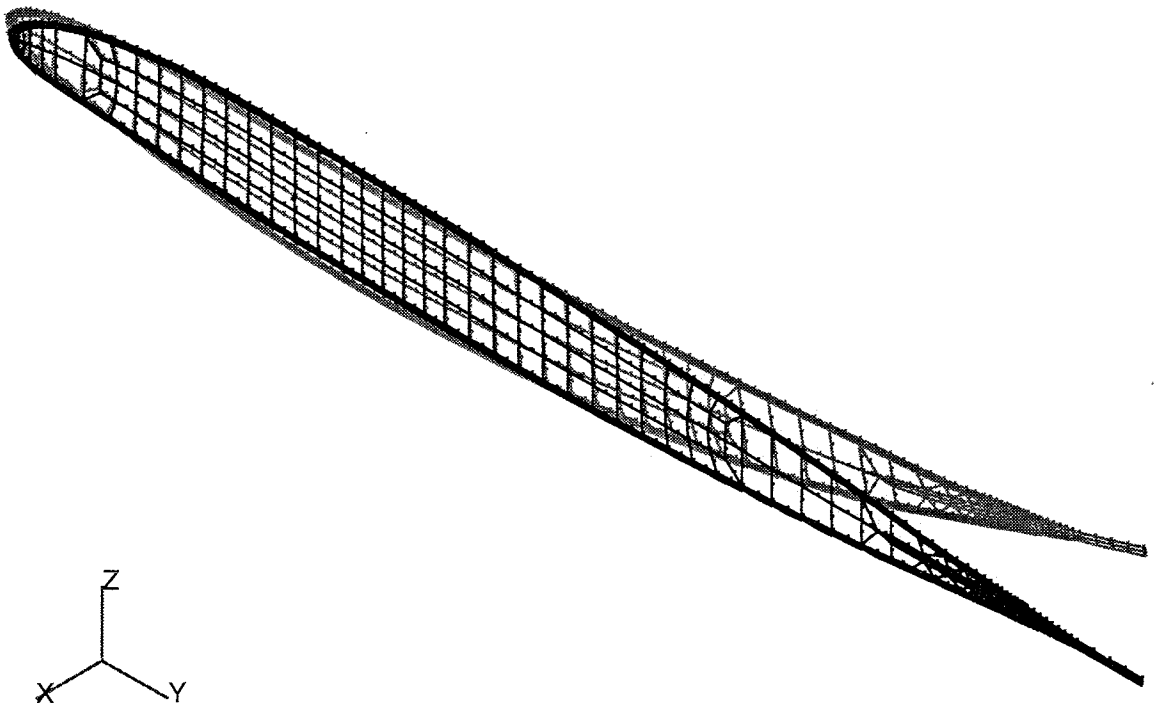

Figure 5.10: ONERA section: Characteristic warping associated with a bending moment about the $\vec{e}_2$ (or Y) axis

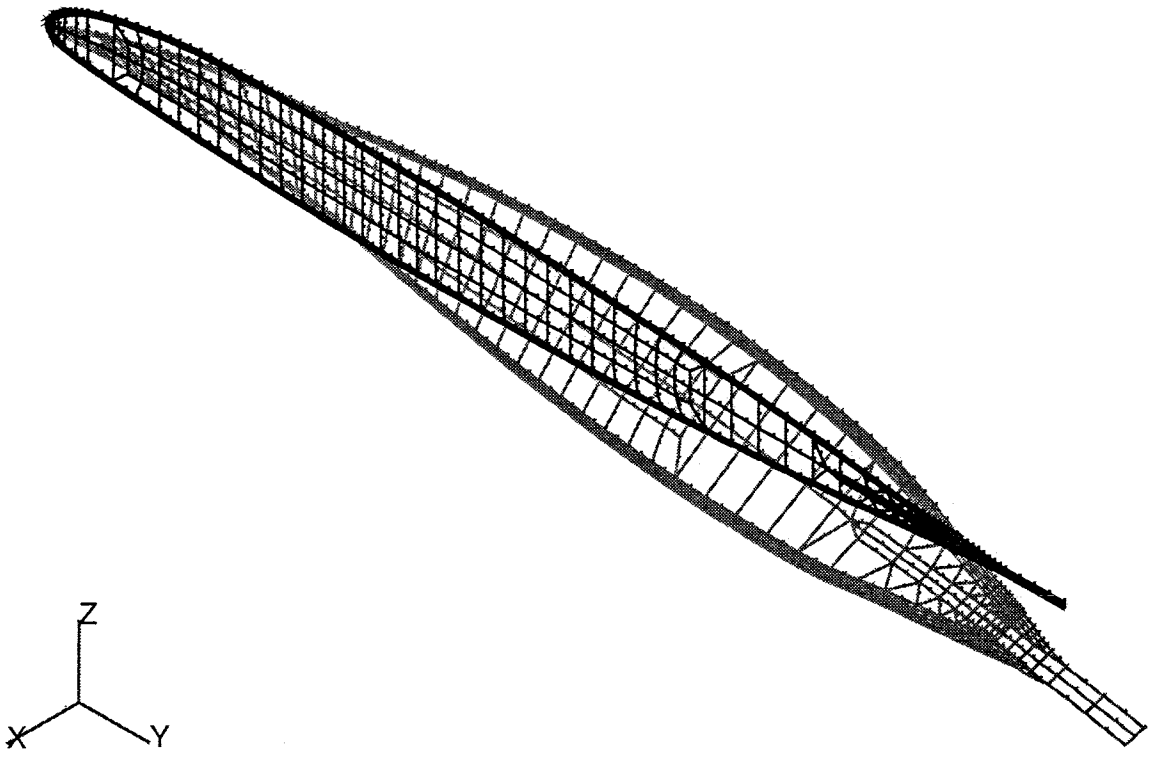

Figure 5.11: ONERA section: Characteristic warping associated with a bending moment about the $\vec{e}_3$ (or Z) axis

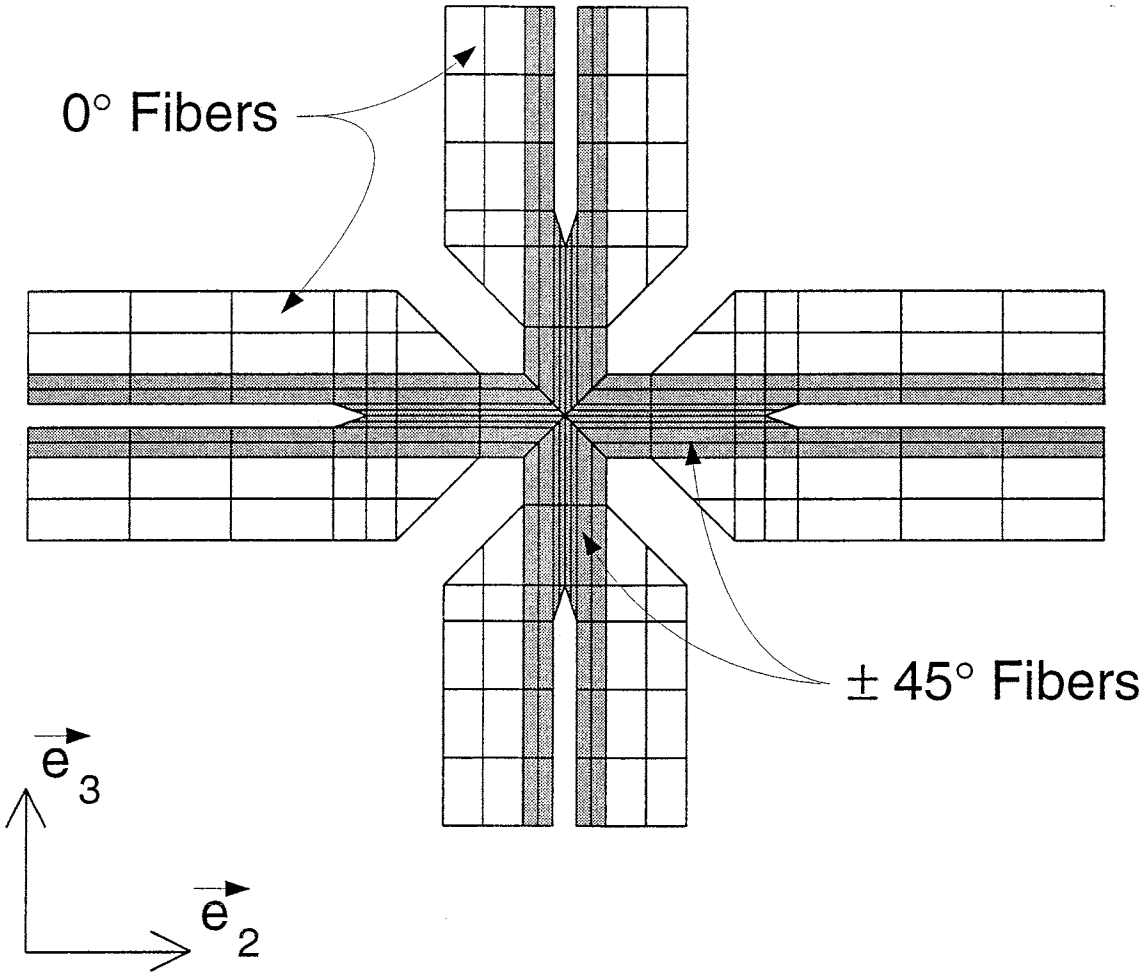

Figure 5.12: MBB cruciform flexbeam: Finite element mesh of section

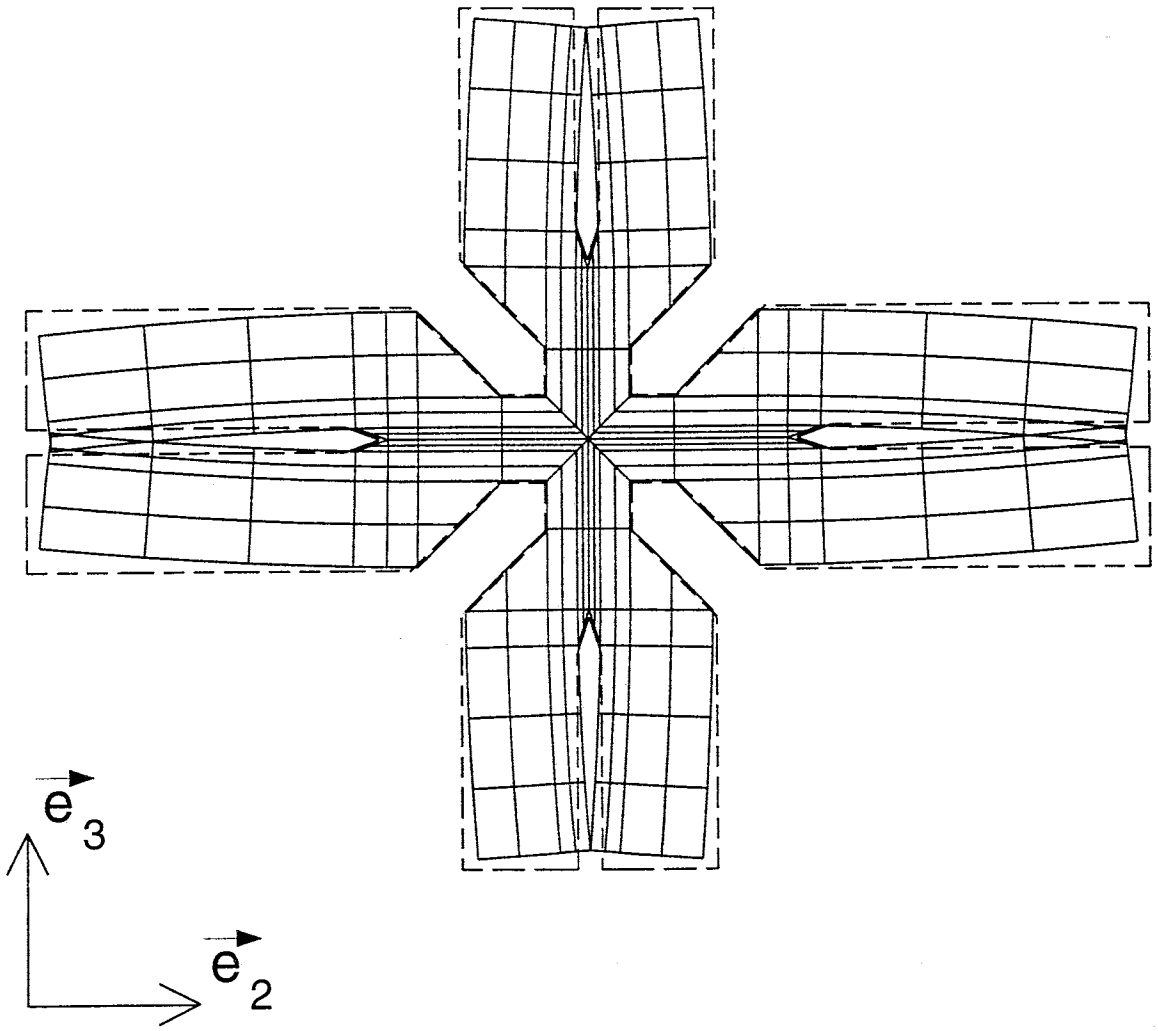

Figure 5.13: MBB cruciform flexbeam: Characteristic warping associated with an axial force

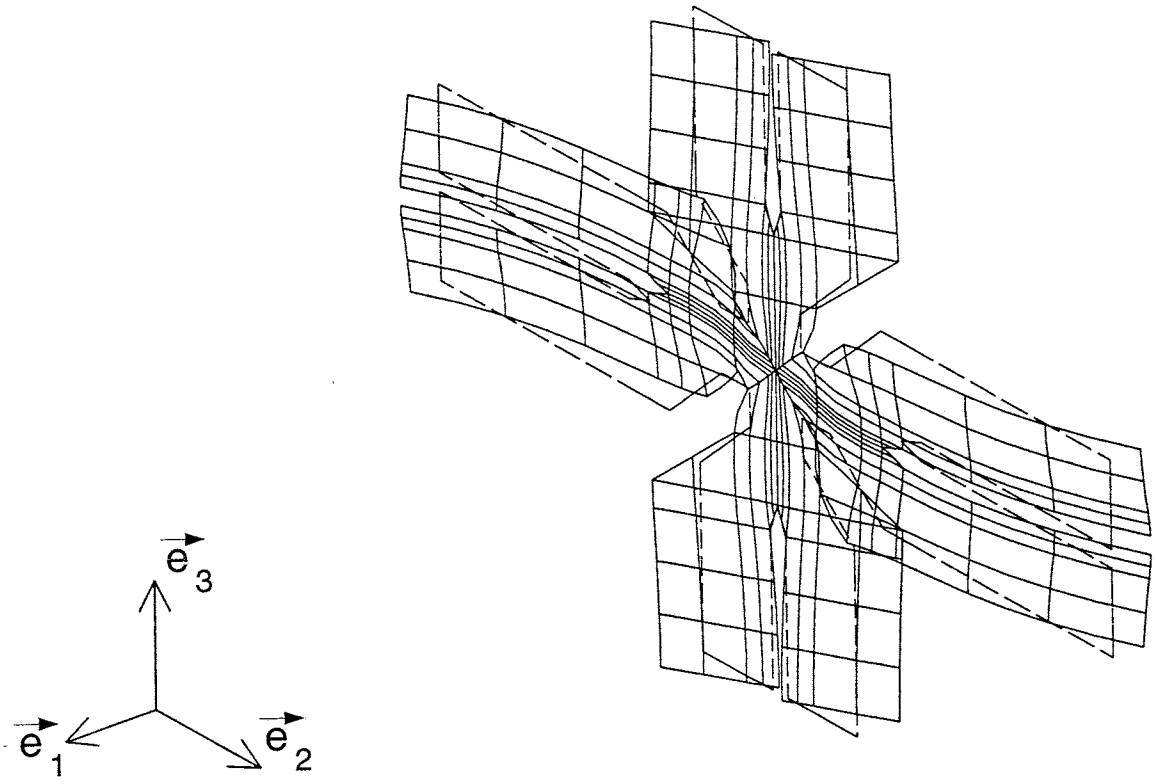

Figure 5.14: MBB cruciform flexbeam: Characteristic warping associated with a transverse shear force in the $\vec{e}_2$ direction

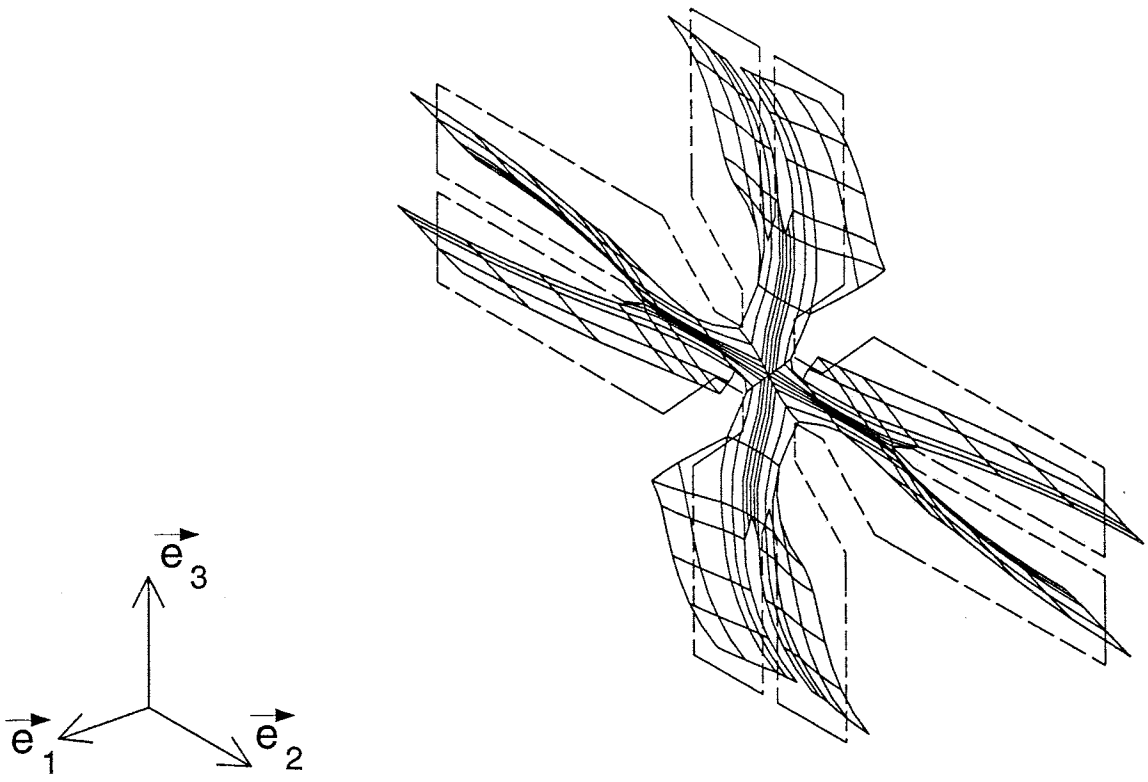

Figure 5.15: MBB cruciform flexbeam: Characteristic warping associated with a transverse shear force in the $\vec{e}_3$ direction

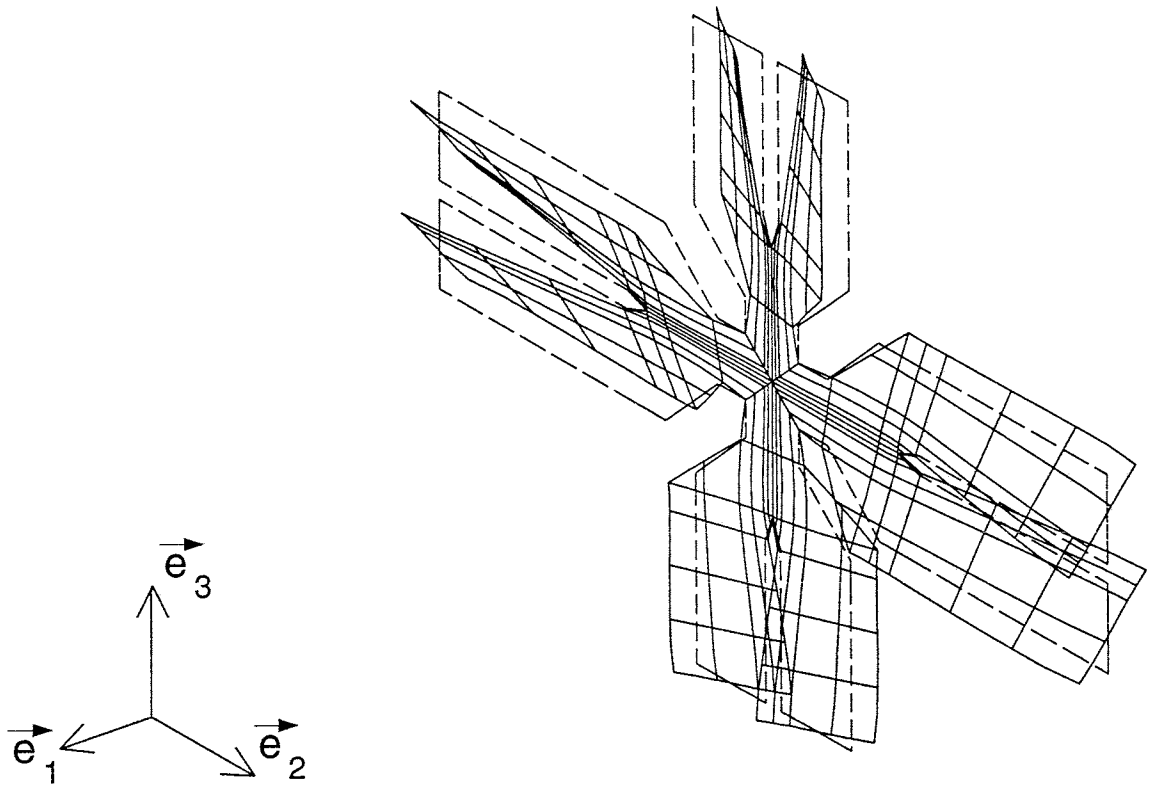

Figure 5.16: MBB cruciform flexbeam: Characteristic warping associated with a torsional moment

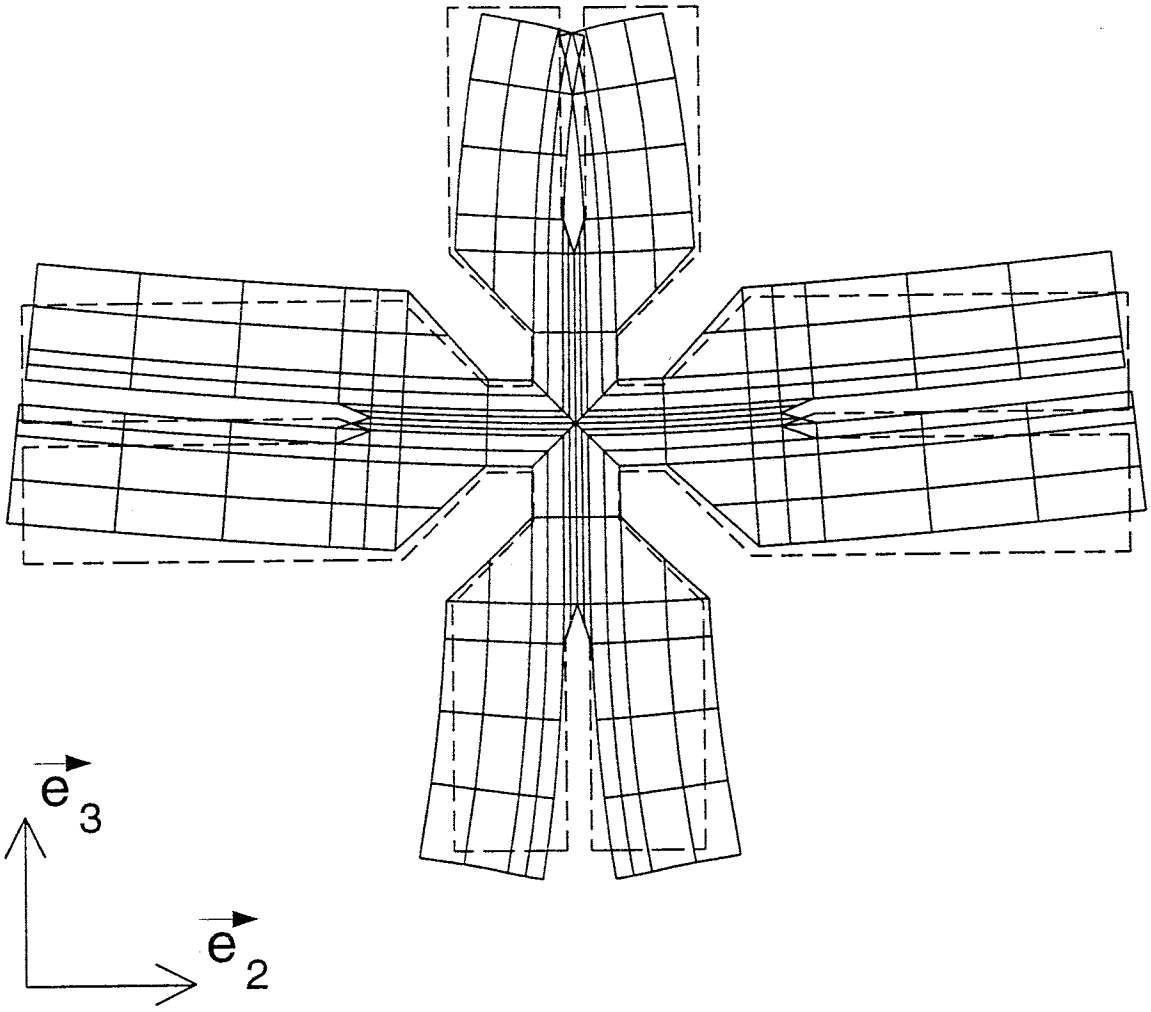

Figure 5.17: MBB cruciform flexbeam: Characteristic warping associated with a bending moment about the $\vec{e}_2$ axis

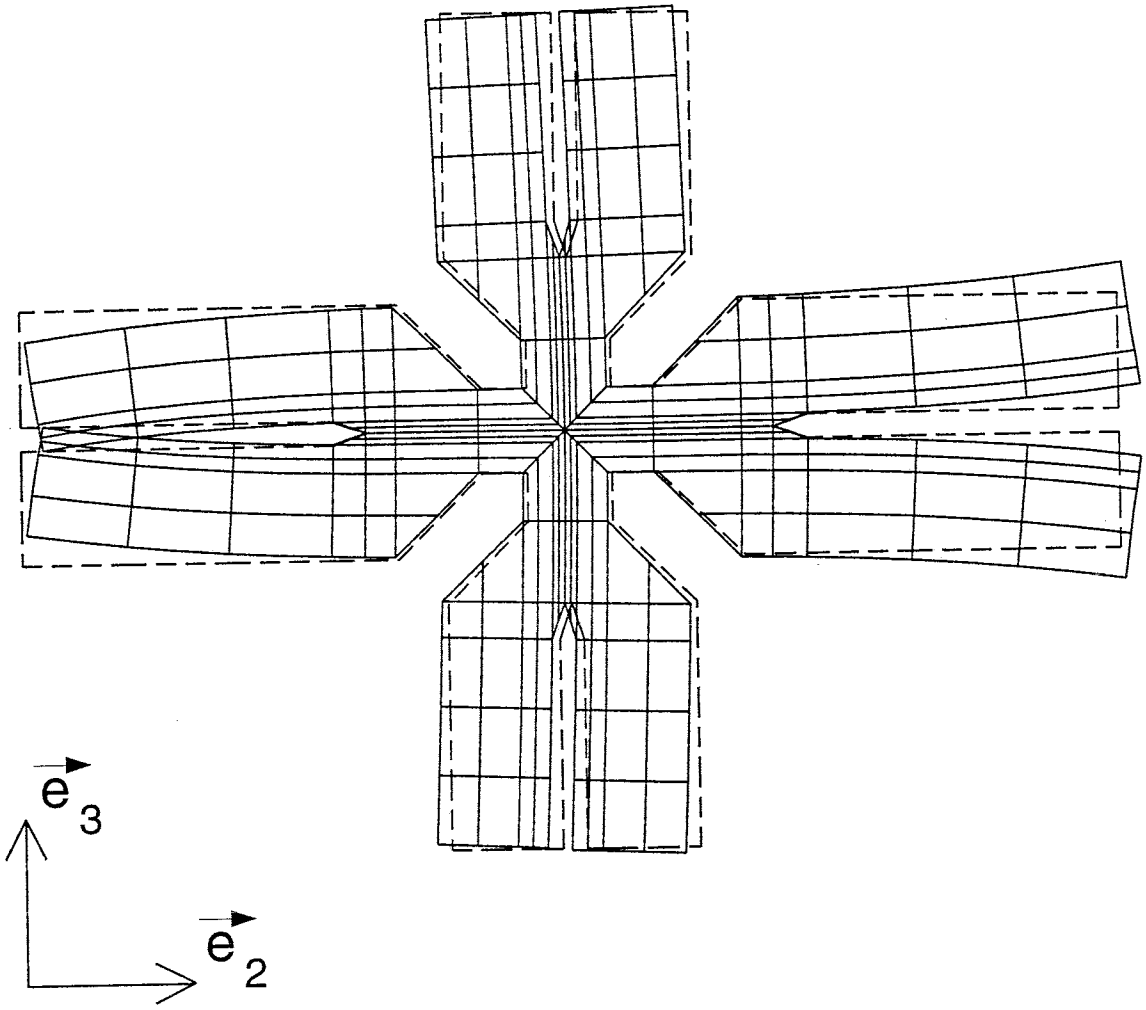

Figure 5.18: MBB cruciform flexbeam: Characteristic warping associated with a bending moment about the $\vec{e}_3$ axis

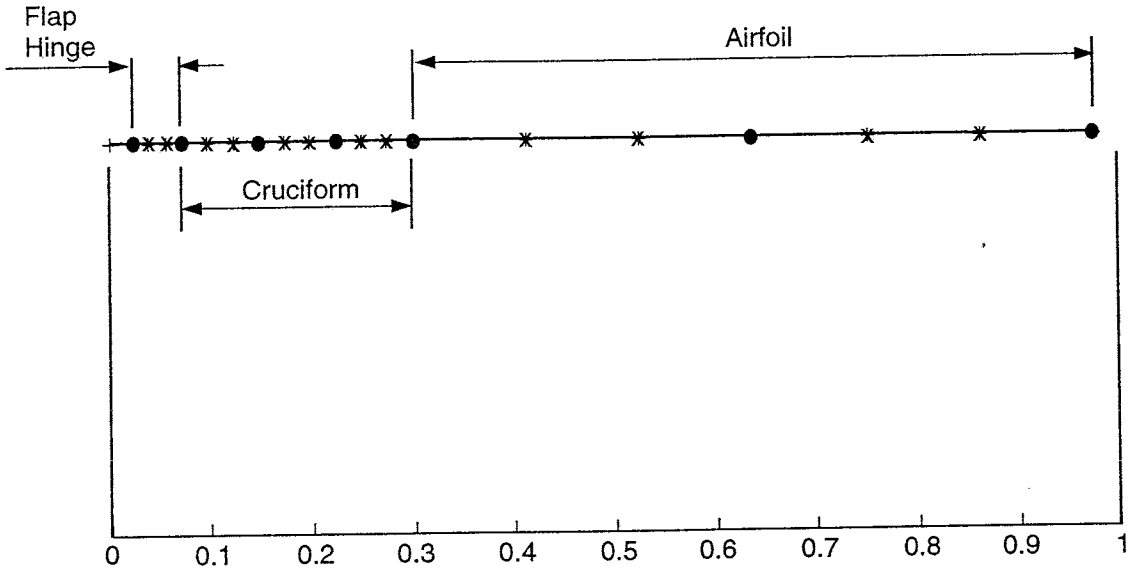

Figure 5.19: MBB tail rotor blade with cruciform flexbeam: finite element mesh of blade

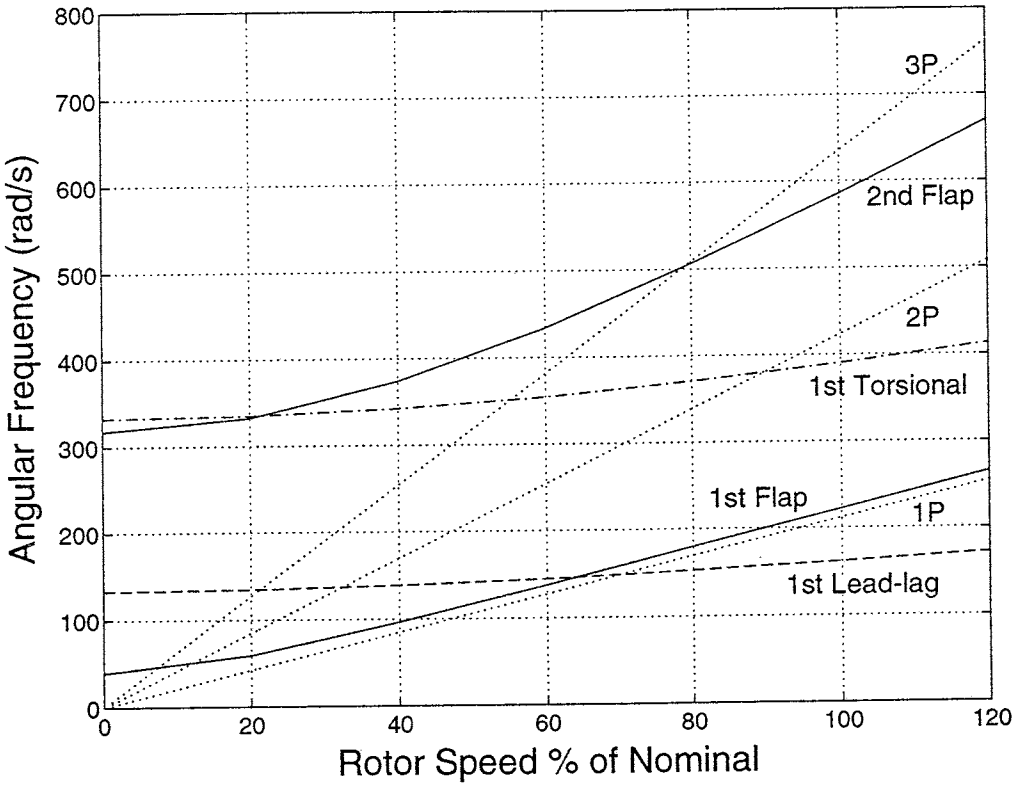

Figure 5.20: MBB tail rotor blade with cruciform flexbeam: fan plot of natural angular frequency as a function of rotor speed, for the case where the flexbeam portion is modeled with regular beam elements

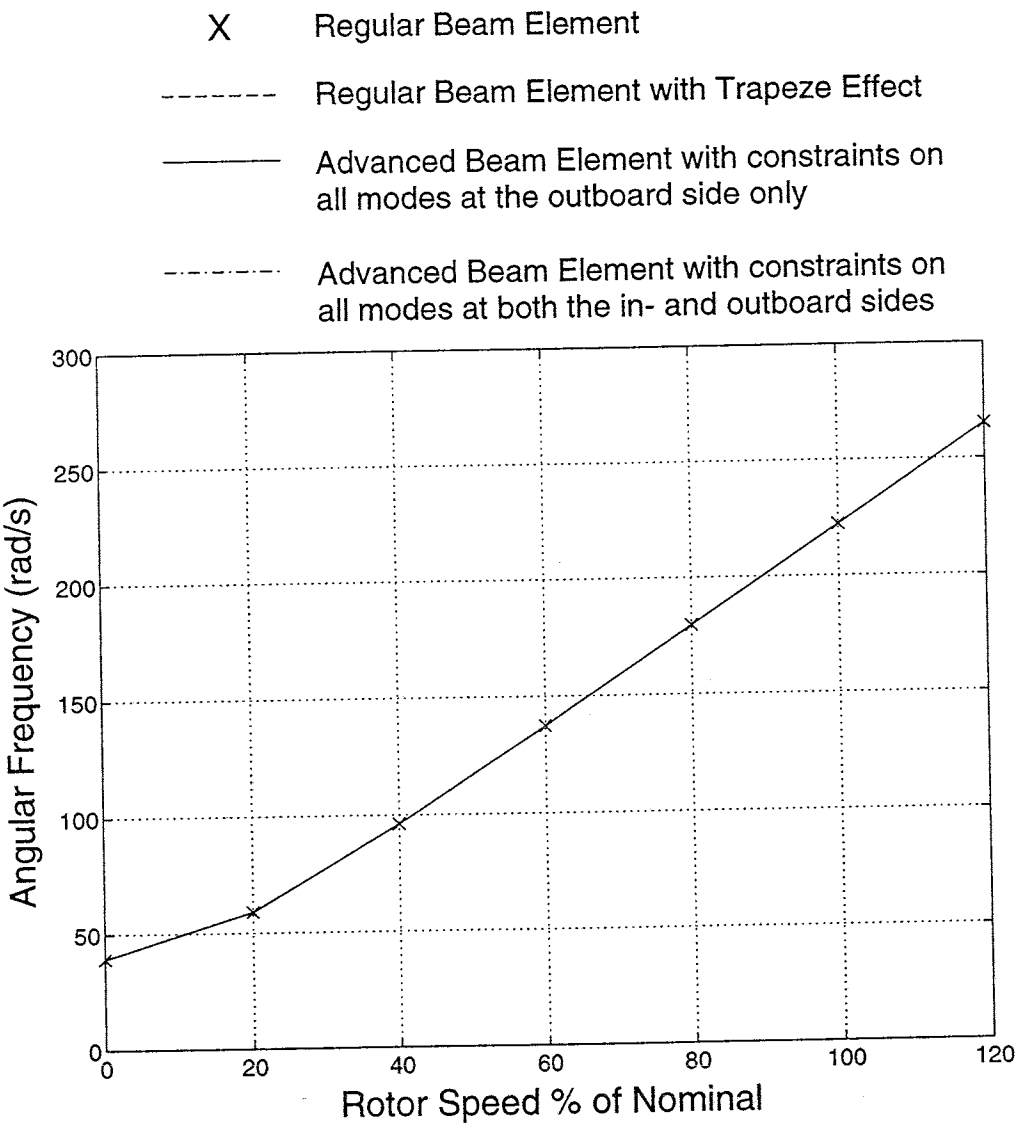

Figure 5.21: MBB tail rotor blade with cruciform flexbeam: natural angular frequency of the 1st flapping mode as a function of rotor speed

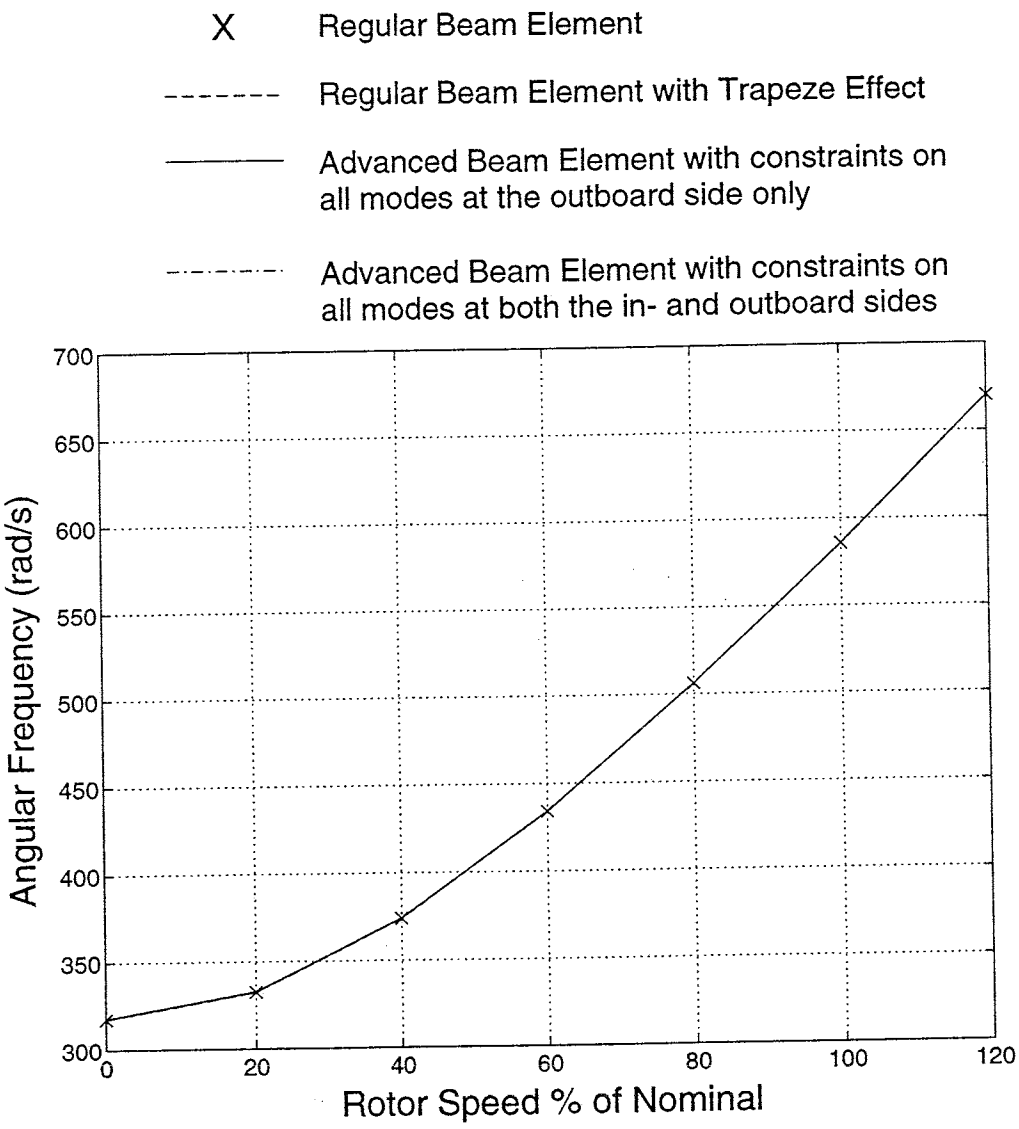

Figure 5.22: MBB tail rotor blade with cruciform flexbeam: natural angular frequency of the 2nd flapping mode as a function of rotor speed

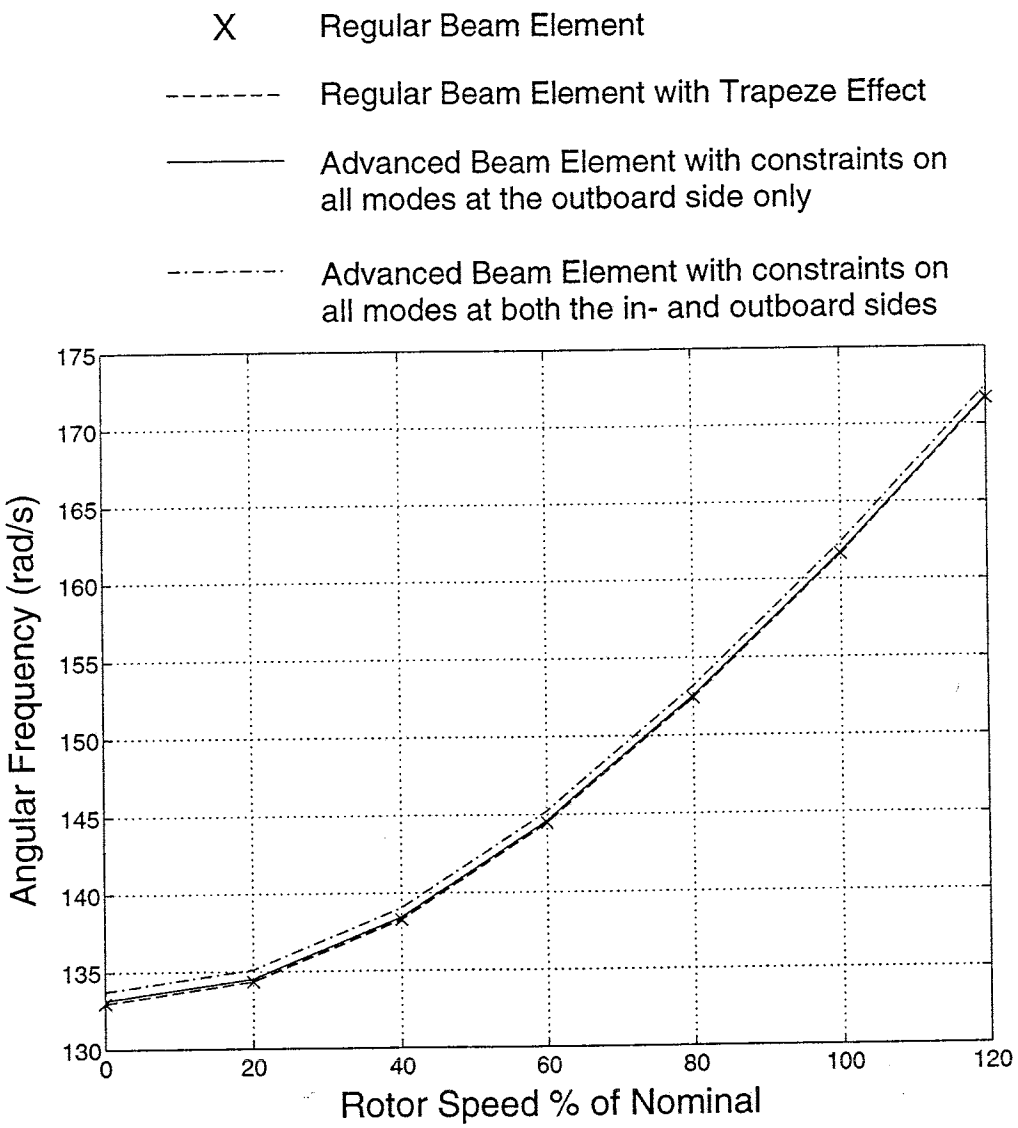

Figure 5.23: MBB tail rotor blade with cruciform flexbeam: natural angular frequency of the 1st lead-lag mode as a function of rotor speed

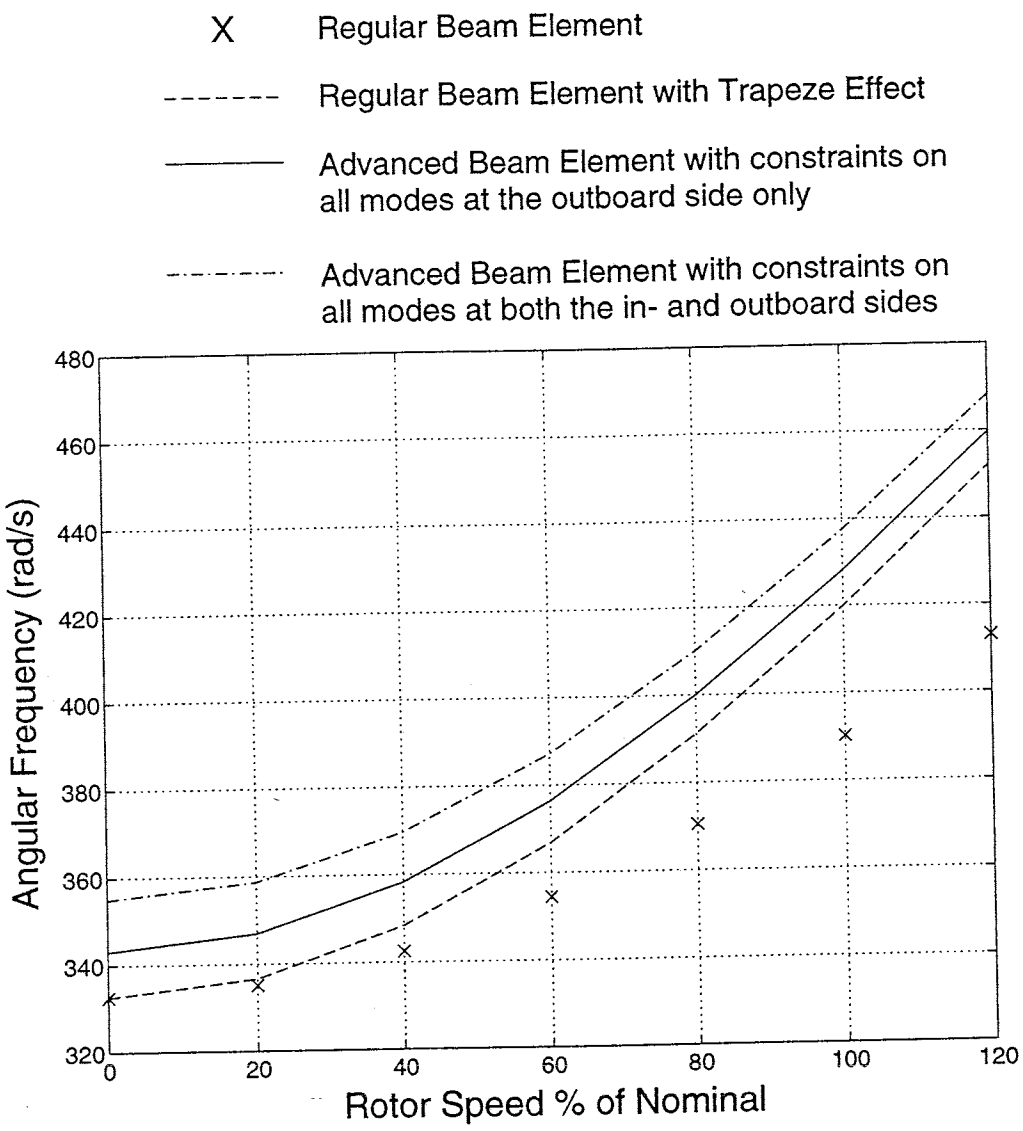

Figure 5.24: MBB tail rotor blade with cruciform flexbeam: natural angular frequency of the 1st torsional mode as a function of rotor speed

CHAPTER 6
ENERGY PRESERVING SCHEME FOR THE TIME INTEGRATION OF BEAM EQUATIONS OF MOTION

6.1 Introduction

The energy preserving scheme was derived to fill the need for a time integration scheme for non-linear analysis of multi-body dynamic systems, with guaranteed unconditional stability. Previously, the HHT scheme [17] or the generalized-α method [19] has been used to perform this type of integration, however, the stability of these schemes can be proven for linear systems only. The unconditional stability of the energy preserving scheme stems from a proof of preservation of the total energy of the system.

This chapter describes the energy preserving scheme for integrating the equations of motion of a non-linear beam. This serves as an example for the derivation of similar schemes for other types of elastic bodies. In order to arrive at the energy preserving scheme, a basic way of discretizing finite rotations and the beam equations of motion are given in sections 6.2 and 6.3, respectively. The latter section also presents a fundamental and very useful work expression resulting from this basic discretization. The two basic discretizations given in this chapter also pertain to the energy decaying method and are therefore used again in chapter 7. Finally, the energy preserving scheme is presented in section 6.4. This section also shows that this scheme is unconditionally stable, due to the preservation of the total energy in the beam.

6.2 Discretization of the finite rotations.

Consider an initial time t_i, a final time t_f and a mid-point time $t_h = (t_i + t_f)/2$ and the corresponding triads $\mathcal{S}_i$, $\mathcal{S}_f$ and $\mathcal{S}_h$, respectively. The rotation matrices associated with those triads are R_i, R_f, and R_h, respectively, all measured in $\mathcal{S}$. $R(\underline{c})$ is the rotation matrix from $\mathcal{S}_i$ to $\mathcal{S}_f$, measured in $\mathcal{S}$. For the purposes of this work, the rotation matrix R is expressed in terms of the components of the conformal rotation vector $\underline{c}$, defined in Appendix A. The mid-point triad $\mathcal{S}_h$ is defined so that the rotation from $\mathcal{S}_i$ to $\mathcal{S}_h$ and $\mathcal{S}_h$ to $\mathcal{S}_f$ are equal. Let G be that rotation, measured in $\mathcal{S}$. Let G^* and R^* be the corresponding rotation matrices measured in $\mathcal{S}_h$. The following relationships are readily derived:

$$\begin{aligned} G &= R_h R_i^T \;; \qquad G^* = R_0^T R_i^T R_h R_0 \;; \\ G &= R_f R_h^T \;; \qquad G^* = R_0^T R_h^T R_f R_0 \;; \\ R &= R_f R_i^T \;; \qquad R^* = R_0^T R_h^T R_f R_0 R_o^T R_i^T R_h R_0 \;; \end{aligned} \tag{6.1}$$

and:

$$\begin{aligned} R_f R_0 &= R_h R_0 G^* = R_i R_0 R^* \;; \\ R_h R_o &= R_i R_o G^* = R_f R_o G^{*T} \;; \\ R_i R_o &= R_h R_o G^{*T} = R_f R_o R^{*T} \;. \end{aligned} \tag{6.2}$$

Finally, the following notations are introduced:

$$\mathcal{R}_i = \begin{bmatrix} R_i R_0 & 0 \\ 0 & R_i R_0 \end{bmatrix} \;; \quad \mathcal{R}_f = \begin{bmatrix} R_f R_0 & 0 \\ 0 & R_f R_0 \end{bmatrix} , \tag{6.3}$$

and

$$\mathcal{G}_h = \frac{2 R_h R_0}{4 - c_0} \;; \quad \mathcal{H}_h = \frac{R_f R_0 + R_i R_0}{2} , \tag{6.4}$$

c_0 being defined in Appendix A.

6.3 Basic discretization of the equations of motion of a beam.

Consider the following discretization of the beam equations of motion (2.11):

$$\frac{\mathcal{R}_f \underline{p}_f^* - \mathcal{R}_i \underline{p}_i^*}{\Delta t} + \mathcal{U}\left[\frac{\widetilde{u_f} - \widetilde{u_i}}{\Delta t}\mathcal{G}_h\right]\frac{\underline{p}_i^* + \underline{p}_f^*}{2} - \left(\mathcal{Q}_h \underline{g}_h^*\right)' - \mathcal{U}\left[\frac{2}{c_0}\left(\widetilde{u_0'} + \widetilde{u_h'}\right)\right]\mathcal{Q}_h \underline{g}_h^* = \underline{q}_h \,, \tag{6.5}$$

where

$$\mathcal{Q}_h = \begin{bmatrix} \mathcal{H}_h & 0 \\ 0 & \mathcal{G}_h \end{bmatrix},$$

the midpoint displacement is defined as $\underline{u}_h = (\underline{u}_i + \underline{u}_f)/2$, and the elastic forces $\underline{g}_h^*$ will be determined later.

Premultiplying these discretized equations by $\begin{bmatrix} \frac{\underline{u}_f^T - \underline{u}_i^T}{\Delta t} & \frac{\underline{c}^T}{\Delta t} \end{bmatrix}$ and integrating over the span of the beam yields:

$$\int_0^L \begin{bmatrix} \frac{\underline{u}_f^T - \underline{u}_i^T}{\Delta t} & \frac{\underline{c}^T}{\Delta t} \end{bmatrix} \left[\frac{\mathcal{R}_f \underline{p}_f^* - \mathcal{R}_i \underline{p}_i^*}{\Delta t} + \mathcal{U}\left[\frac{\widetilde{u_f} - \widetilde{u_i}}{\Delta t}\mathcal{G}_h\right]\frac{\underline{p}_i^* + \underline{p}_f^*}{2} - \left(\mathcal{Q}_h \underline{g}_h^*\right)' - \mathcal{U}\left[\frac{2}{c_0}\left(\widetilde{u_0'} + \widetilde{u_h'}\right)\right]\mathcal{Q}_h \underline{g}_h^* - \underline{q}_h\right] dx_1 = 0 \,.$$

Integration by parts now yields:

$$\int_0^L \begin{bmatrix} \frac{\underline{u}_f^T - \underline{u}_i^T}{\Delta t} & \frac{\underline{c}^T}{\Delta t} \end{bmatrix} \left[\frac{\mathcal{R}_f \underline{p}_f^* - \mathcal{R}_i \underline{p}_i^*}{\Delta t} + \mathcal{U}\left[\frac{\widetilde{u_f} - \widetilde{u_i}}{\Delta t}\mathcal{G}_h\right]\frac{\underline{p}_i^* + \underline{p}_f^*}{2}\right] dx_1 + \int_0^L \left\{ \begin{bmatrix} \frac{\underline{u}_f'^T - \underline{u}_i'^T}{\Delta t} & \frac{\underline{c}'^T}{\Delta t} \end{bmatrix} - \begin{bmatrix} \frac{\underline{u}_f^T - \underline{u}_i^T}{\Delta t} & \frac{\underline{c}^T}{\Delta t} \end{bmatrix} \mathcal{U}\left[\frac{2}{c_0}\left(\widetilde{u_0'} + \widetilde{u_h'}\right)\right] \right\} \mathcal{Q}_h \underline{g}_h^* \, dx_1 = \frac{\Delta W}{\Delta t} \,, \tag{6.6}$$

where ΔW is the work done by the externally applied forces during a time step.

Focussing on the inertial terms in the above equation and using relationships (6.2), the first integral writes:

$$\int_0^L \begin{bmatrix} \frac{\underline{u}_f^T - \underline{u}_i^T}{\Delta t} R_h R_0 & \frac{\underline{c}^{*T}}{\Delta t} \end{bmatrix} \left\{ \begin{bmatrix} G^* + \frac{\tilde{c}^{*T}}{4 - c_0} & 0 \\ 0 & I \end{bmatrix} \frac{\underline{p}_f^*}{\Delta t} - \begin{bmatrix} G^{*T} - \frac{\tilde{c}^{*T}}{4 - c_0} & 0 \\ 0 & I \end{bmatrix} \frac{\underline{p}_i^*}{\Delta t} \right\} dx_1 \,.$$

Invoking first eq. (A.5) and then once more relationships (6.2), this integral may be written as:

$$\int_0^L \underline{v}_h^{*T} \frac{\underline{p}_f^* - \underline{p}_i^*}{\Delta t}\, dx_1 = \frac{1}{\Delta t} \int_0^L \underline{v}_h^{*T} M^* \left(\underline{v}_f^* - \underline{v}_i^*\right)\, dx_1 \,, \tag{6.7}$$

where

$$\underline{v}_h^{*T} = \left\lfloor \frac{\underline{u}_f^T - \underline{u}_i^T}{\Delta t} \mathcal{H}_h \quad \frac{\underline{c}^{*T}}{\Delta t} \right\rfloor .$$

Focussing now on the elastic terms in eq. (6.6), the second integral writes:

$$\frac{1}{\Delta t} \int_0^L \underline{g}_h^{*T} \left\{ \mathcal{Q}_h^T \left| \begin{matrix} \underline{u}_f' - \underline{u}_i' \\ \underline{c}' \end{matrix} \right| - \mathcal{Q}_h^T \mathcal{U}^T \left[\frac{2}{c_0} \left(\widetilde{\underline{u}_0'} + \widetilde{\underline{u}_h'} \right) \right] \left| \begin{matrix} 0 \\ \underline{c} \end{matrix} \right| \right\} dx_1 \,. \tag{6.8}$$

Using relationships (6.2), the first three components of the vector between the braces in eq. (6.8) can be written as:

$$\begin{aligned} &\frac{G^{*T} + G^*}{2} R_0^T R_h^T \left[\left(\underline{u}_0' + \underline{u}_f' \right) - \left(\underline{u}_0' + \underline{u}_i' \right) + R_h R_0 \frac{\widetilde{\underline{c}^*}^T}{c_0^*} R_0^T R_h^T \left(\underline{u}_0' + \underline{u}_f' + \underline{u}_0' + \underline{u}_i' \right) \right] \\ &= \frac{G^{*T} + G^*}{2} \left[\left(I + \frac{\widetilde{\underline{c}^*}^T}{c_0^*} \right) R_0^T R_h^T \left(\underline{u}_0' + \underline{u}_f' \right) - \left(I - \frac{\widetilde{\underline{c}^*}^T}{c_0^*} \right) R_0^T R_h^T \left(\underline{u}_0' + \underline{u}_i' \right) \right] . \end{aligned}$$

With the use of, once again, relationships (6.2), and eq. (A.6), the above expression can be further simplified to

$$R_0^T R_f^T \left(\underline{u}_0' + \underline{u}_f' \right) - R_0^T R_i^T \left(\underline{u}_0' + \underline{u}_i' \right) = \underline{\varepsilon}_f^* - \underline{\varepsilon}_i^* \,. \tag{6.9}$$

The last three components of the vector between the braces in eq. (6.8) can be written as:

$$\mathcal{G}_h^T \left(R_h R_0 \underline{c}^* \right)' \,.$$

With the help of relationships (6.2) it may be shown that

$$\mathcal{H}_h^T \left(R_h R_0 \underline{c}^* \right)' = \frac{2G^{*T}}{4 - c_0^*} \left[\underline{c}^{*\prime} + \left(\widetilde{\underline{k}_0^*} + \widetilde{\underline{k}_i^*} \right) \underline{c}^* \right] = \underline{k}_f^* - \underline{k}_i^* \,. \tag{6.10}$$

Combining results (6.9) and (6.10), the elastic terms write:

$$\frac{1}{\Delta t} \int_0^L \underline{g}_h^{*T} \left(\underline{e}_f^* - \underline{e}_i^* \right)\, dx_1 \,. \tag{6.11}$$

Defining the elastic forces $\underline{g}_h^* = C^* \underline{e}_h^*$, where $\underline{e}_h^*$ are yet to be defined sectional strains, the expression (6.11) may be written as:

$$\frac{1}{\Delta t} \int_0^L \underline{e}_h^{*T} C^* \left(\underline{e}_f^* - \underline{e}_i^* \right) \, dx_1 \, . \tag{6.12}$$

Substitution of the final expressions from (6.7) and (6.12) into eq. (6.6) results in:

$$\int_0^L \underline{v}_h^{*T} M^* \left(\underline{v}_f^* - \underline{v}_i^* \right) + \underline{e}_h^{*T} C^* \left(\underline{e}_f^* - \underline{e}_i^* \right) \, dx_1 = \Delta W \, . \tag{6.13}$$

This fundamental scalar relationship is implied by the discretization (6.5) of the beam equations of motion.

6.4 An energy preserving scheme for beams.

An energy preserving integration scheme is obtained by using the basic discretization, equation (6.5), across a time step, from t_n to t_{n+1}:

$$\begin{aligned} &\frac{\mathcal{R}_{n+1} \underline{p}_{n+1}^* - \mathcal{R}_n \underline{p}_n^*}{\Delta t} + \mathcal{U} \left[\frac{\widetilde{u_{n+1}} - \widetilde{u_n}}{\Delta t} \mathcal{G}_{n+\frac{1}{2}} \right] \frac{\underline{p}_n^* + \underline{p}_{n+1}^*}{2} \\ &\quad - \left(\mathcal{Q}_{n+\frac{1}{2}} \underline{f}_{n+\frac{1}{2}}^* \right)' - \mathcal{U} \left[\frac{2}{a_0} \left(\widetilde{u_0'} + \widetilde{u_{n+\frac{1}{2}}'} \right) \right] \mathcal{Q}_{n+\frac{1}{2}} \underline{f}_{n+\frac{1}{2}}^* = \underline{q}_{n+\frac{1}{2}} \, , \end{aligned} \tag{6.14}$$

where $\underline{a}$ are the components of the conformal rotation vector of the rotation from $\mathcal{S}_n$ to $\mathcal{S}_{n+1}$, measured in $\mathcal{S}$ (see Appendix A), the subscript $n + \frac{1}{2}$ refers to the time step mid-point, and $\underline{f}_{n+\frac{1}{2}}$ refers to elastic forces at this mid-point.

In section 6.3, discretization (6.14) is shown to imply:

$$\int_0^L \underline{v}_{n+\frac{1}{2}}^{*T} M^* \left(\underline{v}_{n+1}^* - \underline{v}_n^* \right) + \underline{e}_{n+\frac{1}{2}}^{*T} C^* \left(\underline{e}_{n+1}^* - \underline{e}_n^* \right) \, dx_1 = \Delta W \, . \tag{6.15}$$

The midpoint sectional velocities and strains are now selected as

$$\underline{v}_{n+\frac{1}{2}}^* = \frac{\underline{v}_{n+1}^* + \underline{v}_n^*}{2} \; ; \; \underline{e}_{n+\frac{1}{2}}^* = \frac{\underline{e}_{n+1}^* + \underline{e}_n^*}{2} \, . \tag{6.16}$$

With this choice, eq. (6.15) becomes:

$$E(\underline{u}_{n+1}) - E(\underline{u}_n) = \Delta W \, , \tag{6.17}$$

where the total energy is defined as $E(\underline{u}) = K + V$. In the absence of externally applied loads (i.e. $\Delta W = 0$), eq. (6.17) reduces to

$$E(\underline{u}_{n+1}) - E(\underline{u}_n) = 0 \,, \tag{6.18}$$

which implies the preservation of the total energy.

6.5 Conclusion

In this chapter the energy preserving scheme for elastic, non-linear beams was presented, starting out from a basic discretization of the equations of motion of the beam. This scheme was shown to be unconditionally stable, due to the fact that the total energy of the beam is preserved. Various numerical examples, including convergence studies, to assess the performance of the energy preserving scheme as applied to non-linear beam in multi-body systems, are discussed in chapter 9.

CHAPTER 7
ENERGY DECAYING SCHEME FOR THE TIME INTEGRATION OF BEAM EQUATIONS OF MOTION

7.1 Introduction

The energy preserving scheme developed in the previous chapter presents no high frequency numerical dissipation. Several examples are shown in chapter 9 where the presence of high frequency oscillations seems to hinder, or even render impossible, the convergence in the solution of the non-linear equations of motion. The selection of a smaller time step does not necessarily help this convergence process, as a smaller time step allows even higher frequency oscillations to be resolved. Furthermore, from some examples in chapter 9, it seems that the presence of high frequency oscillations also renders strict energy preservation difficult to obtain. This could prove to be a real limitation of energy preserving schemes when applied to more and more complex models. For such models, the use of an energy decaying integration scheme presenting high frequency numerical dissipation becomes increasingly desirable.

An energy decaying scheme for a non-linear beam is presented in this chapter. The key to the development of an energy decaying scheme is the derivation of an energy decay inequality [18]. A methodology that can systematically lead to such an inequality is the time discontinuous Galerkin method [22]. This method requires the equations of motion to be written in first-order symmetric hyperbolic form. The writing the nonlinear equations of motion of beams in the symmetric hyperbolic form does not appear to be possible. Furthermore, in symmetric hyperbolic form the state vector consists of displacements, velocities, and stresses. This means that a much larger problem needs to be solved, which is more expensive [23, 24].

In this work an alternate, somewhat hybrid, route is taken. This is done in two steps: in a first phase, described in section 7.2, a standard time discontinuous Galerkin method is used to model a single degree of freedom linear oscillator. The equations of motion of this simple system can be cast into the symmetric hyperbolic form, and the energy decay inequality follows from the theory of the time discontinuous Galerkin method applied to hyperbolic conservation laws [25, 26]. On the other hand, as shown in section 7.3, the resulting discretized equations of motion can also be viewed as a finite difference scheme for which the energy decay inequality can be obtained by a direct computation of the work done by the discretized inertial and elastic forces over a time step.

In the second step, presented in section 7.4, the basic discretization of the beam equations of motion, presented in section 6.3, is applied in a manner that mimics the finite difference scheme obtained for the linear oscillator. An energy decay inequality is then derived by a direct computation of the work done by the discretized inertial and elastic forces over a time step, mimicking once more the process used for linear oscillator.

7.2 Time discontinuous Galerkin scheme for a single degree of freedom system.

Consider a linear, single degree of freedom spring mass system, of which the equation of motion is given as:

$$m\ddot{u}(t) + ku(t) = F(t)\,, \tag{7.1}$$

where $u(t)$ is the displacement of the mass m, k the spring stiffness, $F(t)$ the excitation force, and $\dot{(\,)}$ denotes a time derivative. Introducing the momentum $p = m\dot{u}$ leads to the following two equations which are in the symmetric hyperbolic form:

$$\dot{p} + ku = F; \quad \dot{u} - \frac{p}{m} = 0.$$

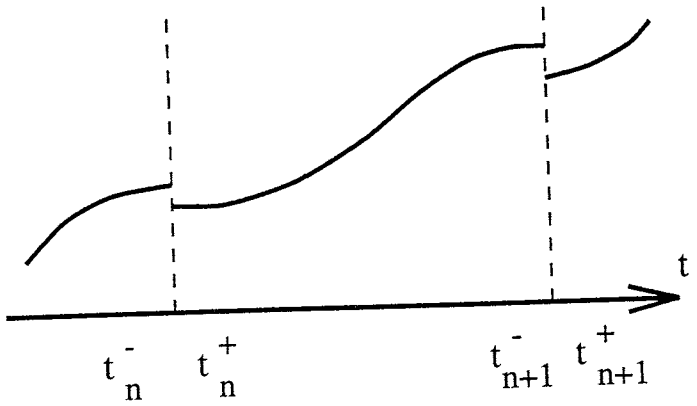

Figure 7.1: Typical time step with function discontinuities at boundaries

A time discontinuous Galerkin approximation of these equations between the initial and final times t_n and t_{n+1} (see figure 7.1) , respectively writes:

$$\int_{t_n^+}^{t_{n+1}^-} \left\{ w_1 \left(\dot{u} - \frac{p}{m} \right) + w_2 \left(\dot{p} + ku - F \right) \right\} dt$$

$$+ w_{1n}^+ \left(u_n^+ - u_n^- \right) + w_{2n}^+ \left(p_n^+ - p_n^- \right) = 0 \, . \tag{7.2}$$

where w_1 and w_2 are test functions, and the notations $(\,)_n^-$, $(\,)_n^+$ and $(\,)_{n+1}^-$ are used to indicate the corresponding quantities at t_n^-, t_n^+ and t_{n+1}^-, respectively.

Integrating eq. (7.2) by parts yields:

$$\int_{t_n^+}^{t_{n+1}^-} \left(-\dot{w}_1 u - w_1 \frac{p}{m} - \dot{w}_2 p + w_2 k u - w_2 F \right) dt$$

$$+ w_{1\,n+1}^- u_{n+1}^- + w_{2\,n+1}^- p_{n+1}^- - w_{1\,n}^+ u_n^- - w_{2\,n}^+ p_n^- = 0 \, . \tag{7.3}$$

A linear in time approximation over the time step is used to discretize the unknowns u and p, the test functions w_1 and w_2, and the excitation force F. The resulting discretized equations of motion are readily found by integrating (7.3) to find:

$$\frac{m \dfrac{\dot{u}_{n+1}^- + \dot{u}_n^+}{2} - m\dot{u}_n^-}{\Delta t} + k \frac{u_{n+1}^- + 2u_n^+}{6} = \frac{F_n^+}{3} + \frac{F_{n+1}^-}{6};$$

$$\frac{m\dot{u}^-_{n+1} - m\dfrac{\dot{u}^-_{n+1}+\dot{u}^+_n}{2}}{\Delta t} + k\frac{2u^-_{n+1}+u^+_n}{6} = \frac{F^+_n}{6} + \frac{F^-_{n+1}}{3};$$

$$\frac{\dfrac{u^-_{n+1}+u^+_n}{2} - u^-_n}{\Delta t} = \frac{\dot{u}^-_{n+1}+2\dot{u}^+_n}{6};$$

$$\frac{u^-_{n+1} - \dfrac{u^-_{n+1}+u^+_n}{2}}{\Delta t} = \frac{2\dot{u}^-_{n+1}+\dot{u}^+_n}{6}.$$

These four equations may be combined in a linear fashion to yield:

$$\frac{m\dot{u}^-_{n+1} - m\dot{u}^-_n}{\Delta t} + ke_m = \frac{F^+_n + F^-_{n+1}}{2}; \tag{7.4}$$

$$\frac{m\dot{u}^+_n - m\dot{u}^-_n}{\Delta t} + ke_j = \frac{F^+_n - F^-_{n+1}}{6}; \tag{7.5}$$

$$\frac{u^-_{n+1} - u^-_n}{\Delta t} = \frac{\dot{u}^-_{n+1}+\dot{u}^+_n}{2}; \quad e_m = \frac{u^-_{n+1}+u^+_n}{2}; \tag{7.6}$$

$$\frac{u^+_n - u^-_n}{\Delta t} = -\frac{\dot{u}^-_{n+1}-\dot{u}^+_n}{6}; \quad e_j = -\frac{u^-_{n+1}-u^+_n}{6}. \tag{7.7}$$

Equations (7.4) to (7.7) define a time discontinuous approximation of the equation of motion of the system, eq. (7.1). The unconditional stability of the scheme can be proved based on the energy decay inequality that follows from the theory of the time discontinuous Galerkin method applied to hyperbolic conservation laws [25, 26].

This can be confirmed by a conventional analysis of the scheme based on the characteristics of the amplification matrix. The period elongation is $\frac{\Delta T}{T} = \frac{\omega^4\Delta t^4}{270} + O(\omega^6\Delta t^6)$, while the algorithmic damping is $\zeta = \frac{\omega^3\Delta t^3}{72} + O(\omega^5\Delta t^5)$, where $\omega^2 = k/m$. Hence, the scheme is third-order accurate. The spectral radius, period elongation, and algorithmic damping are shown in figures 7.2 to 7.4 as functions of $\Delta t/T = \omega\Delta t/(2\pi)$. The results are compared with generalized-α method [19] with three different values of spectral radius at infinity, $\rho_\infty = 0.9, 0.5$, and 0.0. Figure 7.3 indicates that the time discontinuous Galerkin scheme has better period elongation characteristics than generalized-α method, while figure 7.4 shows that its low frequency numerical dissipation characteristics are similar those of the generalized-α

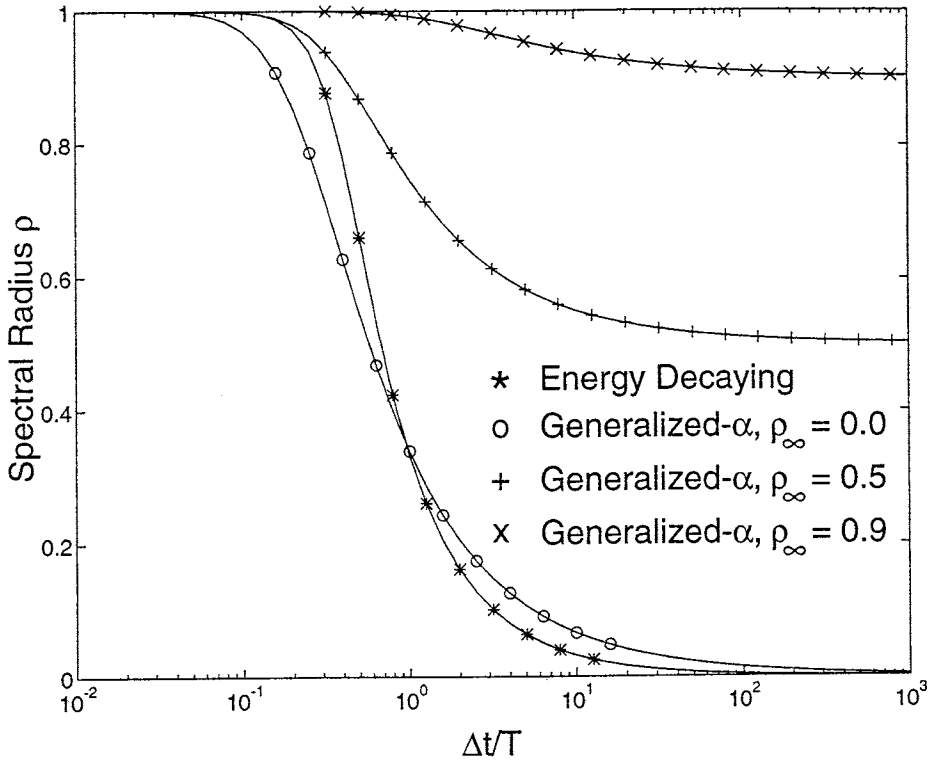

Figure 7.2: Comparison of spectral radii of various time integration schemes

method with $\rho_\infty = 0.5$. Asymptotic annihilation is obtained with the time discontinuous Galerkin scheme. The scheme is unconditionally stable since the spectral radius is always smaller than unity.

7.3 Stability proof based on an energy argument.

An alternate way of proving the unconditional stability is based on a direct computation of the work done by the inertial and elastic forces which will be shown to imply an energy decay inequality. The total energy of the system is $E(u) = K(\dot{u}) + V(u)$, where the kinetic energy is $K(\dot{u}) = \frac{1}{2}m\dot{u}^2$ and the potential energy $V(u) = \frac{1}{2}ku^2$. The change in total energy over a time step can be evaluated by computing the work done by the inertial and elastic forces. The discretized equation

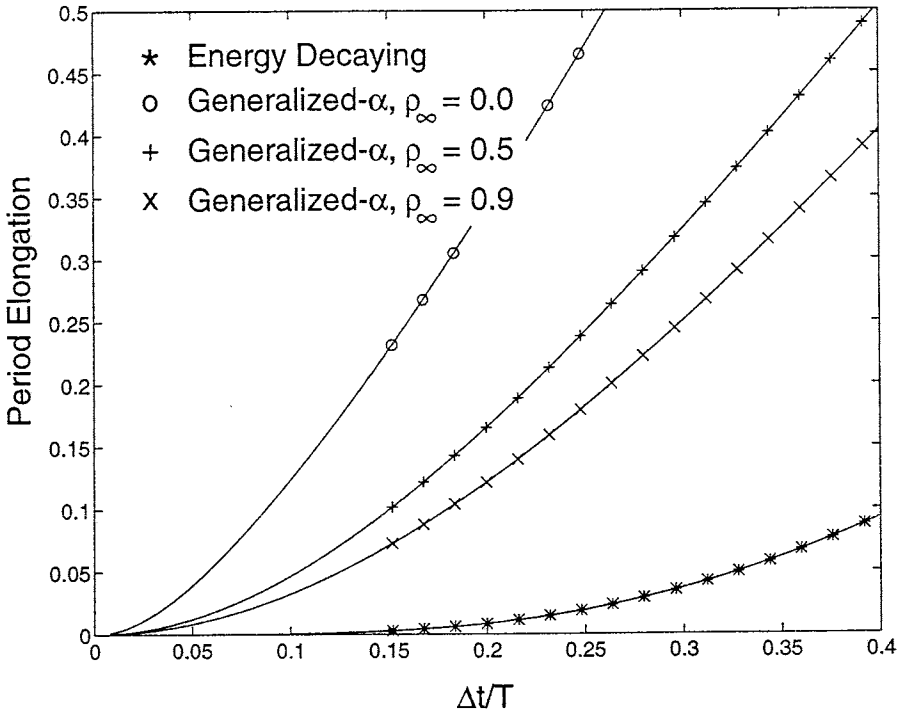

Figure 7.3: Comparison of period elongation of various time integration schemes

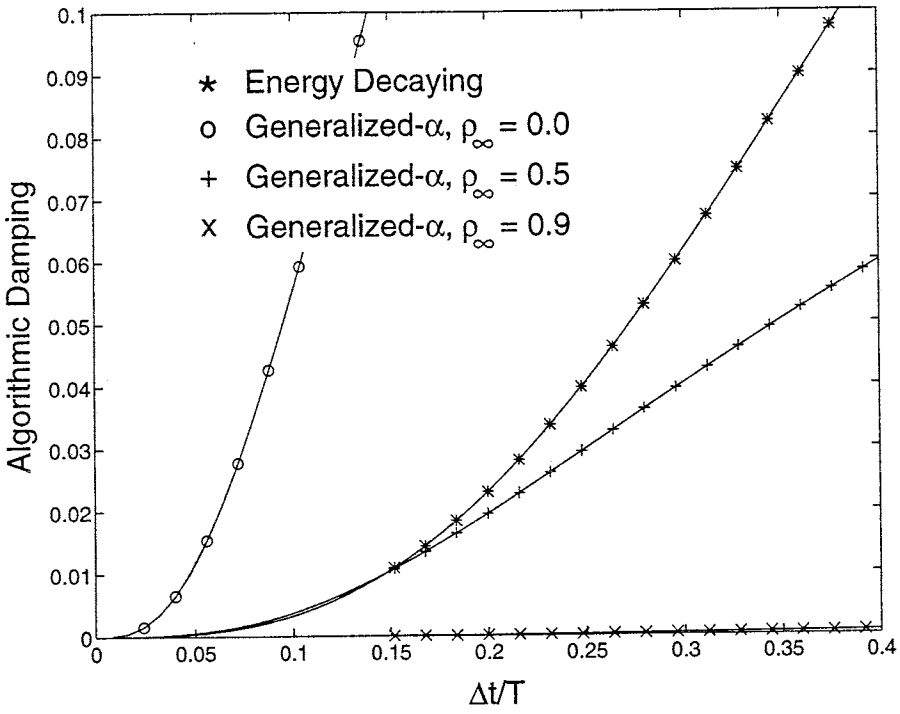

Figure 7.4: Comparison of algorithmic damping of various time integration schemes

of motion (7.4) is multiplied by a displacement increment to yield:

$$\left(\frac{u_{n+1}^- - u_n^-}{\Delta t}\right)\frac{m\dot{u}_{n+1}^- - m\dot{u}_n^-}{\Delta t} + \left(\frac{u_{n+1}^- - u_n^-}{\Delta t}\right)k\frac{u_{n+1}^- + u_n^+}{2} = \frac{\Delta W_m}{\Delta t}\,,$$

where ΔW_m is the work done by the applied loads. With the help of eq. (7.6), this can be rewritten as:

$$\left(\frac{\dot{u}_{n+1}^- + \dot{u}_n^-}{2}\right)\frac{m\dot{u}_{n+1}^- - m\dot{u}_n^-}{\Delta t} + \left(\frac{u_{n+1}^- - u_n^-}{\Delta t}\right)k\frac{u_{n+1}^- + u_n^+}{2} = \frac{\Delta W_m}{\Delta t}\,,$$

and simplifies to:

$$E\left(u_{n+1}^-\right) - E\left(u_n^-\right) + E\left(u_n^+ - u_n^-\right)$$
$$+\frac{1}{2}(\dot{u}_n^+ - \dot{u}_n^-)m(\dot{u}_{n+1}^- - \dot{u}_n^+) + \frac{1}{2}(u_n^+ - u_n^-)k(u_{n+1}^- - u_n^+) = \Delta W_m\,. \quad (7.8)$$

Next, the discretized equation of motion (7.5) is multiplied a displacement increment across the jump to find:

$$\left(\frac{u_n^+ - u_n^-}{\Delta t}\right)\frac{m\dot{u}_n^+ - m\dot{u}_n^-}{\Delta t} + \left(\frac{u_n^+ - u_n^-}{\Delta t}\right)k\frac{u_n^+ - u_{n+1}^-}{6} = \frac{\Delta W_j}{\Delta t}\,,$$

where ΔW_j is the work done by the applied loads. Using eq. (7.7), the above equation rewrites as:

$$\left(\frac{\dot{u}_n^+ - \dot{u}_{n+1}^-}{6}\right)\frac{m\dot{u}_n^+ - m\dot{u}_n^-}{\Delta t} + \left(\frac{u_n^+ - u_n^-}{\Delta t}\right)k\frac{u_n^+ - u_{n+1}^-}{6} = \frac{\Delta W_j}{\Delta t}\,,$$

and simplifies to:

$$-\frac{1}{6}(\dot{u}_n^+ - \dot{u}_n^-)m(\dot{u}_{n+1}^- - \dot{u}_n^+) - \frac{1}{6}(u_n^+ - u_n^-)k(u_{n+1}^- - u_n^+) = \Delta W_j\,. \quad (7.9)$$

Finally, a linear combination of eqs. (7.8) and (7.9) yields the following energy statement:

$$E\left(u_{n+1}^-\right) - E\left(u_n^-\right) + E\left(u_n^+ - u_n^-\right) = \Delta W_m + 3\Delta W_j\,. \quad (7.10)$$

In the absence of externally applied loads, the following energy decay characteristic of the scheme is established:

$$E\left(u_{n+1}^-\right) = E\left(u_n^-\right) - E\left(u_n^+ - u_n^-\right), \quad \Rightarrow \quad E\left(u_{n+1}^-\right) \le E\left(u_n^-\right)\,. \quad (7.11)$$

This energy decay inequality provides an alternate proof of the unconditional stability of the scheme. Equation (7.11) implies exact preservation of energy when the energy associated with the jump ($E\left(u_n^+ - u_n^-\right)$) is zero. This can be achieved by enforcing continuity of displacement and momentum at the inter-element boundary. In that case the (unconditionally stable) average acceleration scheme is recovered.

7.4 An energy decaying scheme for beams.

An energy decaying scheme for beams is obtained by extending the single degree of freedom time discontinuous Galerkin method described in section 7.2 to the equations of motion of a beam, eq. (2.11). The basic discretization (6.5) is applied first over the time step, i.e. from t_n^- to t_{n+1}^-:

$$\frac{\mathcal{R}_{n+1}^- \underline{p}_{n+1}^{*-} - \mathcal{R}_n^- \underline{p}_n^{*-}}{\Delta t} + \mathcal{U}\left[\frac{\widetilde{u_{n+1}^-} - \widetilde{u_n^-}}{\Delta t}\mathcal{G}_m\right]\frac{\underline{p}_n^{*-} + \underline{p}_{n+1}^{*-}}{2}$$
$$-\left(\mathcal{Q}_m \underline{f}_m^*\right)' - \mathcal{U}\left[\frac{2}{a_0}\left(\widetilde{u_0'} + \widetilde{u_m'}\right)\right]\mathcal{Q}_m \underline{f}_m^* = \underline{q}_m, \tag{7.12}$$

where $\underline{a}$ are the components of the conformal rotation vector of the rotation from $\mathcal{S}_n^-$ to $\mathcal{S}_{n+1}^-$, measured in $\mathcal{S}$ (see Appendix A), the subscript m refers to the time step mid-point, and $\underline{f}_m$ refers to elastic forces at this mid-point. The basic discretization (6.5) is then applied across the jump, i.e. from t_n^- to t_n^+:

$$\frac{\mathcal{R}_n^+ \underline{p}_n^{*+} - \mathcal{R}_n^- \underline{p}_n^{*-}}{\Delta t} + \mathcal{U}\left[\frac{\widetilde{u_n^+} - \widetilde{u_n^-}}{\Delta t}\mathcal{G}_j\right]\frac{\underline{p}_n^{*-} + \underline{p}_n^{*+}}{2}$$
$$-\left(\mathcal{Q}_j \underline{f}_j^*\right)' - \mathcal{U}\left[\frac{2}{b_0}\left(\widetilde{u_0'} + \widetilde{u_j'}\right)\right]\mathcal{Q}_j \underline{f}_j^* = \underline{q}_j, \tag{7.13}$$

where $\underline{b}$ are the components of the conformal rotation vector of the rotation from $\mathcal{S}_n^-$ to $\mathcal{S}_n^+$, measured in $\mathcal{S}$, the subscript j refers to the jump "mid-point", and $\underline{f}_j$ refers to elastic forces at this mid-point.

The unconditional stability of the scheme defined by equations (7.12) and (7.13) will be established based on an energy argument. The proof follows the steps

described in section (7.3) for the single degree of freedom system. The work done by the inertial and elastic forces in eq. (7.12) was computed in 6.3 as:

$$\int_0^L \underline{v}_m^{*T} M^* \left(\underline{v}_{n+1}^{*-} - \underline{v}_n^{*-}\right) + \underline{e}_m^{*T} C^* \left(\underline{e}_{n+1}^{*-} - \underline{e}_n^{*-}\right) \, dx_1 = \Delta W_m. \tag{7.14}$$

By analogy to eq. (7.6), the midpoint sectional velocities and strains are selected as:

$$\underline{v}_m^* = \frac{\underline{v}_{n+1}^{*-} + \underline{v}_n^{*+}}{2}; \quad \underline{e}_m^* = \frac{\underline{e}_{n+1}^{*-} + \underline{e}_n^{*+}}{2}. \tag{7.15}$$

With this choice, eq. (7.14) now becomes:

$$E(\underline{u}_{n+1}^-) - E(\underline{u}_n^-) + E(\underline{u}_n^+ - \underline{u}_n^-) + \frac{1}{2}\int_0^L \left\{\left(\underline{v}_n^{*+T} - \underline{v}_n^{*-T}\right) M^* \left(\underline{v}_{n+1}^{*-} - \underline{v}_n^{*+}\right) + \left(\underline{e}_n^{*+T} - \underline{e}_n^{*-T}\right) C^* \left(\underline{e}_{n+1}^{*-} - \underline{e}_n^{*+}\right)\right\} \, dx_1 = \Delta W_m. \tag{7.16}$$

This equation is equivalent to (7.8).

The work done by the inertial and elastic forces in eq. (7.13) was computed in 6.3 as:

$$\int_0^L \underline{v}_j^{*T} M^* \left(\underline{v}_n^{*+} - \underline{v}_n^{*-}\right) + \underline{e}_j^{*T} C^* \left(\underline{e}_n^{*+} - \underline{e}_n^{*-}\right) \, dx_1 = \Delta W_j \, . \tag{7.17}$$

By analogy to eq. (7.7), the midpoint sectional velocities and strains are now selected as:

$$\underline{v}_j^* = -\frac{\underline{v}_{n+1}^{*-} - \underline{v}_n^{*+}}{6}; \quad \underline{e}_j^* = -\frac{\underline{e}_{n+1}^{*-} - \underline{e}_n^{*+}}{6}. \tag{7.18}$$

With this choice, eq. (7.17) now becomes:

$$-\frac{1}{6}\int_0^L \left\{\left(\underline{v}_n^{*+T} - \underline{v}_n^{*-T}\right) M^* \left(\underline{v}_{n+1}^{*-} - \underline{v}_n^{*+}\right) + \left(\underline{e}_n^{*+T} - \underline{e}_n^{*-T}\right) C^* \left(\underline{e}_{n+1}^{*-} - \underline{e}_n^{*+}\right)\right\} \, dx_1 = \Delta W_j. \tag{7.19}$$

This equation is equivalent to (7.9). Finally, a linear combination of eqs. (7.16) and (7.19) yields the following energy statement:

$$E(\underline{u}_{n+1}^-) - E(\underline{u}_n^-) + E(\underline{u}_n^+ - \underline{u}_n^-) = \Delta W + 3\Delta W_j, \tag{7.20}$$

which is identical to (7.10). In the absence of externally applied loads, the following energy decay characteristic of the scheme is established:

$$E\left(u_{n+1}^{-}\right) = E\left(u_{n}^{-}\right) - E\left(u_{n}^{+} - u_{n}^{-}\right), \quad \Rightarrow \quad E\left(u_{n+1}^{-}\right) \leq E\left(u_{n}^{-}\right). \tag{7.21}$$

This proves the unconditional stability of the finite difference scheme defined by eqs. (7.12), (7.13), (7.15) and (7.18). Note that the velocities can be readily eliminated from the formulation by using the vector equations (7.15) and (7.18). Standard finite element techniques can be applied to discretize the problem leading to a set of non-linear algebraic equations for the displacements at times t_n^+ and t_{n+1}^-.

7.5 Conclusion

In this chapter the energy decaying scheme for the example of a non-linear beam was presented. This scheme was obtained by applying the basic discretization of the equations of motion of a beam in a manner that mimics the time discontinuous Galerkin method applied to a linear oscillator. An energy decay inequality was derived, which proves the unconditional stability of the scheme.

The use of the energy decaying scheme to analyze non-linear beam dynamics is illustrated with a number of examples in section 9.3. These examples show that this scheme inherits the salient features of the time discontinuous Galerkin method, of high frequency numerical dissipation with asymptotic annihilation, and, as is evident from a number of convergence studies, to a certain degree also the third order accuracy. The use of this scheme in multi-body analysis is presented in section 9.4.

CHAPTER 8
ENFORCEMENT OF KINEMATIC CONSTRAINTS

8.1 Introduction

Energy preserving and energy decaying schemes for the time integration of non-linear beam equations of motion have been presented in chapters 6 and 7. To be able to analyze multi-body systems, attention must now be given to the enforcement of kinematic constraints. In oder to ensure the stability of the integration process, the forces of constraint need to be discretized in such a way that they perform no work. An example of a single degree of freedom pendulum, modeled as a two degree of freedom system with a single constraint, is presented in section 8.2. This example is later used in the discussions of both the energy preserving and energy decaying schemes, to allow clearer understanding of the above requirement and how it is achieved. Also, the discretization of this very basic equation of constraint with the time discontinuous Galerkin method forms a useful parallel for finding the optimum discretization of the equations of constraint in the case of the energy decaying scheme.

The enforcement of constraints within the energy preserving scheme is discussed in section 8.3. First the simple pendulum is discussed, and then, in section 8.3.2, the basic discretization of the equations of constraint of a revolute joint is presented. This basic discretization is used by both the energy preserving and energy decaying schemes. A fundamental and very useful work expression resulting from this basic discretization is also presented in section 8.3.2. The section on the energy preserving scheme concludes, in section 8.3.3, by showing how the implementation of the basic discretization of the forces of constraint leads to the vanishing of all work done by these forces.

decay inequality [25, 26]. Two approaches will be investigated corresponding to constant, or linear in time approximations for the Lagrange multiplier, respectively.

8.3 Energy Preserving Scheme

In this section the enforcement of kinematic constraints with the energy preserving scheme is discussed. The simple pendulum example is treated first, after which the revolute joint is considered.

8.3.1 Discretization of pendulum equations

The following discretization of the pendulum equations of motion, eq. (8.2) is proposed:

$$\frac{m\dot{\underline{u}}_{n+1} - m\dot{\underline{u}}_n}{\Delta t} + \frac{\underline{u}_{n+1} + \underline{u}_n}{2} s\lambda_{n+\frac{1}{2}} = m\underline{g} \; ; \tag{8.3}$$

$$\frac{\underline{u}_{n+1} - \underline{u}_n}{\Delta t} = \frac{\dot{\underline{u}}_{n+1} + \dot{\underline{u}}_n}{2} \; . \tag{8.4}$$

This discretization does not account for the presence of the constraint (8.1). Premultiplying eq. (8.3) by the transpose of $\frac{\underline{u}_{n+1} - \underline{u}_n}{\Delta t}$ allows the work performed by the inertial and constraint forces to be computed. This yields the following energy related statement:

$$E(\underline{u}_{n+1}) - E(\underline{u}_n) + \left(\mathcal{C}(\underline{u}_{n+1}) - \mathcal{C}(\underline{u}_n)\right) s\lambda_{n+\frac{1}{2}} = 0 \; ,$$

where the last term corresponds to the work done by the discretized forces of constraint. The total energy of the system is $E(\underline{u}) = K(\dot{\underline{u}}) + P(\underline{u})$, where the kinetic energy is $K(\dot{\underline{u}}) = \frac{1}{2} m \dot{\underline{u}}^T \dot{\underline{u}}$ and the potential energy $P(\underline{u}) = -m\underline{u}^T \underline{g}$.

The *discretized* constraint conditions are selected so that the work done by the discretized forces of constraint vanishes, i.e.

$$\frac{\mathcal{C}(\underline{u}_{n+1}) - \mathcal{C}(\underline{u}_n)}{\Delta t} = 0 \; , \tag{8.5}$$